Characterization of Qubit Control Pulse Distortions in Superconducting Quantum Hardware

AMIRTHA VARSHINY ARUMUGAM

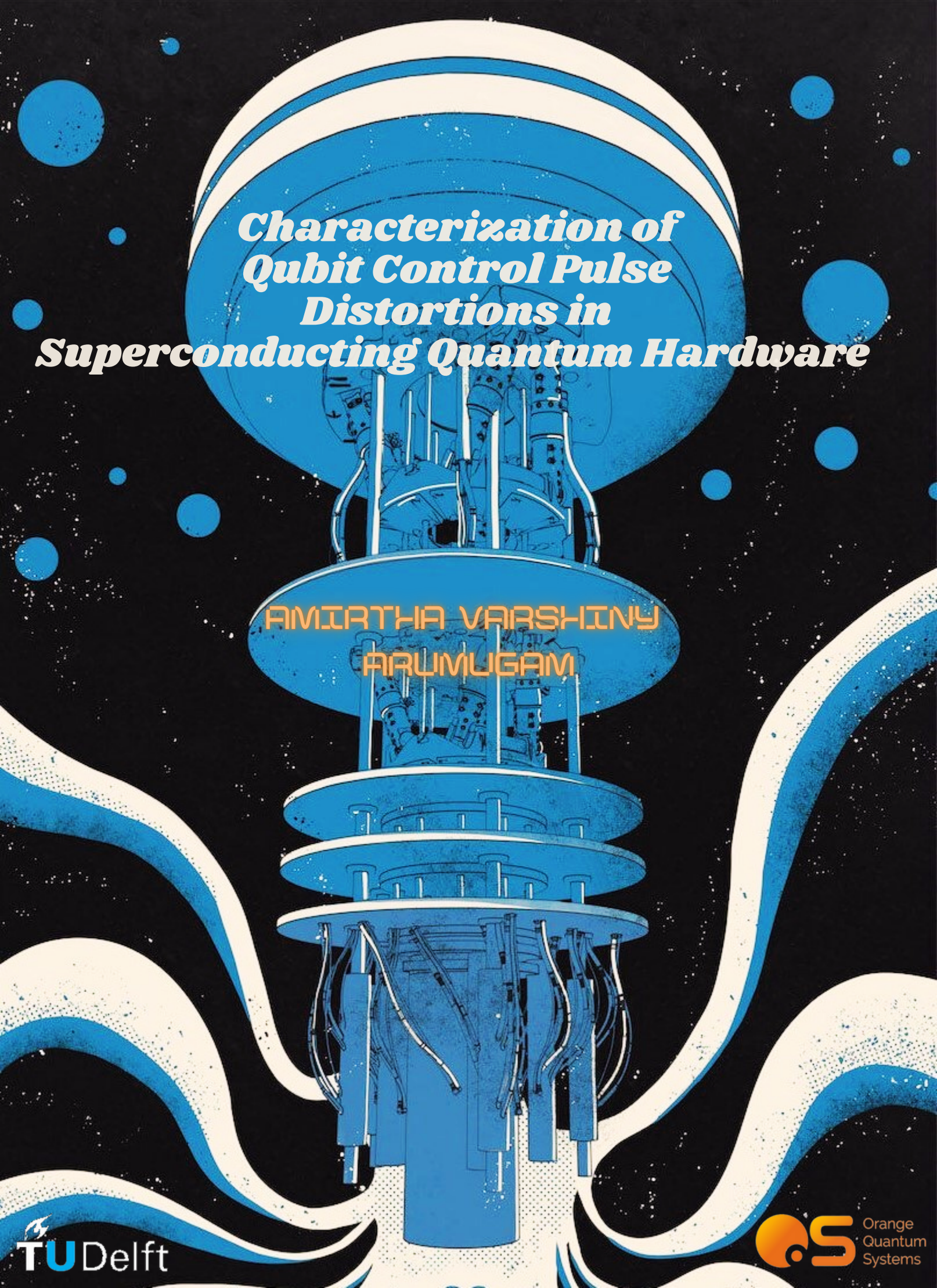

TU Delft

Orange Quantum Systems

Characterization of Qubit Control Pulse Distortions in Superconducting Quantum Hardware

by

Amirtha Varshiny Arumugam

to obtain the degree of Master of Science in Computer Engineering
at the Delft University of Technology,
to be defended publicly on 15/02/2023

Student number: 5243149
Project duration: November 17, 2021 – October 31, 2022
Thesis committee:

Dr. F. Sebastiano,	TU Delft, supervisor
Dr. D. S. Wong,	TU Delft
Dr. A. Rol,	Orange Quantum Systems

TU Delft

Acknowledgements

Amirtha Varshiny Arumugam
Delft, February 2023

First, I would like to thank my family for all their love and support. The three of you held me together from so far away. I couldn't have done this without you and all the cute pictures of Milo you sent at 3 am.
I thank my supervisor, Dr Fabio Sebastiano, for his guidance and indispensable help. Despite your busy schedule, I could always reach you whenever I needed guidance and signatures on the various documents. I could not thank you enough for your patience and understanding. Most of the learning that I got in this thesis happened in our meetings and I will always be grateful for the support, both technical and moral, that I got from you on this rather rocky journey. Thank you for imparting all the invaluable quantum and non-quantum-related knowledge.
I thank Kelvin Loh, my daily supervisor at Orange Quantum Systems, for his innumerable help and guidance. Thank you for helping me with all the technical parts of the thesis. Without your aid, implementing all the methods wouldn't have been possible.
I thank Dr Adriaan Rol for offering this interesting thesis project and for patiently explaining, answering all my questions about the subject. I thank my fellow interns, Tim and Timo, for spelling out important concepts of quantum physics in basic terms that a non-physics student like me could understand. I thank all the members of Orange Quantum Systems, Thorsten, Garrelt, Anna, Slava, Amber, Adam, Konstantin, Vraj and Sebastian, for their help. It was a pleasure working alongside you in all three locations our office had been in.

I would like to thank Monica, for being my supportive roommate, for the unplanned Ramen runs and for the not-so-helpful advice sessions. I thank Ravi for being a stalwart support with the very helpful advice sessions. I thank Alexandra for dragging me to book clubs and for being a solid friend who I can always fall back on to complain about the courses at TU Delft. I thank Sadhna for her unending optimism and the drama her questionable choices in life led her to. I am grateful to Maitry for being a wonderful friend and for consistently accompanying me to all Marvel films.
I also would like to mention the eleventh-hour wizards, Denesh, Iva, Anish, Karthik and Yu-Wen. Thank you for the immeasurable help that I needed at the last moment. I also thank Aishwarya for being an amazing senior and for helping me with my thesis and life in general. I am grateful to Sneha for all our weekend meetings and for your assistance in preserving my wits these past two years. My friends across different continents, Keerthana, Veena, Prakalya, Vidyaa, Divya and Antony, though you were not next to me physically, thank you for all the support and love.

Lastly, I would also like to thank the TU Delft library for bearing silent witness to my numerous meltdowns, last-minute exam prep anguish and the many late-night existential crises over the last couple of years. You're a champ, and I will always be indebted to you for being one of the few buildings accessible during the pandemic.

Abstract

With the slow recession in the number of transistors that can be placed onto a chip, other innovative methods to further improve the performance of computing have become a necessity. One such avenue that is being extensively explored is Quantum Computing. It is the field of research, which involves harnessing special properties of quantum mechanical systems – such as superposition and entanglement – to process information. These systems hold the potential to solve problems that elude classical computers, and also promise an incredible speedup of computation over classical computers.

With the advent of many promising quantum mechanical systems that can be effectively employed to execute quantum computing algorithms, methods to optimize these systems have also been researched. These quantum mechanical systems being used to execute algorithms are termed "qubits" - **qu**antum mechanical **bits**. Qubits face many problems when being used for the optimal execution of algorithms, the primary problem being their high sensitivity to noise. Being exposed to noise can cause the qubit to lose its information. Therefore, the effect of noise on qubit systems needs to be minimized for the qubits to retain data and function effectively.

In superconducting transmons, a type of qubit system, the configuration of the qubit is such that the qubit frequency is controlled by varying the magnetic field passing through the transmon. In order to control this frequency, voltage pulses to alter the magnitude of the flux are applied. For the flux to affect the qubit frequency as intended, the input pulse to the qubit has to be as ideal as possible. However, in practical situations, the input pulse faces distortions caused by the instruments on this control line. Therefore, the goal of this thesis project is to study the distortions that occur on the input voltage pulse due to noise parameters. Another objective was also to implement methods to identify these fluctuations and rectify them.

The thesis work includes the study and implementation of three such methods. The methods employed are the Cryoscope, the Chevron and Ramsey using Kelly's method. The principle behind these three methods and their implementation are discussed in detail. This is then followed by the data analysis of the measurements leading to corresponding method results. Using these results, a comparison of the three methods has also been elaborated upon.

Contents

1

Introduction

Everything we call real is made of things that cannot be regarded as real.
- Niels Bohr

Computing systems have constantly been innovated to achieve higher performances. In this quest for faster and better systems, computer performance was heavily influenced by the number of transistors that could be squeezed onto a chip. With improvements in silicon technology, chips have become smaller, along with an increase in the number of transistors. This trend, succinctly explained by Moore, has driven the computing industry in these past years [1]. However, it has been shown that this cannot be sustained, as recent chip manufacturers have run into problems around power consumption and heat generation [2]. A transistor is used in encoding information by switching it ON or OFF by sending electrical currents to control the gate voltage. As transistors become smaller and smaller, the capacity of the gate to stop the flow of current during switching reduces. This causes the transistor to continuously consume energy even when it is not required, leading to power wastage. There is also excessive heat generation that hinders the effective functioning of the transistors.
To solve these problems, methods such as parallel processing on multi-core technologies [2] [3] and spatial computing using reconfigurable hardware [4] are being explored. Parallel to this research on enhancing the performance of computing systems, there has been an exciting alternative in the form of a computing environment offered by quantum physics. By entirely disregarding the use of transistors altogether, this field of Quantum Computing intends to process information using **qubits**. Qubits are quantum mechanical systems with interesting properties - such as superposition and entanglement - that can be used to encode and process information.
Superposition is a unique property displayed by qubits wherein the qubit can exist as a combination of states. In known analog computing, information stored as bits is described using the state of the bit, i.e., if the bit is '0' or '1'. Similarly, a qubit can be described by its *superposition* state, a combination of $|0\rangle$ and $|1\rangle$. Therefore, a qubit state ($|\Psi\rangle$) is defined as

$$|\Psi\rangle = \alpha\,|0\rangle + \beta\,|1\rangle \tag{1.1}$$

where α and β are complex coefficients that adhere to $|\alpha|^2 + |\beta|^2 \leq 1$. Similar to how analog gates such as NOT, AND, OR are used to manipulate bits, *quantum* gates operate on the qubit, causing changes to its state as described in Equation 1.1.
Entanglement is a phenomenon observed in multi-qubit systems. Two qubits are "entangled" if the net qubit state can no longer be expressed as a product of the two individual quantum states. For example, we consider the Bell state $|\Phi_+\rangle = \frac{1}{\sqrt{2}}(|00\rangle + |11\rangle)$.
Due to entanglement, this state cannot be expressed using the two singular individual states. That is,

$$|\Psi\rangle_{q1} \otimes |\Psi\rangle_{q2} \neq |\Phi_+\rangle$$

Entanglement has given rise to interesting transformations such as Quantum teleportation and Superdense coding (Refer Chapter 1 of [5]).
As mentioned earlier, in our contemporary systems, information is encoded and processed in bits. These 'classical' bits are processed using circuits on integrated chips primarily consisting of transistors. Therefore, the transistor is the standard, basic element required for the realization of present-day computing systems. In contrast, qubits don't have such standard elements for their realization. At present, many different quantum mechanical systems have been shown as viable options for realising a qubit. These include superconducting qubits [6], nitrogen vacancies in diamond [7] [8], electron spins in silicon [9], quantum dots [10], trapped ions [11] [12], ultracold atoms [13] and polarized photons [14].
Unlike its classical analogue, a quantum computer, comprised of qubits realized on any of these platforms mentioned above, has multiple, individually functioning parts across different temperatures that make up the entire system. For example, when using superconducting qubits as the basic processing element, the computing system contains a dilution refrigerator housing the 'quantum chip' since superconducting qubits function at cryogenic temperatures. This qubit is then controlled using a variety of electronics kept both at cryogenic temperatures and at room temperature.
Therefore, a quantum computer is a complex system comprising of the quantum processor with the qubit(s)

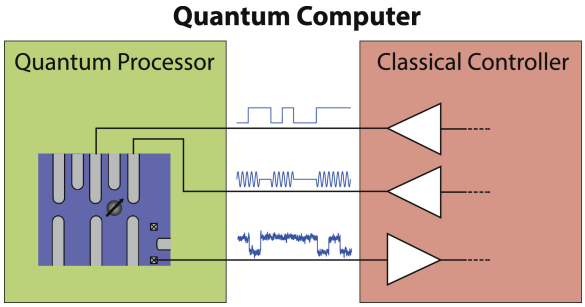

Figure 1.1: Representation of a Quantum Computer [15]

and the electronic interface that controls the quantum processor. This has been shown in Figure 1.1.
With each qubit realization platform having its own individual advantages and disadvantages, the common denominator they share is that the entire quantum computing system is big in comparison to our current 'classical' computing systems. Hence, the control and data extraction method from the qubit system varies for different realization platforms. In this report, the experiments have been tailored for execution on a superconducting qubit called the transmon. Another sharp contrast when comparing quantum computing systems to classical computing systems, is that calibration of the system is relatively tedious and has to be done regularly. Calibrating the qubit is of utmost importance to get accurate results from any experiment since the qubit is highly susceptible to noise. Many different sources of noise in the system affect the qubit. One of the many observed effects is the presence of distortions in the flux control line of a transmon qubit system. These distortions cause adverse effects on the transmon qubit, affecting its ability to couple with another qubit. Therefore, this thesis aims to identify and rectify the distortions in the flux control of transmon systems.

1.1. Superconducting qubits

Superconducting qubits are one of the leading technologies in realising qubits and quantum logic operations. With the ability for a sufficiently high control together with low noise in measurements, superconducting circuits present a very viable method of realising a quantum computer [16]. These devices, called *circuit Quantum Electrodynamic Devices* (cQED), are used to process quantum information by employing the principles of quantum mechanics at extremely low temperatures.
Superconducting qubits comprise of the superconducting element and circuits fabricated on silicone/sapphire substrates made compatible with CMOS circuits. This is then placed within an electromagnetic environment, out of which the necessary signal lines are drawn. The basic building blocks of the superconducting qubits circuitry include resonators, couplers, bias lines and other basic electrical components such as Arbitrary Wave Generators, Amplifiers etc. All these come together as parts of the entire quantum computing system using superconducting qubits.
The main component of the superconducting qubits are the superconducting elements termed Josephson

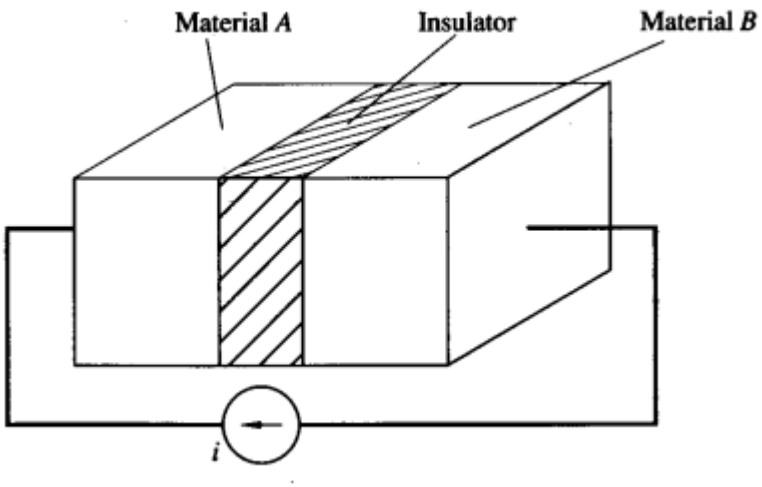

Figure 1.2: Diagram Representation of a Josephson Junction [17]

junctions. A **Josephson junction** is a device that consists of two superconductors separated using a thin film insulator as shown in Figure 1.2. A supercurrent is then observed in this configuration between the two superconductors (Material A and Material B) due to the flow of Cooper pairs tunnelling through the insulating barrier [18]. When describing the condensate wavefunction of the two superconductors in the Josephson junction, the Josephson phase (φ) is taken as the phase difference of the wavefunctions [19]. This leads to the famed Josephson relations,

$$I = I_c \sin\varphi \tag{1.2}$$

$$\frac{d\varphi}{dt} = \frac{2e}{\hbar} V \tag{1.3}$$

where,

I – supercurrent through the junction
I_c – critical current
V – voltage across the junction

The critical current I_c is the maximum current that can flow in the Josephson junction and is a constant for a particular setup. Combining the Equations 1.2 and 1.3, the non-linear dependence between current and voltage is derived, which is a distinct characteristic of the Josephson junction. From Equation 1.2,

$$I = I_c \sin\varphi \tag{1.4}$$

$$\frac{dI}{dt} = I_c \cos\varphi \frac{d\varphi}{dt} \tag{1.5}$$

Using Equation 1.3,

$$\left(\frac{1}{(I_c * \frac{2e}{\hbar}) * (\cos\varphi)}\right) * \frac{dI}{dt} = V \tag{1.6}$$

Equation 1.6 is similar to the current-voltage relation observed in inductors. Therefore, the Josephson Junction can be considered as a non-linear inductor with the inductance as $L = \left(\frac{1}{(I_c * \frac{2e}{\hbar}) * (\cos\varphi)}\right)$.

The energy associated with this inductance can be derived using

$$\begin{aligned} E_L &= \int_0^t I * V\, dt \\ &= \int_0^t (I_c \sin\varphi) * (\frac{\hbar}{2e}\frac{d\varphi}{dt}) dt \\ &= \frac{\hbar * I_c}{2e}\int_0^\varphi (\sin\varphi) d\varphi \\ &= \frac{-\hbar * I_c}{2e}\cos\varphi \end{aligned}$$

This is then rewritten as

$$E_L = -E_J \cos\varphi \tag{1.7}$$

where $E_J = \frac{\hbar * I_c}{2e}$.
The Josephson Junction also faces some stray capacitance whose energy contribution can be quantified as

$$E_{CJ} = \frac{q^2}{2C_J}$$

where C_J is the junction capacitance and q is the charge stored on this capacitance. This charge q can be written as $2en$ where e is the charge on one electron, and n is the discrete number of Cooper pairs that have tunnelled through the junction barrier [20]. Therefore, the energy associated with the junction capacitance can be rewritten as

$$E_{CJ} = 4E_C n^2$$

where $E_C = \frac{e^2}{2C_J}$. The net energy associated with the Josephson Junction is the summation of the energy due to the effective inductance and the capacitance.

$$\begin{aligned} E_{tot} &= E_{CJ} + E_L \\ E_{tot} &= 4E_C n^2 - E_J \cos\varphi \end{aligned}$$

With the energy described using E_C and E_J, we tune these parameters to change the states of the qubit configuration using Josephson Junctions. The starting point for qubit realizations using Josephson Junctions is the charge qubit known as the Cooper Pair Box. The Josephson Junction is coupled to capacitances, and a Voltage source forms the **Cooper Pair Box** (CPB) as explained in the following section [21].

1.1.1. Cooper Pair Box

To fashion a system as a qubit, the energy of the system must be able to be defined using distinct energy levels. Such a system should have at least two isolated energy levels, and the system must be able to transit between these energy levels by the application(or removal) of external energy. A secondary requirement a potential qubit system must have is that the difference in energy for consecutive energy levels must be different. That is, the energy it takes to drive the qubit from $|0\rangle \rightarrow |1\rangle$ must not be equal to the energy causing $|1\rangle \rightarrow |2\rangle$. This *Anharmonicity* is required so that driving between energy levels can be done easily. Here, we show that the setup of a Cooper Pair Box displays both the requisite characteristics for the realization of a qubit.

The CPB, as shown in Figure 1.3, is designed as a Josephson Junction with a junction capacitance of C_J connected to a voltage source ($V_g(t)$) via a gate capacitance C_g. A Josephson Junction is described using the symbol $\times$.

In this setup, the single electron charging energy can be written as

$$E_C = \frac{e^2}{2C_\Sigma}$$

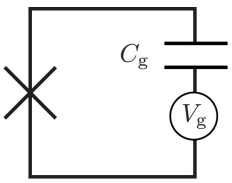

Figure 1.3: Circuit diagram of a charge qubit [22]

where $C_\Sigma = C_g + C_J$. Taking 'n' as the discrete number of Cooper electron pairs tunnelling through the barrier, the total charge q accumulated on the capacitances can be written as $q = -2en$.
Similar to the Josephson Junction, the energy related to capacitances in this setup can be written as

$$E_{CJ} = 4E_C(n - n_g)^2$$

where n_g represents the charge from the Voltage $V_g(t)$. The total energy of this Cooper Pair Box setup is then written as

$$E_{tot} = E_{CJ} + E_L \tag{1.8}$$
$$E_{tot} = 4E_C(n - n_g)^2 - E_J \cos\varphi \tag{1.9}$$

So far, we have been detailing the system's energy using classical variables. Ultimately, this has to be regarded as a quantum mechanical system, so it would be better to describe the system in terms of the Hamiltonian and quantum operators. Classically, a system's characteristics are described using measurable quantities such as velocity, power etc. These quantities are measurable and possess a specific value. However, in quantum, the observable physical quantities no longer have a fixed value that can be computed easily. Therefore, to measure a particular quantity, we associate it with a quantum operator that operates on a quantum state to give as output the measured value. We define a quantum state using the state vector $|\Psi\rangle$, on which acts a quantum operator $\hat{q}$ that gives as output the observed value of quantity q [23].
In the CPB setup, we define the quantum operator $\hat{n}$, which is used to compute the discrete number of Cooper pairs that tunnel through the insulating barrier compared to the number at the equilibrium state. This operator is used as $\hat{n}|n\rangle = n|n\rangle$ where $|n\rangle$ depicts the charge states of the junction and n is the eigenvalues of an operator acting on its eigenvectors[24]. We consider the charge states to form the eigenbasis for convenience. Therefore the Hamiltonian detailing the energy related to the capacitance can be rewritten as

$$H_c = E_c \sum_n (n - n_g)^2 |n\rangle\langle n|$$

The Josephson phase is taken as the other quantum operator $\hat{\varphi}$. Then, the energy related to the junction is rewritten using the charge state description [19]

$$-E_J \cos\varphi = -\frac{E_J}{2} \sum_n |n\rangle\langle n+1| + |n+1\rangle\langle n|$$

where E_J is the same value discussed in Equation 1.7. Therefore, the net Hamiltonian for the CPB is

$$H_{net} = E_c \sum_n (n - n_g)^2 |n\rangle\langle n| - \frac{E_J}{2} \sum_n |n\rangle\langle n+1| + |n+1\rangle\langle n| \tag{1.10}$$

From the Equation 1.10, it can be seen that the charge states of the CPB can be adjusted via the parameter n_g using the input Voltage $V_g(t)$. Half-integer values of n_g are chosen since, at these points, the two lowest energy levels are well separated, making for an easier transition between charge states [25]. Further modifications added to this base setup of a Cooper Pair box lead to the configuration of the transmon.

1.1.2. Transmon

The transmon is a design of a superconducting quantum bit that has been shown to have reduced charge noise sensitivity compared to the Cooper Pair Box qubit structure discussed in Section 1.1.1. A primary motivation of this design was to improve the qubit coherence time, i.e., the time for the qubit can retain the encoded information. A transmon consists of two Josephson Junctions attached in parallel to a capacitance

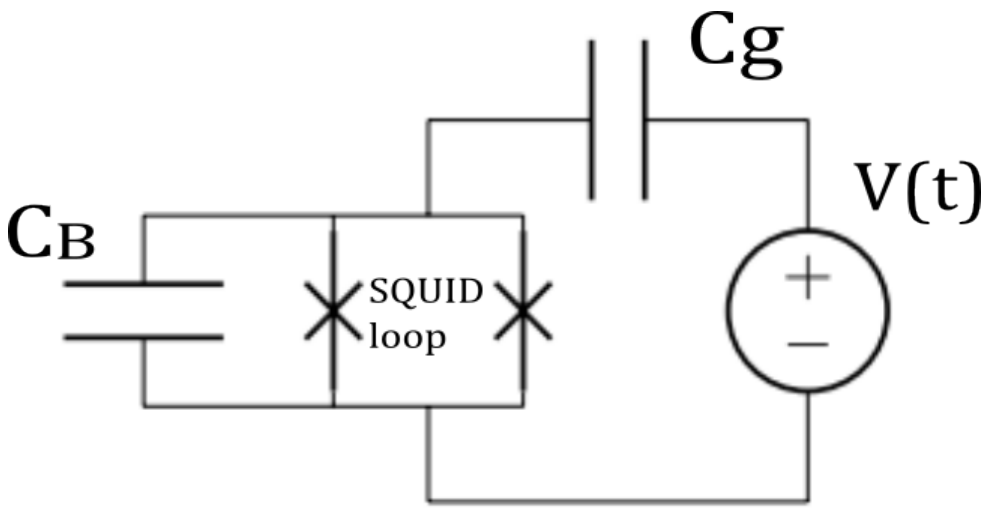

Figure 1.4: Design of Transmon [25]

(C_B), which is then connected to the voltage source via a gate capacitance (C_g) as shown in Figure 1.4. Two Josephson junctions in parallel form a **S**uperconducting **QU**antum **I**nterference **D**evice (SQUID), which is then employed to adjust the E_J of the setup using an external magnetic flux [26]. The energy of the system can still be quantified using Equation 1.10. By adding the large capacitance C_B, the energy E_C is tamped down relative to E_J ensuring that the transmon operates in the regime where $E_J >> E_C$.

Now, on analysing the energy versus input voltage relation, we obtain the Figure 1.6. Taking the energy required for causing the excitation from the ground level to the first excitation level as E_{01}, Figure 1.5 shows the Energy levels $E_m \forall m \in \{0,1,2\}$ calculated for the Hamiltonian 1.10. As mentioned in the previous section, by operating the qubit at half-integer values of n_g, the sensitivity to noise that causes the qubit to excite is reduced. It can be seen from Figure 1.5 that at half-integer values of n_g, linear noise cannot cause the qubit to transit to higher energy levels. However, this method does not protect the qubit system from being susceptible to large fluctuations that can drive the qubit away from operating at half-integer values. Therefore, to account for this, the design of the transmon qubit increases the ratio $\frac{E_J}{E_C}$. Figure 1.6 shows an example where the $\frac{E_J}{E_C} = 50$. From here, it can be seen that increasing the ratio of $\frac{E_J}{E_C}$, the prospect of being affected by the noise which causes the qubit to deviate from the optimal spot of operation, is reduced.
Experimental implementation of the transmon qubits has shown that the qubit coherence time can be extended up to $100\mu s$ [27]. The experiments, such as the ones object of this thesis, are typically controlled using software that controls the transmon quantum computing setup. The experiment coded in a high-level language (Python in this thesis) is first compiled into instructions understandable by the control electronics. This compilation step differs for the various quantum control electronics available. The quantum control electronics send signals to the dilution refrigerator, which houses the qubit chip. The output of the experiments is collected using a readout signal from the control electronics. Chapter 1 of [28] and the paper [29] explains in detail the experiment flow from software to hardware. For the sake of this thesis, we do not examine the nuances here and consider the final qubit state measurement data obtained from the readout (Chapter 8 of [28]). For the experiments conducted, expectation values are calculated from the qubit state data before further processing.
Expectation Values for measured states on the Z - axis (measurement axis - $|0\rangle$ and $|1\rangle$) are mathematically calculated as

$$\begin{aligned} E_\psi(Z) &= \langle\psi| Z |\psi\rangle \\ &= \langle\psi| (|0\rangle\langle 0| - |1\rangle\langle 1|) |\psi\rangle \\ &= \langle\psi|0\rangle\langle 0|\psi\rangle - \langle\psi|1\rangle\langle 1|\psi\rangle \\ &= |\langle 0|\psi\rangle|^2 - |\langle 1|\psi\rangle|^2 \end{aligned}$$

where $|\psi\rangle$ is the qubit state vector measured in the Z axis [30].

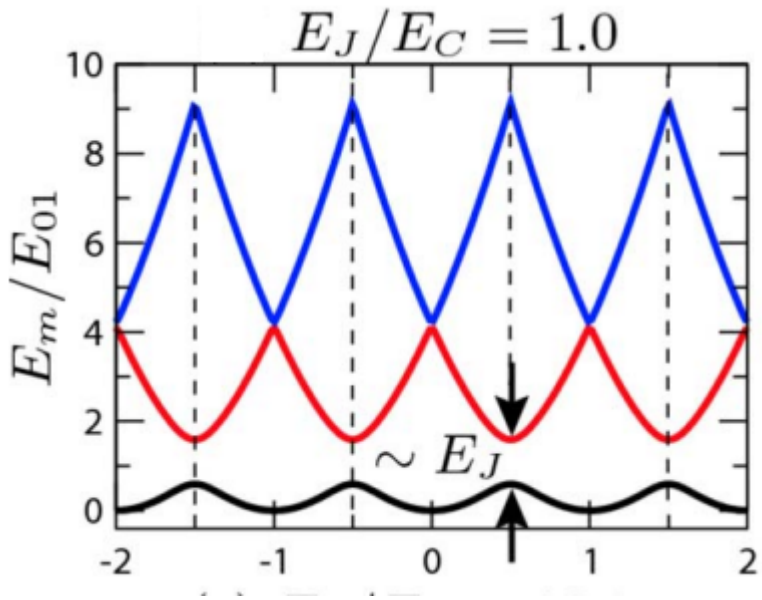

Figure 1.5: Eigenenergies of the Hamiltonian 1.10 for $\frac{E_J}{E_C} = 1$ [26]

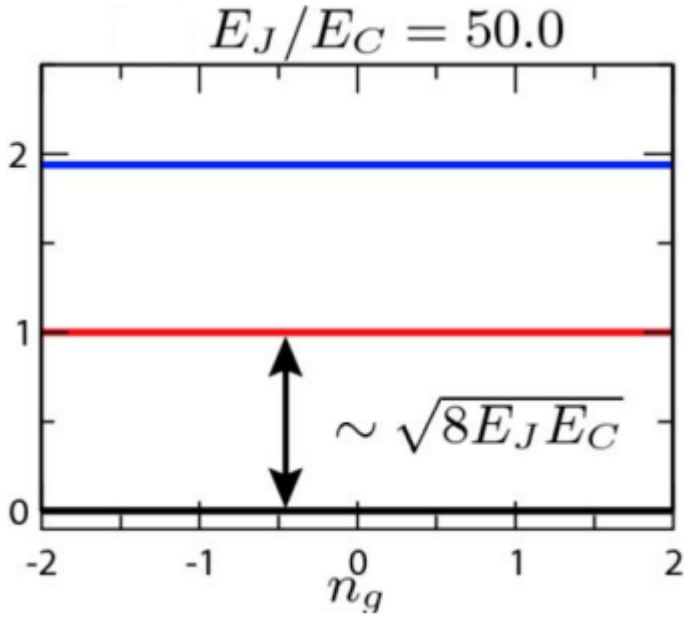

Figure 1.6: Eigenenergies of the Hamiltonian 1.10 for $\frac{E_J}{E_C} = 50$ [26]

1.2. Thesis Motivation

With quantum computing being a new field, optimising such systems is still a work in progress. The company at which this thesis was done, Orange Quantum Systems, uses superconducting quantum hardware called transmon. In transmon systems, with the addition of the control line to the qubit chip, calibrating this line also becomes important. Input qubit control signals from an arbitrary waveform generator (AWG) operating at room temperature undergo linear dynamical distortions as it traverses various electrical components on the control line connecting to the quantum device. If uncompensated for, such distortions can have detrimental effects on gate performance, affecting fidelity and even repeatability. Distortions introduced by components at room temperature (e.g., AWG bandwidth, high-pass filtering of a bias tee, and skin effect in instrumentation cable) are easily characterized using a fast oscilloscope. However, distortions introduced by components inside the refrigerator (e.g., low-pass filters, impedance mismatch, skin effect in semi-rigid coaxial cable, and chip packaging) are generally temperature-dependent. They are thus best characterized in the cold. Additionally, the on-chip response varies across devices and even between different qubits on the same device. Therefore, the ideal strategy for characterizing pulse distortion would be using the controlled qubit. Therefore, the motivation for this thesis was to study the distortions that occur on this line and the currently available methods that use the qubit itself for correction.

This work aimed to study and implement three distortion characterization methods for correcting the distortions on the control line of a transmon system. As mentioned earlier, the input qubit control signals in transmon systems are the main component used in tuning the qubit frequency by applying flux. To ensure that the qubit frequency is tuned perfectly, the distortions that arise on the flux pulses must be accounted for. For example, an operation that requires changing the qubit frequency would be the implementation of a two-qubit CPHASE gate. When there are distortions on the flux pulse that alters the qubit frequency, then coupling the qubits for implementing the CPHASE gate becomes difficult. Hence, methods/protocols that can achieve the same must be implemented before the qubit system can run other qubit-related experiments that require varying the qubit frequency.

1.3. Thesis Objective

The main goal, as mentioned previously, of this thesis is to study and implement three distortion-correcting protocols for improving the signal on the flux bias line in a transmon system. Therefore, the main objectives are -

1. To study the configuration of transmon hardware. This is done to understand how flux affects the qubit system.
2. To study the three protocols of the Cryoscope, Chevron and Ramsey using Kelly's method and to understand the variations in the individual protocols.
3. To implement the said protocols on software by first drawing up its algorithm and then programming it.
4. To run the experiments on actual quantum hardware after their software-level Implementation.
5. To implement a method that compares the distortion-characterization methods using chosen performance metrics.

1.4. Organization of this report

The report is divided into five major chapters, followed by the conclusion. In Chapter 2, an introduction to noise observed in a single qubit system is given. Here, concepts of **Bloch Sphere Representation** of a single qubit, corresponding **single qubit noise characterization** methods and a brief explanation of two-qubit gates (**CPHASE**) are discussed. Since this report limits itself to flux-based noise identification, the next chapters elucidate three methods or protocols implemented to characterize flux distortions in qubit control pulses.
Chapter 3 discusses the **Cryoscope** method. Here, the **Principle**, which builds the method, the **Implementation** of the method and the **Analysis** of the qubit measurement data are illustrated. Detailed explanations of the **Results** both from simulation and actual experimental runs are also specified. The chapter concludes

with an account of the **Assumptions and Drawbacks** of this method.
Chapter 4 follows a similar structure to the previous chapter in detailing **Ramsey using Kelly's** method. It also begins with the description of the **Principle** behind the protocol, followed by the **Implementation** and the **Analysis**. The next section describes the **Results** from the simulated data, and the chapter is concluded with a discussion on the **Assumptions and Drawbacks** associated with this method.
The third method, the **Chevron**, is elaborated in Chapter 5 with the sections divided into **Principle**, **Implementation**, **Results** and **Assumptions and Drawbacks**. Chapter 6 contains the novel part of this thesis work, the comparison of implemented protocols.
The final chapter 7 briefly summarizes the distortion-characterization methods implemented. This chapter finishes with the **Future implementations** that can follow the methods discussed in this report.

2

Characterization of Noise

Qubits are susceptible to noise from the measurement equipment, the control equipment and the environment. This noise emerges as random processes on the qubit, which causes it to decohere [6]. The qubit state at any point can be calculated if its initial state and Hamiltonian are known, in the case of closed systems. When the qubit system is made an open system, there are interactions between the qubit and the environment, which causes fluctuations in the qubit state. As these fluctuations persist, the qubit loses its information, with the qubit state moving away from what is expected. Fluctuations (noise and fluctuations used interchangeably) that occur because of arbitrary changes in system parameters that affect the qubit are called **Stochastic Noise**. An example would be the uncontrollable variations in the amplitude of an input control signal. These unknown variations would then affect the qubit causing it to decohere. Stochastic Noise therefore would differ for every experimental run and so, cannot be predicted beforehand. **Systemic Noise** on the other hand quantifies the discrepancies that are known to arise due to a fixed process. For example, when driving a qubit to transit from the $|0\rangle$ to the $|1\rangle$, we assume that the transition causes the qubit to rotate exactly by 180° about the equatorial plane. However, in reality, the qubit driving system may cause a couple of extra degrees of rotation onto the qubit. This over/under rotation is always by a fixed amount generated by the system and therefore leads to the rotation error every time the pulse is applied. This error is termed as Systematic error and can be compensated for easily using proper calibration methods, unlike stochastic error. The effect of noise on the qubit can be easily visualized using the Bloch Sphere representation of the qubit state.

2.1. Bloch Sphere Representation

The Bloch Sphere is a unit sphere that is frequently used to describe a qubit system. The quantum states of $|0\rangle$ and $|1\rangle$ are placed on either end of the *z-axis*, also called the *longitudinal axis*. The equatorial plane of this sphere is the *transverse plane*, and the x and y axes are called the *transverse axes*. Figure 2.1 shows an example of a quantum state vector on the Bloch Sphere.
Any pure quantum state can now be represented as a vector, a point on the surface of this sphere [6]. With the help of the polar angle ($0 \leq \theta \leq \pi$), the azimuthal angle ($0 \leq \phi \leq 2\pi$) and the two quantization states ($|0\rangle$, $|1\rangle$), a quantum state vector can be written as:

$$\begin{aligned} |\Psi\rangle &= \alpha\,|0\rangle + \beta\,|1\rangle \\ &= \cos\left(\frac{\theta}{2}\right)|0\rangle + e^{i\phi}\sin\left(\frac{\theta}{2}\right)|1\rangle \end{aligned}$$

The quantum state vector, thus defined, is represented on the Bloch sphere by taking the polar angle ($0 \leq \theta \leq \pi$) to be the angle of the vector measured on the longitudinal axis. The azimuthal angle ($0 \leq \phi \leq 2\pi$) is the angle of the qubit state vector projection on the equatorial plane, measured from the positive x-axis [5]. The transverse plane angle (ϕ) plays an important role in the flux distortions characterization methods discussed in the following chapters.

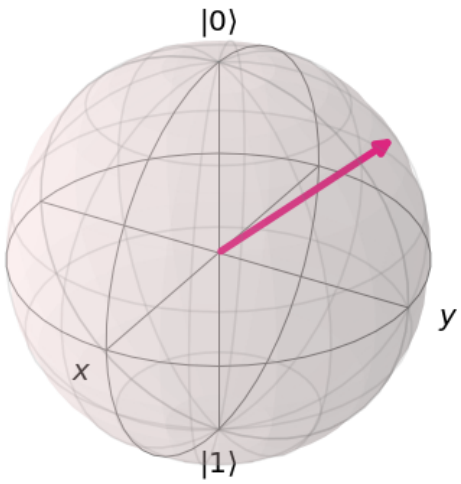

Figure 2.1: Example of a quantum state plotted on the Bloch sphere using Qiskit.

In this representation of the qubit state, the state vector is assumed to be stationary within the sphere. This assumption holds only when the Bloch sphere is taken to be a *rotating frame of reference*. In superconducting qubits, the energy of state $|1\rangle$ is higher than that of state $|0\rangle$. Therefore, when the qubit state is a superposition of the two polar states, this difference in energy causes the qubit state vector to precess around the z-axis with a frequency of $\frac{\omega_q}{2\pi} = \frac{E_{|1\rangle} - E_{|0\rangle}}{\hbar}$ (the qubit frequency). For easier visualization, the frame of reference is also taken to rotate around the z-axis with the same frequency as above. This precessing Bloch Sphere is the *rotating frame of reference* that causes the qubit state vector to appear stationary.
When the qubit state vector, due to some external factors (noise sources), does not rotate around the z-axis with the same frequency as mentioned above, we say that qubit is **detuned** from the reference rotating frame. This detuning causes a phase to occur on the final qubit state measurements and this phenomenon is an important part of the distortion correction protocols.

2.2. Longitudinal Relaxation of Qubit

Relaxation of the qubit along the longitudinal axis is the effect of noise that couples with the qubit via the transverse axes. Longitudinal relaxation is the shift in the qubit state on the longitudinal axis, i.e., the noise effect that causes the excited state (ground state) of the qubit to transition to the ground state (excited state). This effect originates from an energy exchange between the qubit and the environment leading to the qubit Up transition ($|\psi\rangle_{|0\rangle \to |1\rangle}$) and the qubit Down transition ($|\psi\rangle_{|1\rangle \to |0\rangle}$). In figure 2.2, the blue arc shows an example path of a possible qubit up and down transition.
Now, the longitudinal relaxation rate can be defined as the summation of the rate of Up transition and the rate of Down transition.

$$\begin{aligned} \text{longitudinal relaxation rate } \Gamma_1 &= \Gamma_{|0\rangle \to |1\rangle} + \Gamma_{|1\rangle \to |0\rangle} \\ &= \frac{1}{T_1} \end{aligned}$$

where in T_1 is defined as the net decay time over which the qubit population will relax to a steady state value. In superconducting qubits, the steady state value is the ground state ($|0\rangle$), with the longitudinal relaxation being mainly contributed by the Down transition. Using Boltzmann Equilibrium statistics, it can be derived that

$$\Gamma_{|0\rangle \to |1\rangle} = (e^{\frac{-\hbar\omega_q}{k_B T}})\Gamma_{|1\rangle \to |0\rangle} \tag{2.1}$$

where ω_q is the qubit frequency, k_B is the Boltzmann constant and T is the operating temperature[31]. Transmon qubits generally operate around temperatures of $T \approx 20mK$ and with qubit frequencies close to $\omega_q \approx 5GHz$. At these values, from Equation 2.1, it can be seen that due to the exponential function, the up

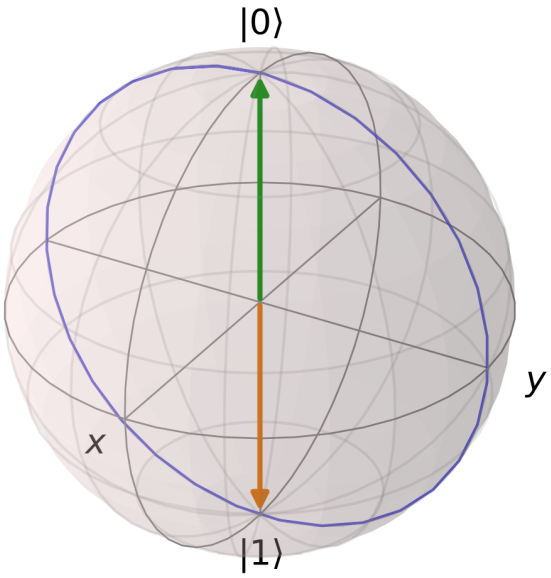

Figure 2.2: Bloch Sphere showing depolarization.

transition rate is vastly repressed and, therefore, can be taken as negligible.
In simple terms, superconducting qubits operate at cryogenic temperatures and are encoded with information by applying external energy sources such as the drive field and flux changes. Hence in the absence of these external energy suppliers, the qubit state will collapse to the steady state value since the qubits are more prone to losing energy than vice versa at cryogenic conditions.
Longitudinal relaxation for superconducting qubits can then be expressed as -

$$\begin{aligned}\Gamma_1 &= \Gamma_{|1\rangle\rightarrow|0\rangle} \\ &= \frac{1}{T_1}\end{aligned}$$

where T_1 is the relaxation time taken for the excited state of the qubit to lose its information and collapse to the ground state. Calculation of T_1 is an important method of characterizing a qubit since it provides insight into how long the qubit can retain the excited state. The experiment to calculate the T_1 times of a qubit is one of the first basic steps of qubit characterization. In order to measure the T_1 time, the transmon qubit is first reset to $|0\rangle$ state and then driven to the excited state using its particular qubit transition frequency ($|\Psi\rangle_{|0\rangle} \rightarrow |\Psi\rangle_{|1\rangle}$). After reaching its excited state, the qubit is measured at a particular duration, and the process is repeated again by varying the measurement times. This is done to get an estimate of the qubit state population at each measurement time. Repeated measurements are made in order to obtain the average estimate of the state population.
In Figure 2.3, it can be observed that the measurement time (shown as Delay times) increases as the population in $|1\rangle$ state decreases. By fitting an exponential decay curve to the data points, T_1 relaxation time is calculated by extracting the value τ from the curve. In general, the qubits less susceptible to noise would be the ones with longer T1 times, i.e., qubits that can preserve the higher energy state with slow decay rates.

2.3. Transverse Relaxation of Qubit

The qubit state is affected by two major relaxation rates - *longitudinal relaxation* as discussed in Section 2.2 and *transverse relaxation*. ***Transverse relaxation*** is used to quantify the net loss of information of a quantum

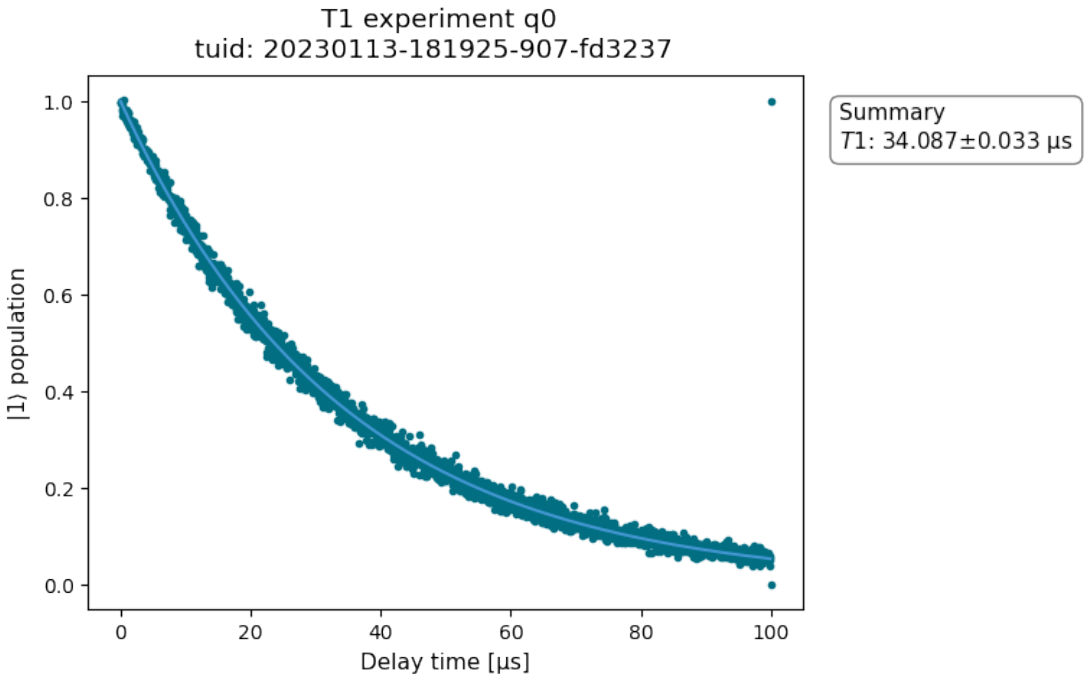

Figure 2.3: T1 relaxation of $|1\rangle$ state

superposition state. Therefore, Transverse relaxation of the qubit is defined as:

$$\Gamma_2 = \frac{\Gamma_1}{2} + \Gamma_\phi \tag{2.2}$$

$$= \frac{1}{T_2} \tag{2.3}$$

where Γ_1 is the longitudinal relaxation rate and Γ_ϕ is the Dephasing rate.
Qubit state change along the *transverse axes* due to noise is called *Pure Dephasing*. Pure Dephasing, quantified using the dephasing rate Γ_ϕ, originates from noise coupled to the qubit via the *z-axis*. This noise gives rise to fluctuations in the qubit frequency ω_q, which in turn makes the state vector precess with a frequency different to the frequency of the rotating frame of reference. This dissimilarity makes the qubit state vector appear as if it is rotating on the transverse plane in the rotating frame. Dephasing noise affects the azimuthal angle ($0 \leq \phi \leq 2\pi$), eventually making the qubit lose the information along the transverse axes.
Dephasing, unlike longitudinal relaxation, is not produced only by noise frequencies close to the qubit transition frequency. All frequencies of noise can modify the qubit and generate changes that emerge as an excess phase in the transverse axes. As observed in Section 2.2, there is an exchange of energy between the environment and the qubit system in case of longitudinal relaxation, and so, it is an irreversible process. In contrast to this, Dephasing is a reversible process since there is no exchange of energy with the environment and can be done using various methods [32].

2.3.1. Ramsey Experiment

Transverse relaxation rate defined using Equation 2.2 is measured via the Ramsey Interferometry method. This experiment employs $\frac{\pi}{2}$ rotations of the qubit to create superposition states. As the first step, the qubit is reset to the $|0\rangle$ state to ensure that the starting point is always the ground state. Next, the qubit is driven to the equal superposition state with a microwave pulse that implements a $\frac{\pi}{2}$ rotation around the *x-axis*. With the qubit in the equatorial plane, the expected qubit state now would be $|\Psi\rangle = \frac{|0\rangle - i|1\rangle}{\sqrt{2}}$. At this juncture, in case dephasing occurs, the qubit state vector would revolve in the equatorial plane. A final $\frac{\pi}{2}$ rotation around the *x-axis* is implemented on the qubit after a certain delay, following which the qubit is immediately measured. By varying the wait times (also known as Delay times) in between the rotation pulse (the first $X90$

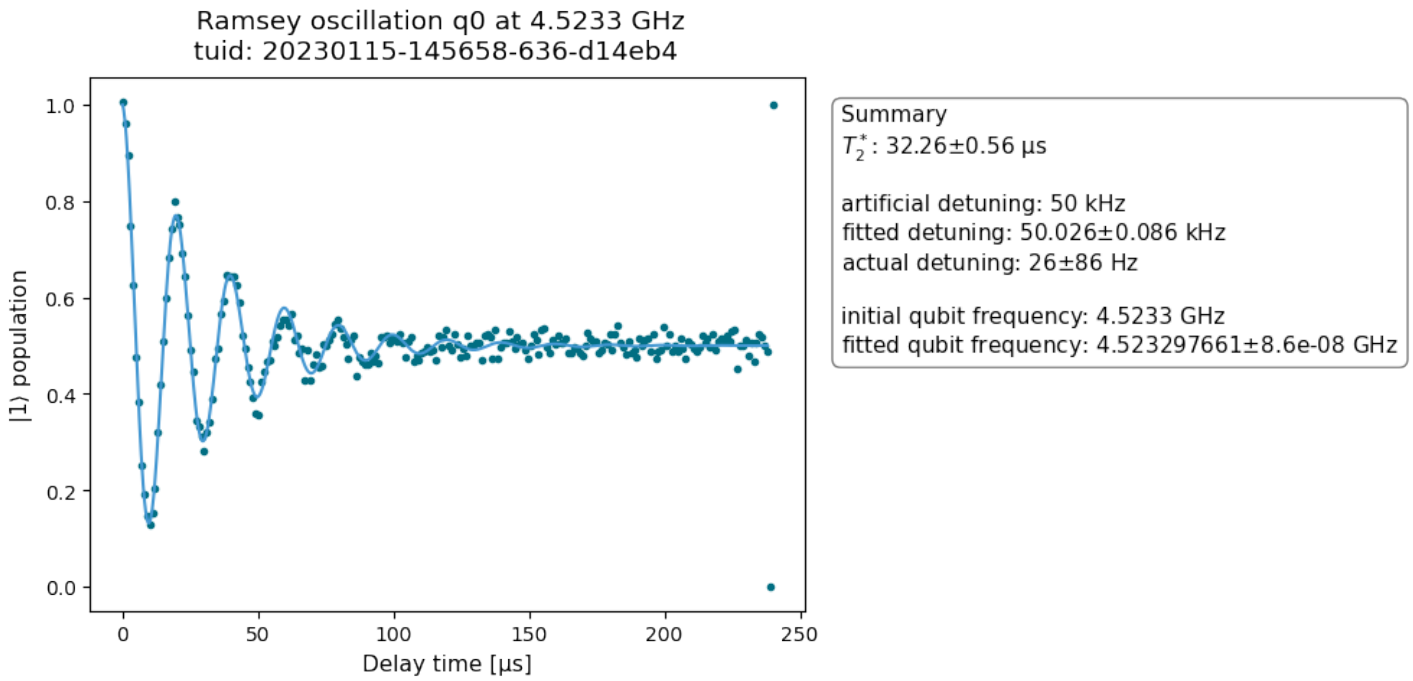

Figure 2.4: Ramsey experiment using simulated data

pulse and the ending $\frac{\pi}{2}$ pulse), and repeating the experiment, distinct phase points of the qubit state vector on the equatorial plane are found. Figure 2.4 displays the state population of $|1\rangle$ from the Ramsey experiment conducted using simulated data. In this example, the simulated qubit has a qubit frequency of 4.5233 GHz and an artificial detuning of 50MHz. *Artificial Detuning* is the method of shifting the qubit frequency from the original qubit frequency at the input on purpose. This is done to initiate oscillations of the qubit state on the equatorial plane to enable easier analysis. By specifying the artificial detuning value, that is by how much the qubit frequency differs from the primary qubit frequency, the expected dephasing in an ideal situation is known. Therefore, the output dephasing is easier to compute with the known value of the dephasing.
In the absence of any dephasing, the transverse relaxation rate is governed only by the longitudinal relaxation of the qubit and so, the graph from the Ramsey experiment would resemble Figure 2.3 of the T1 experiment. When dephasing noise elements are present, the state of the measured qubit oscillates in accordance with $\delta w_q(t)$. $\delta w_q(t)$ is defined as the difference in the original qubit frequency and the qubit frequency affected by dephasing elements. Initially, the dephasing rate dominates the transverse relaxation causing wide oscillations in the state population. As the delay times increase, the longitudinal relaxation takes over and so the state population settles at the superposition state. The T_2 decay rate is calculated by computing the decay of the exponential envelope fitted to the graph. The end state is a superposition state because the qubit for long delays would have relapsed back to the $|0\rangle$ state. And so, on applying the terminal $\frac{\pi}{2}$ pulse about the *x-axis* would take the state to the superposition state.

2.4. Magnetic Flux noise

Flux-tunable superconducting qubits, such as the transmons, are affected by random fluctuations that arise in the biasing magnetic flux. These arbitrary fluctuations are assumed to be perpetrated by unpaired electrons that are excited due to thermal variations within the SQUID loop [33]. In the given configuration of the transmon qubit, the flux noise is coupled to the qubit through the *z-axis*. Therefore, it primarily contributes to dephasing noise, which is estimated as Γ_ϕ.
The frequency of a transmon is controlled by the magnetic flux through the SQUID loop [34]. The magnetic flux is changed by sending known voltages in the bias line of the transmon system [35]. By changing the qubit frequency, the transmon is effectively detuned from the drive field, which is required for coupling it to another qubit at a lower frequency. Qubit-qubit coupling is essential for the realization of multi-qubit gates and so high levels of interaction between the qubits are required [36]. For maximal interaction between two

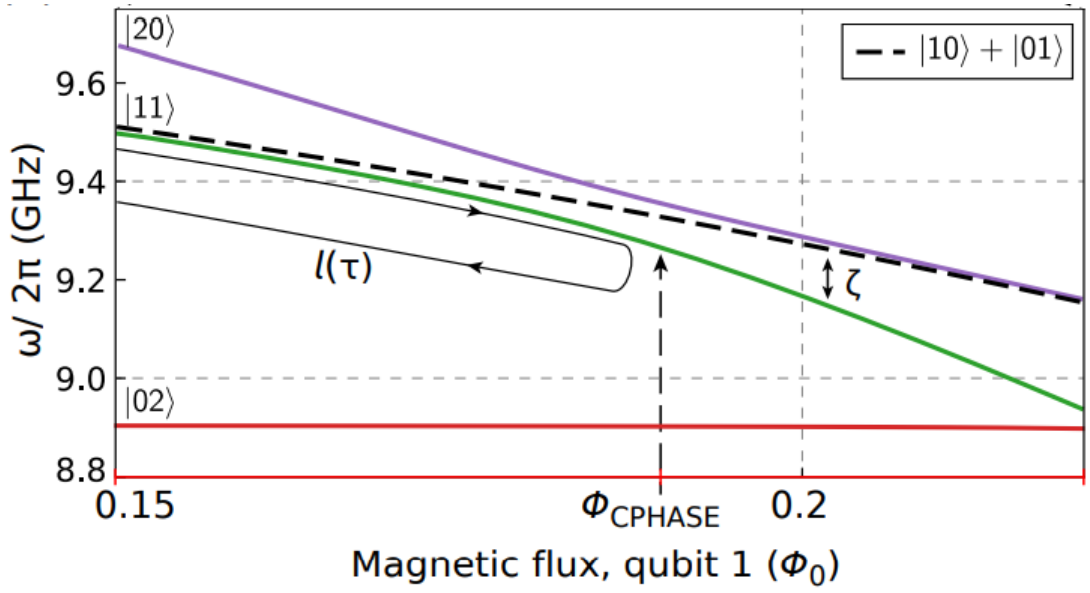

Figure 2.5: Energy vs Magnetic Flux in a two-qubit system [6]

qubits, the detuning has to be as ideal as possible, which in turn means that the flux-based fluctuations (distortions) in the qubit must be minimized. Many methods for characterization of flux-based noise currently exist.
In the current report, three methods that employ the qubit itself for flux noise characterization are discussed. These protocols are used to identify the noise affecting the qubit control pulses that implement the flux change in the transmon qubit. The same qubit system for two-qubit experiments is used in these protocols to capture the distortions induced by noise. This is due to the fact that the distortions occur at cryogenic temperatures and so any reference device might display different effects compared to the actual qubit itself. Therefore, any noise corrections made using a reference device might not be effective in the actual qubit system and so, would be useless in characterizing the actual qubit control pulse distortions.

2.5. CPHASE gate

Two qubit gates are obtained by relying on the qubit-qubit interactions in the system. One such implementation is using a flux tunable qubit coupled to a fixed frequency qubit [37]. Using this implementation, the primary implementation of a **CPHASE** gate has been experimentally shown to have high fidelities [38]. The variable frequency transmon qubit in such cases is modulated by using the flux through the qubit [39]. Therefore, producing a distortion-less signal that controls the flux biasing in the tunable qubit is of utmost importance to the realization of two-qubit gates. As an example, the working and implementation of the two-qubit CPHASE gate are discussed to view how much a distorted control signal affects its successful implementation. A CPHASE gate can be described using the unitary

$$U_{CPHASE} = \begin{bmatrix} 1 & 0 & 0 & 0 \\ 0 & 1 & 0 & 0 \\ 0 & 0 & 1 & 0 \\ 0 & 0 & 0 & -1 \end{bmatrix}$$

From the unitary, it is seen that when the state of the two-qubit system is $|11\rangle$, the application of a CPHASE causes a π phase shift on the excited states. That is, $|11\rangle \xrightarrow{CPHASE} -|11\rangle$. To implement the CPHASE gate, the avoided crossing between higher energy states of $|11\rangle \leftrightarrow |02\rangle$ is used. After preparing the excited state $|11\rangle$, magnetic flux is applied on the tunable qubit (denoted as qubit 1) slowly moving the combined state towards the region of avoided crossing. An example is shown as the grey trajectory in Figure 2.5. In doing so, the

system incurs phase on its states which is equivalent to applying a unitary defined as -

$$U_{phase} = \begin{bmatrix} 1 & 0 & 0 & 0 \\ 0 & e^{i\theta_{01}(\tau)} & 0 & 0 \\ 0 & 0 & e^{i\theta_{10}(\tau)} & 0 \\ 0 & 0 & 0 & e^{i\theta_{11}(\tau)} \end{bmatrix} \tag{2.4}$$

The phase acquired on varying the pulse is quantified as $\theta_{ij}(\tau)$.

$$\theta_{ij}(\tau) = \int_0^{\tau)} \omega_{ij}(t)dt$$

ω_{ij} as shown in Figure 2.5 is influenced by the applied magnetic flux Φ_0. A new parameter ζ is defined which denotes the phase acquired by $|11\rangle$ state relative to the other two states.

$$\zeta = \omega_{11} - (\omega_{01} + \omega_{10})$$

Therefore, the trajectory followed should yield a relative phase of π on the excited state of $|11\rangle$. To obtain a π phase on the excited state $|11\rangle$,

$$\begin{aligned} \int_0^{\tau} \zeta(t)dt &= \pi \\ \int_0^{\tau} \omega_{11}(t) - (\omega_{01}(t) + \omega_{10}(t))dt &= \pi \\ \Rightarrow \theta^l_{11}(\tau) - (\theta^l_{01}(\tau) + \theta^l_{10}(\tau)) &= \pi \\ \theta^l_{11}(\tau) &= \pi + (\theta^l_{01}(\tau) + \theta^l_{10}(\tau)) \end{aligned}$$

where $\theta^l_{ij}(\tau)$ depicts the particular phase acquired along the trajectory l. Replacing the values in Equation 2.4, the unitary becomes -

$$\begin{aligned} U_{phase} &= \begin{bmatrix} 1 & 0 & 0 & 0 \\ 0 & e^{i\theta^l_{01}(\tau)} & 0 & 0 \\ 0 & 0 & e^{i\theta^l_{10}(\tau)} & 0 \\ 0 & 0 & 0 & e^{i\theta^l_{11}(\tau)} \end{bmatrix} \\ &= \begin{bmatrix} 1 & 0 & 0 & 0 \\ 0 & e^{i\theta^l_{01}(\tau)} & 0 & 0 \\ 0 & 0 & e^{i\theta^l_{10}(\tau)} & 0 \\ 0 & 0 & 0 & e^{i(\pi+(\theta^l_{01}(\tau)+\theta^l_{10}(\tau)))} \end{bmatrix} \end{aligned}$$

The extra phase that is being brought upon the single-qubit states of $|01\rangle$ and $|10\rangle$ can be effectively cancelled by applying single-qubit pulses. On applying these pulses to both the qubits, the unitary can now be written as

$$\begin{aligned} U_{phase} &= \begin{bmatrix} 1 & 0 & 0 & 0 \\ 0 & e^{i\theta^l_{01}(\tau)} * e^{-i\theta^l_{01}(\tau)} & 0 & 0 \\ 0 & 0 & e^{i\theta^l_{10}(\tau)} * e^{-i\theta^l_{10}(\tau)} & 0 \\ 0 & 0 & 0 & e^{i\pi} * e^{i\theta^l_{01}(\tau)} * ei\theta^l_{10}(\tau) * e^{-i\theta^l_{01}(\tau)} * e^{-i\theta^l_{10}(\tau)} \end{bmatrix} \\ &= \begin{bmatrix} 1 & 0 & 0 & 0 \\ 0 & 1 & 0 & 0 \\ 0 & 0 & 1 & 0 \\ 0 & 0 & 0 & e^{i\pi} \end{bmatrix} \end{aligned}$$

This gives the expected unitary of a CPHASE operation ($e^{i\pi} = -1$). Therefore, the implementation of a CPHASE gate includes applying a magnetic flux to a tunable qubit coupled with a fixed-frequency qubit to take it to the region of higher level avoided crossing. This is then followed by the application of single-qubit pulses. There

is another method of implementing the CPHASE gate by taking it directly to the point of maximal interaction between $|11\rangle \leftrightarrow |02\rangle$, which works similarly to the iSWAP gate [6]. That has not been detailed here since it is not necessary for understanding the remainder of the thesis.
It can be seen that a close-to-perfection application of magnetic flux is a requisite for effectively tuning the qubit, as shown in Figure 2.5. Hence, protocols to correct flux-based noise are of utmost importance in realizing two-qubit gates. This thesis project aimed to study such methods and implement, analyse, and compare three of them. The implementation of the methods has been detailed in the following chapters.

3

Cryoscope

The **Cryo**genic oscillo**scope** (Cryoscope) is a flux-distortions characterization method that primarily uses the qubit response to reconstruct the input control pulse [28]. By varying the duration of a pulse of constant amplitude, the qubit state reflects these variations and the qubit measurements are used to reconstruct the pulse experienced by the qubit itself. This reconstructed pulse is the pulse which is seen by the qubit, including any non-ideality affecting the system. The goal of distortions characterization using the Cryoscope is to quantify these distortions caused by the non-idealities and provide for its correction.
The flux bias line is used in transmon systems to change the flux through the SQUID loop of the transmon, thereby causing the qubit frequency to change. When the qubit frequency is changed, the qubit is *detuned* from the drive frequency set before the change. This phenomenon of detuning the transmon qubit is very important for operations such as the implementation of the Conditional-Phase gate [40]. Therefore, the change in flux at the SQUID loop of the transmon has to be as ideal as possible for the successful implementation of flux-related operations. However, pulse information sent on the input flux line is affected by system noise and suffers distortions. These distortions on the input square pulse, in turn, cause disturbances in the amplitude of the applied flux, which impedes the qubit from detuning as expected. The Cryoscope, as mentioned earlier, is a method for detecting and correcting these distortions such that the flux pulse, as observed by the qubit, is ideal.

3.1. Principle

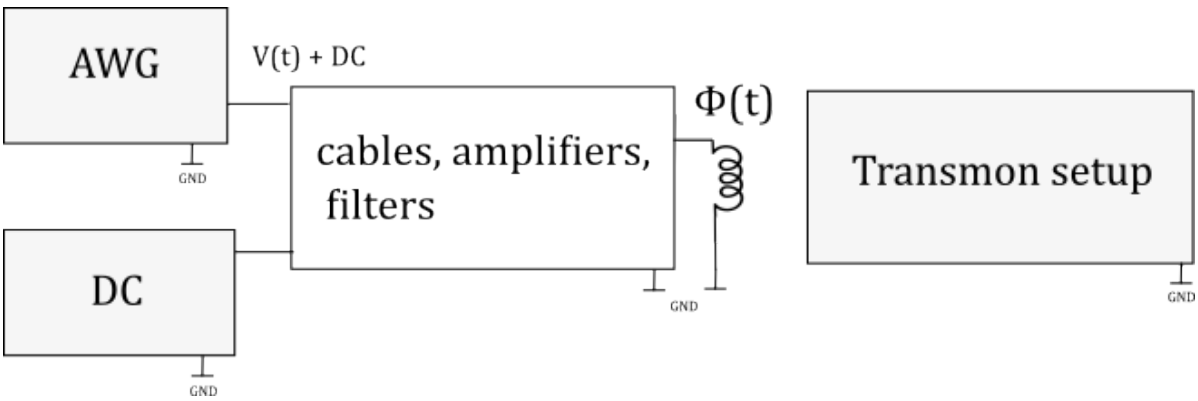

Figure 3.1: Schematic of the Cryoscope's control line

The transition frequency of the transmon qubit depends on the flux through the qubit in the following way:

$$f_Q(\Phi_Q(\tau)) \approx \frac{1}{h} * (\sqrt{8 * E_J * E_C * \left|\cos\left(\pi * (\frac{\Phi_Q(\tau)}{\Phi_0})\right)\right|} - E_C) \tag{3.1}$$

where: -

$\Phi_Q(\tau)$ – the external flux applied
f_Q – transition frequency of the transmon
Φ_0 – flux quantum
E_J – sum of the Josephson energies of individual junctions
E_C – charging energy of the shunt capacitor

With the qubit frequency affected profoundly by the flux, as shown through equation 3.1, it is imperative that the flux applied remains unaffected by any disturbances. This flux is applied through the control line of the qubit system by sending a voltage signal from an Arbitrary Waveform Generator (AWG). A block diagram depicting the main instruments of the control line of the Cryoscope is shown in Figure 3.1. This input control signal suffers distortions as it passes through the various electrical components on the control line. These distortions can occur due to the AWG response, skin effect in the connecting cables, and other effects due to filters and amplifiers [41]. In the presence of the distorted control signal, the flux received by the qubit is also similarly affected, leading to unwanted fluctuations in the qubit frequency. To identify these noise parameters, the Cryoscope experiment uses the qubit itself. The basic principle of the Cryoscope is to reconstruct the flux as seen by the qubit and correct for the deformations that appear on the reconstruction. In the Cryoscope experiment, the flux pulse is implemented by using a square input pulse. To reconstruct this square pulse fully, the experiment is repeated for multiple iterations, with each iteration implementing the pulse of different pulse widths. Figure 3.2 shows an example of the varying pulse. In accordance with this

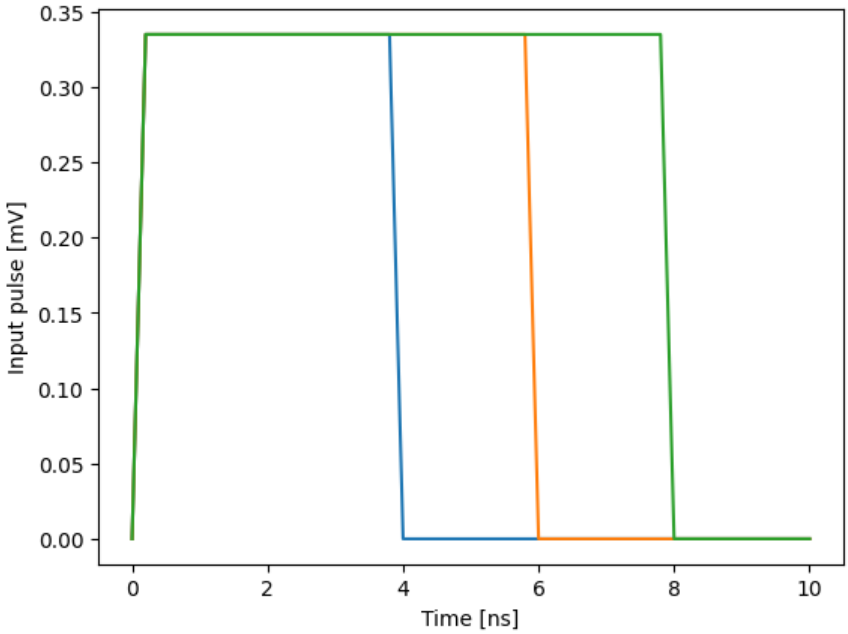

Figure 3.2: Example of pulses with different durations

example, in the first iteration of the cryoscope experiment, the input flux pulse is applied for 4ns. Therefore, the phase obtained by the qubit during these 4ns is reflected on the qubit and is measured via the output qubit state measurements. By measuring the phase at these varied pulse durations, the amplitude of flux that caused that particular value of phase acquired by the qubit is reconstructed.

However, in the absence of any flux, the qubit frequency is said to be at its maximal frequency, denoted by

$$f_{max} = f_Q(0) \approx \frac{1}{h} * (\sqrt{8 * E_J * E_C * \left|\cos\left(\pi * (\frac{0}{\Phi_0})\right)\right|} - E_C)$$
$$= \frac{1}{h} * (\sqrt{8 * E_J * E_C} - E_C)$$

The qubit is detuned from its maximal frequency by implementing an external flux $\Phi_Q(\tau)$ with varying time (τ) sandwiched between two $\frac{\pi}{2}$ rotation pulses. This flux $\Phi_Q(\tau)$ is directly dependent on the input control voltage $V_{in}(\tau)$, which is a square pulse of varying times (τ) of the pulse being ON. This $V_{in}(\tau)$ can be defined as

$$V_{in}(\tau) = \begin{cases} 1 & : 0 < \tau < T_{SEP} \\ 0 & : \text{elsewhere} \end{cases}$$

Here, T_{SEP} is the fixed separation time between the $pi/2$ pulses. The requirement of this fixed parameter and the method of using the phase to reconstruct the pulse is explained in the following section.
On measuring the qubit response to every τ, i.e., for every iteration with different pulse widths, the distorted voltage amplitude as seen by the qubit is reconstructed $(V_{noisy}(\tau))$. This reconstruction $V_{noisy}(t)$ is then used to compute the distorting parameters.

3.2. Implementation

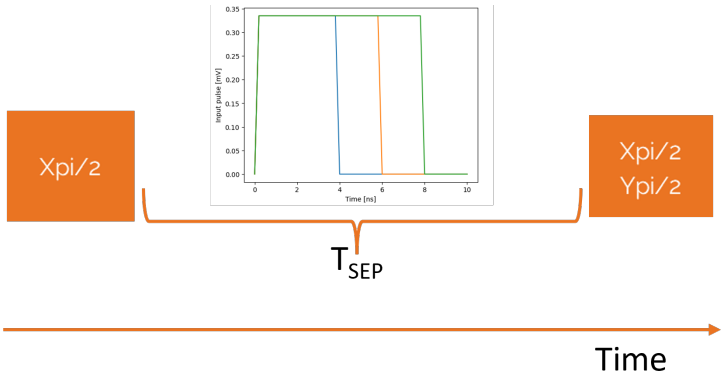

Figure 3.3: Block Diagram representing the Cryoscope implementation

The implementation of the Cryoscope is a variation of the Ramsey experiment explained in Section 2.3.1. Figure 3.3 shows the diagrammatical representation of the implementation. As shown, the qubit is first prepared at $|0\rangle$ and taken to the equatorial plane using a $X_{\pi/2}$ rotation, which is visualized as a 90° rotation about the X - axis in the anti-clockwise direction on the Bloch Sphere (refer section 2.1). After the qubit is rotated to the equatorial plane, a square pulse of fixed amplitude and varying pulse width is applied via the flux control line. This applied flux causes the qubit to detune from the drive frequency. This detuning can be visualized as the qubit state vector rotating on the equatorial plane of the Bloch Sphere in the clockwise direction. The frequency of this rotation on the equatorial plane is the frequency difference between the drive frequency and the qubit frequency after the application frequency. This frequency, also called the detuning frequency, has been defined below.

Qubit frequency in the absence of a flux pulse $(\Phi_Q(\tau) = 0)$ can be written as

$$f_Q(0) = \frac{1}{h} * (\sqrt{8 * E_J * E_C} - E_C) \tag{3.2}$$

When the flux pulse is applied, the qubit frequency is then described with equation 3.1, which is

$$f_Q(\Phi_Q(\tau)) \approx \frac{1}{h} * (\sqrt{8 * E_J * E_C * \left|\cos\left(\pi * (\frac{\Phi_Q(\tau)}{\Phi_0})\right)\right|} - E_C)$$

. Therefore, detuning frequency is the difference between the qubit frequency at $\Phi_Q(\tau) = 0$ (same as the drive frequency) and qubit frequency when the flux is applied. Using equations 3.1 and 3.2

$$\Delta f_{Q,detuning}(\tau) = f_Q(0) - f_Q(\Phi_Q(\tau)) \tag{3.3}$$

$$\Rightarrow \Delta f_{Q,detuning}(\tau) = \frac{(\sqrt{8 * E_J * E_C})}{h} * \left(1 - \sqrt{\left|\cos\left(\pi * (\frac{\Phi_Q(\tau)}{\Phi_0})\right)\right|}\right) \tag{3.4}$$

This detuning shows up in the qubit state measurements as the qubit phase $\phi(\tau)$.

$$\phi(\tau) = 2\pi * \int_0^{T_{SEP}} \Delta f_{Q,detuning}(\tau) d\tau$$

3.2.1. Relating the phase acquired by the qubit and its state probabilities

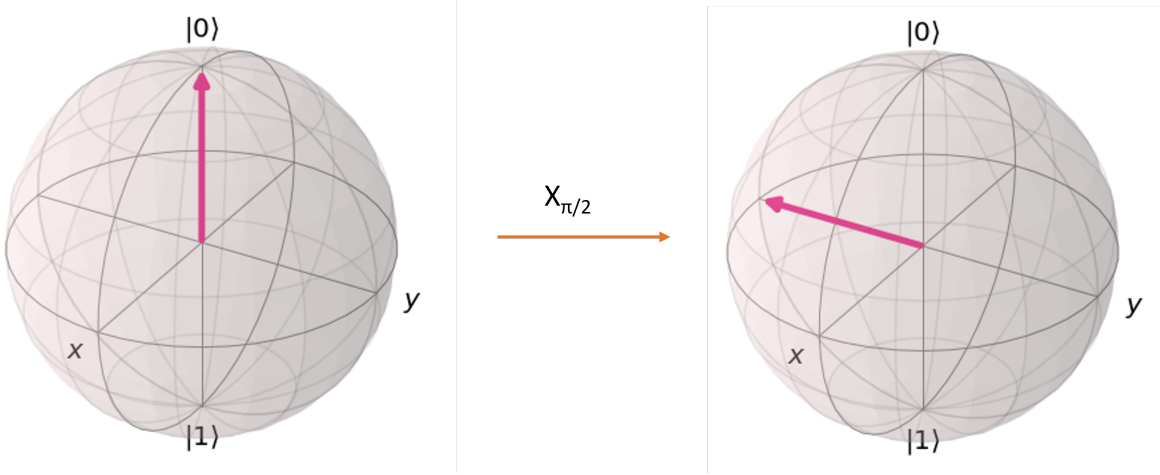

Figure 3.4: Bloch Sphere representation of $X_{pi/2}$ rotation

As mentioned previously, the detuning of the qubit causes the qubit to gain a phase. This phase depends on the flux applied $\Phi_Q(\tau)$. Figure 3.4 shows the effect of the initial $X_{pi/2}$ rotation performed on the qubit. The

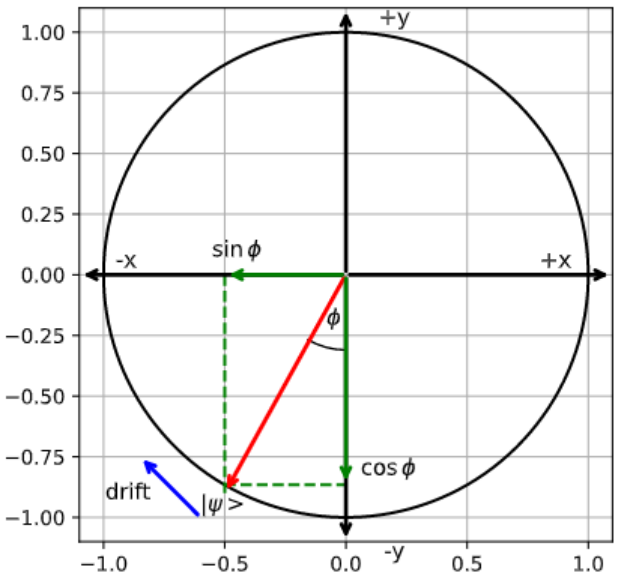

Figure 3.5: Equatorial plane representation of the qubit vector

initial $X_{\pi/2}$ rotation takes the qubit vector to the $-Y$ axis on the Bloch Sphere as per our representation. On

the equatorial plane, the qubit state vector precesses in the clockwise direction, thereby drifting towards the $-X$ axis. At the instance of the measurement where the qubit vector is stationary, the vector projections onto the $-Y$ axis and $-X$ axis are the $-\cos\phi$ and $-\sin\phi$ respectively as shown in Figure 3.5.As shown in Figure 3.3, a final $\pi/2$ around either the X axis or the Y axis is implemented after a time T_{SEP}. This parameter is kept constant between the two rotation pulses to ensure that the particular system-induced detuning is the same for all the iterations of the Cryoscope.
When the final rotation done is $X_{\pi/2}$, the projection vector $-\cos\phi$ is rotated about the X axis and is measured as $-\cos\phi|1\rangle$. Similarly, when the final rotation is $Y_{\pi/2}$, the projection vector $-\sin\phi$ is rotated about the Y axis and is measured as $-\sin\phi|1\rangle$. The measurement data received are the state probabilities that are measured

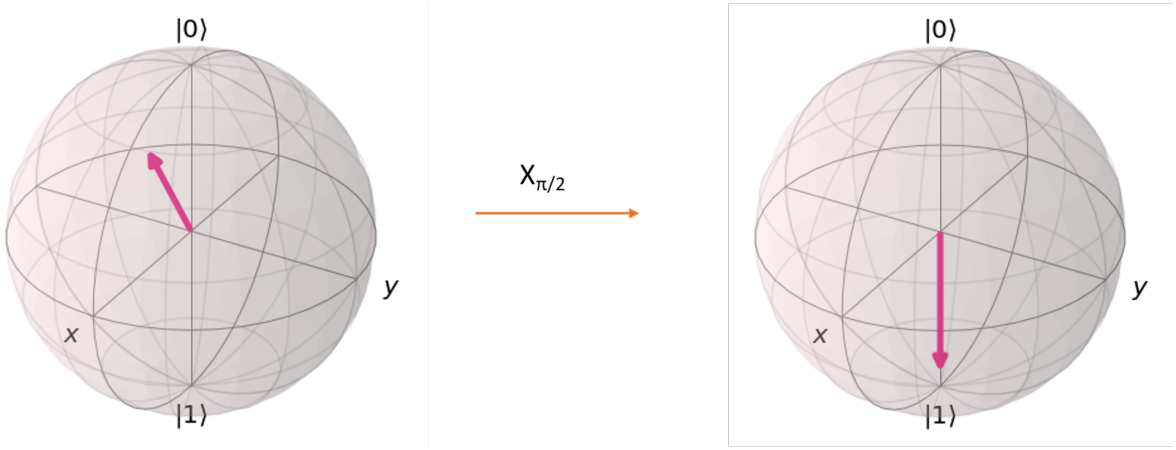

Figure 3.6: Final $X_{pi/2}$ rotation of an example qubit state in the presence of flux

after every iteration of the varying flux pulse (for every τ). Therefore, when the final rotation is the $X_{pi/2}$ rotation, the state probability is given by $|-\cos\phi|$. Figure 3.6 shows the Bloch sphere rotation of the qubit when the final rotation is $X_{pi/2}$. In this figure, the example shown has the qubit acquiring a phase of $\pi/8$. And so the state probability value from the measured data would be $\cos\pi/8$ (0.9238), as shown in this figure.
Similarly, when the final rotation is the $Y_{pi/2}$ rotation, the state probability is given by $|-\sin\phi|$. Figure

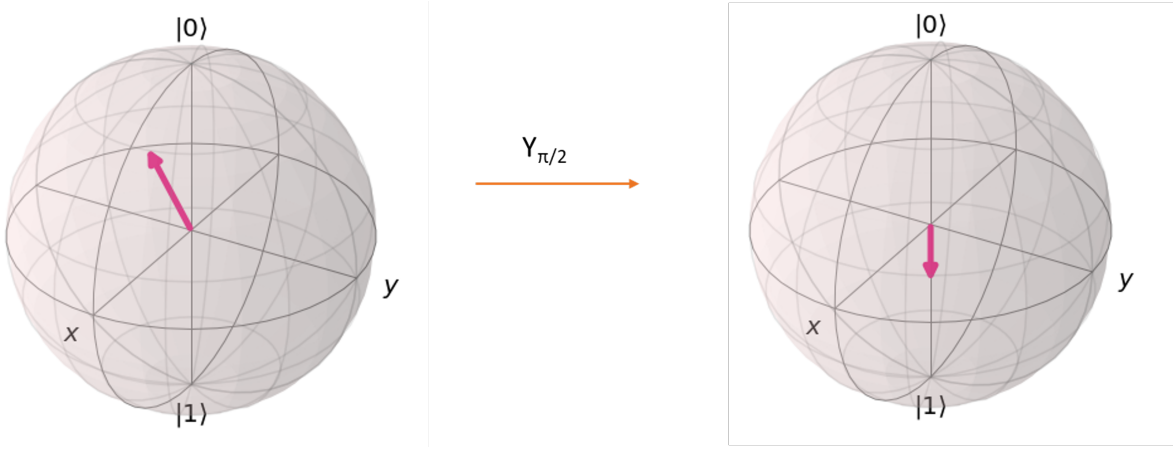

Figure 3.7: Final $Y_{pi/2}$ rotation of an example qubit state in the presence of flux

3.7 shows an example of this. In this figure, the state probability from the measured data would be $\sin\pi/8$ (0.3826). Please note that Figures 3.6 and 3.7 and the values above are only examples. These do not represent an actual qubit configuration from an experiment of the Cryoscope. These are only to be used to visualize how the rotations and detuning affect the qubit.

3.2.2. Implementation Conclusion

As mentioned earlier, the Cryoscope is a customization of the Ramsey experiment explained in Section 2.3.1. Therefore, these rotations are chosen using the principle behind the Ramsey experiment. All rotations have been visualized on the Bloch Sphere as anti-clockwise rotations of the qubit state vector about a particular axis. Hence, the final rotation is a 90° rotation about the X (Y) - axis.

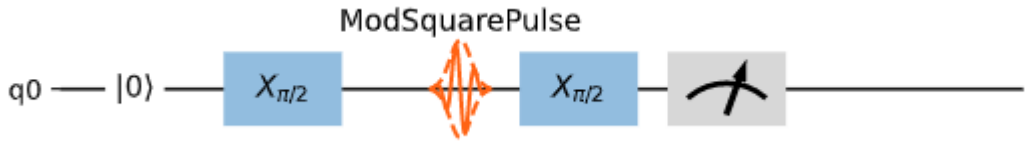

(a)

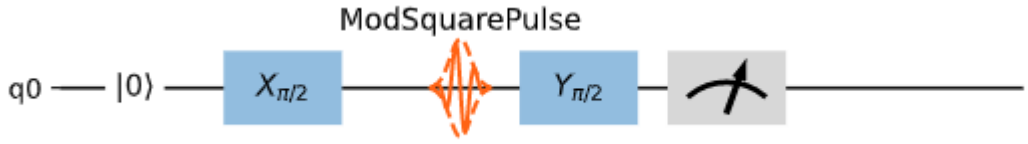

(b)

Figure 3.8: (a) Variation of the Cryoscope experiment with $X90$ final rotation
(b)Variation of the Cryoscope experiment with $Y90$ final rotation

The implementation of the Cryoscope experiment has been portrayed in the form of block diagrams in Figure 3.8. Both variations of the experiment were implemented using the qubit control software quantify-scheduler [42]. Here, the qubit and qubit operations are set as parameters in a *Schedule* which are then compiled to the hardware configuration before being executed on the experimental setup.

Listing 3.1: Code snippet showing Cryoscope Schedule *

```
sched = Schedule("Cryoscope")

sched.add(Reset(q0))  # initialize the qubits
sched.add(X90(qubit=q0)) # to rotate the qubit to the equatorial plane
square_pulse = sched.add(
    SquarePulse(amp=0.2, duration=1e-6, port="q0:res", clock="q0.ro")
) # adding square pulse

sched.add(Y90(qubit=q0)) # final Y rotation
sched.add(Measure(q0, acq_index=0)) # measurement
```

In the code snippet 3.1, we first initialize a *Schedule* with the name 'Cryoscope' and add operations in the required sequence to the initialized 'sched' parameter. We start with the qubit, specified as 'q0', *Reset* to ground state. With the qubit in $|0\rangle$, the gate and pulse operations are performed as shown in Figure 3.8b, which are followed by the *Measure* operation. This code is then compiled in accordance with the control electronics used, which adds the timing and other pertinent information.
After the code has been executed on the setup, the output from the readout is the qubit state measurements. These state measurements are the qubit state probabilities averaged for every iteration, where an iteration is a cryoscope run for one variant of the pulse width. Using the state probabilities, their respective expectation values are calculated as shown in section 3.3.2.

3.2.3. Simulation Implementation

With the implementation done for the actual experimental run, we developed a method to check if the data received from the experiment adheres to what is expected. For that, a simulation function that returns emulated data as expected from the experiment was done. To replace the characteristics of the real qubit that would affect the experiment, an object termed 'mock qubit' was used. This mock qubit object was hard-coded with dummy values for parameters such as qubit flux sensitivity, E_J Josephson energy, E_C charging energy etc. These mock parameters had multiple usages in the simulation function. The mock parameters of E_J and E_C were used to calculate the max qubit frequency, i.e. when the detuning is zero. From the user-defined input

* - A note - this code snippet is only an example. The implemented code is different and complex, with loops and reference points within the functions tailored to the format required by the company.

Schedule, the simulation function takes in the sequence of qubit operations.
When attempting to simulate the data, a mathematical relation that connects the input voltage pulse to the flux pulse affecting the qubit is needed. This relation between the voltage amplitude and flux amplitude can be written in simple terms as *Input Voltage* (V) = *mock qubit flux sensitivity* (V/Wb) $*$ *Flux* (Wb). By doing so, it can be seen that by increasing voltage amplitude, the flux also increased linearly, similar to how it takes place in the quantum backend. As the flux through the transmon increases, the qubit is detuned further with the relation following Equation 3.1. The detuning frequency is then computed by evaluating the difference between the max qubit frequency and the flux-affected frequency from the aforementioned equation.
Then, using the computed detuning frequency, the phase that the qubit vector (ϕ_{sim}) would have acquired for the given input amplitude of the pulse over the specified time scale is calculated. With the calculated phase information, the expectation values are computed as $\cos\phi_{sim}$ and $\sin\phi_{sim}$ for final rotations $X_{\pi/2}$ and $Y_{\pi/2}$ respectively. These calculated expectation values are then used as the equivalent experiment data to check the data analysis code. With the help of this simulation function, the data analysis procedure can be verified for its accurate working.
As a first step, the simulation environment was ideal without distortions on the flux pulse. Later, a function that adds linear distortions to the array holding flux pulse values was included. In doing so, the qubit phase calculated by the simulation function is affected by the presence of linear distortions similar to how it occurs in an actual experimental setup.

3.3. Analysis

The Analysis of the experimental data from the setup can be divided into five segments. Figure 3.9 shows

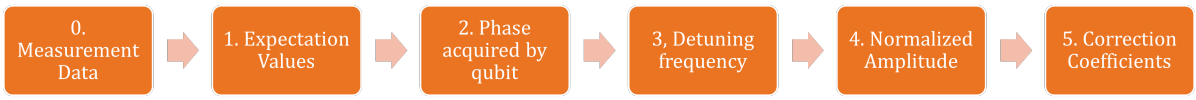

Figure 3.9: Flow of the Analysis section

the flow of the analysis procedure diagrammatically. First, the expectation values of the qubit readings are extracted from the measurement data. The measurement data from a Cryoscope run on the actual hardware returns the qubit state probabilities readout for each experiment iteration. Then, from the expectation values (either from simulation or hardware), the phase and detuning frequency are calculated. Finally, the flux amplitude and the filter coefficients to correct the distortions are computed. The subsections below elaborate on the individual segments of the procedure in detail with the corresponding graphs obtained from the simulation function.
The simulation was first run for an input square pulse of 0.1V with pulse duration varying from 0 ns to 60 ns. The analysis code executed for data from this simulation is used to demonstrate how the magnitude of input voltage amplitude affects the oscillating frequency of the expectation values. However, secondary simulation data was used to illustrate the analysis flow. This simulated data was acquired by using a square pulse of amplitude 0.335 V, with pulse duration varying from 0 ns to 60 ns.

3.3.1. Calculation of expectation values

The output data is received as state probabilities from which the expectation values of the measured qubit are extracted. There would be two sets of qubit measurements for the time-varying pulse, one for the final $X_{\pi/2}$ rotation and the other for the final $Y_{\pi/2}$ rotation. These two variations of the run are done to find the phase acquired by the qubit accurately. The expectation values calculated are denoted using $< X >$ and $< Y >$. $< X >$ and $< Y >$ signify the expectation values of the final $Y_{\pi/2}$ and $X_{\pi/2}$ rotation.
Figure 3.10 shows the expectation values obtained from the simulated data. The initial expectation values for the $X_{\pi/2}$ ($< Y >$) and $Y_{\pi/2}$ ($< X >$) variations are -1.0 and 0.0 as expected. This is because, in the absence of

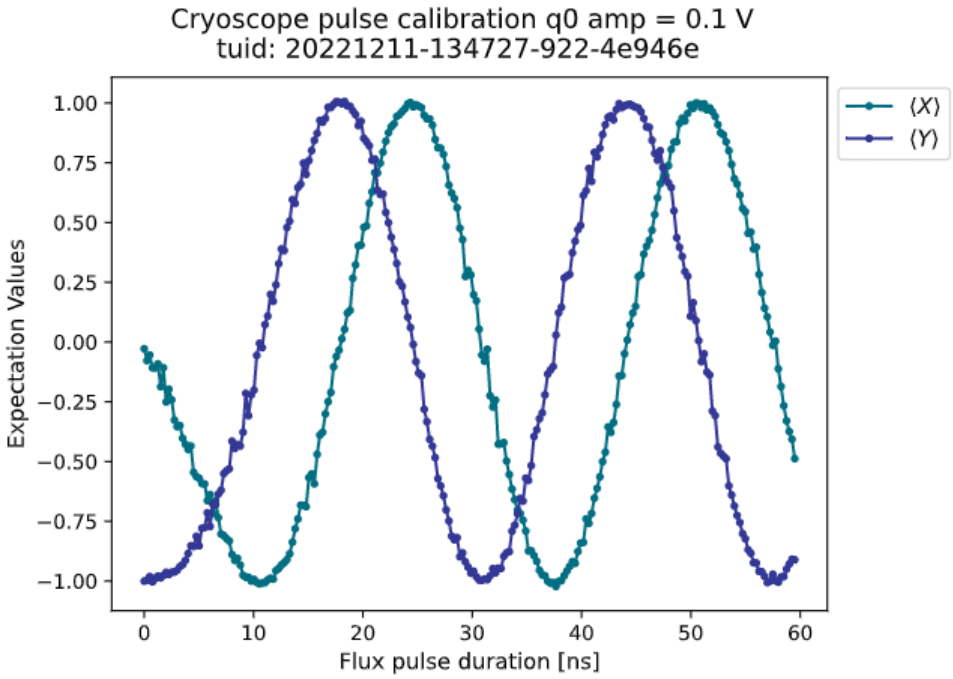

Figure 3.10: Graphical representation of the Expectation values obtained from simulated data for pulse amplitude of 0.1 V

a square pulse, the qubit does not face any detuning. Therefore, at 0 ns of the pulse duration (i.e., no pulse application and immediate measurement after final rotation), the final states of the qubit after $X_{\pi/2}$ and $Y_{\pi/2}$ rotations are $|1\rangle$ and $\frac{|0\rangle - i|1\rangle}{\sqrt{2}}$. Then the expectation values for these states after measurement in the Z basis are (refer section 1.1.2)

$$\begin{aligned} < Y > &= |\langle 0|1\rangle|^2 - |\langle 1|1\rangle|^2 \\ &= -1 \\ < X > &= \left|\langle 0| \frac{|0\rangle - i|1\rangle}{\sqrt{2}}\right|^2 - \left|\langle 1| \frac{|0\rangle - i|1\rangle}{\sqrt{2}}\right|^2 \\ &= \frac{1}{2} - \left|\frac{-i}{\sqrt{2}}\right|^2 \\ &= \frac{1}{2} - \frac{1}{2} \\ &= 0 \end{aligned}$$

Therefore, a good check would be to see if the starting data points after the calculation of expectation values are approximately 0 and -1 for $< X >$ and $< Y >$, respectively.

In the cases where the input pulse amplitude is high, the frequency of oscillation is equivalently high too. This is because the flux amplitude is directly proportional to the input amplitude as used in Section 3.2.3. Therefore, as the magnitude of the flux $|\Phi_Q(\tau)|$ surges up, the detuning experienced by the qubit also increases, which can be observed from Equation 3.4. Therefore the higher the detuning, the more the qubit state measurements oscillate. In some cases, when the input amplitude is high, the data obtained would encounter large detuning, making it tedious to extract phase information. Therefore, the highest frequency component from such measurement data was removed using demodulation to make further processing easier. This is demonstrated from graphs 3.10 and 3.11. It can be observed that for higher input amplitude, the frequency of the oscillating expectation values increases. Therefore, to compute the phase from such cases, first, the data is demodulated to remove the high-frequency component. This demodulation frequency is calculated by taking the Fourier transform of the data and selecting the highest frequency from the transformation.
From Figure 3.11, it can be seen that as the pulse amplitude increased to 0.335 V, the frequency of the oscil-

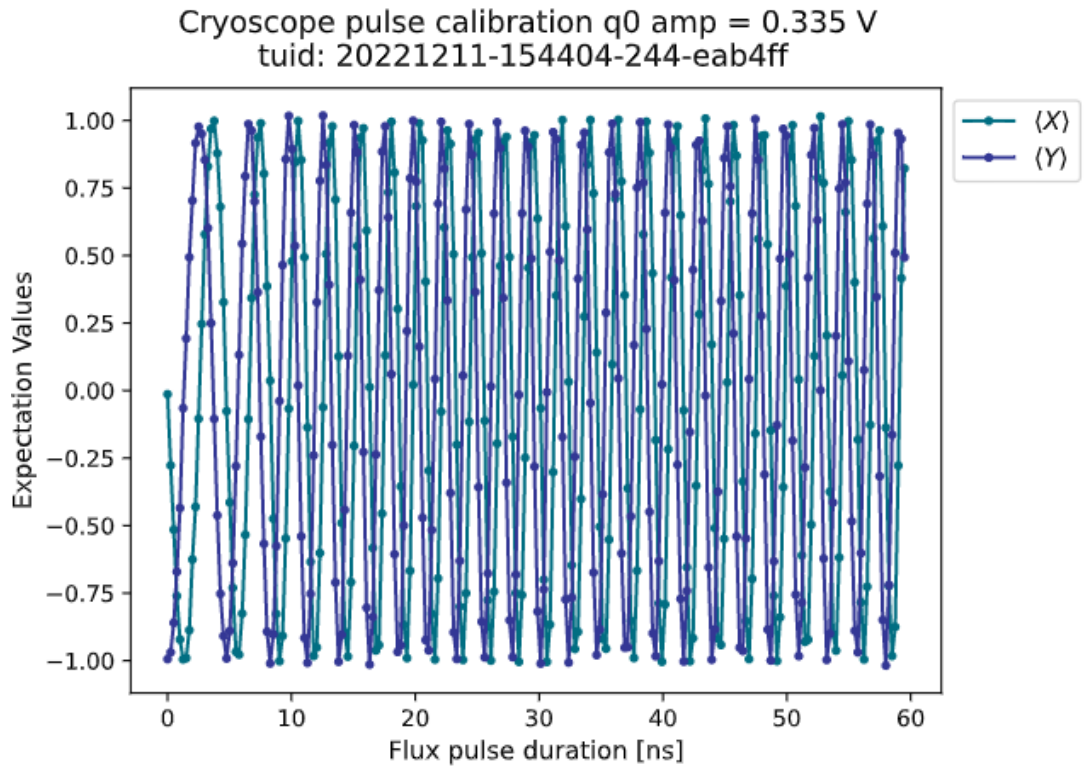

Figure 3.11: Graphical representation of the Expectation values obtained from simulated data for a pulse of 0.335 V

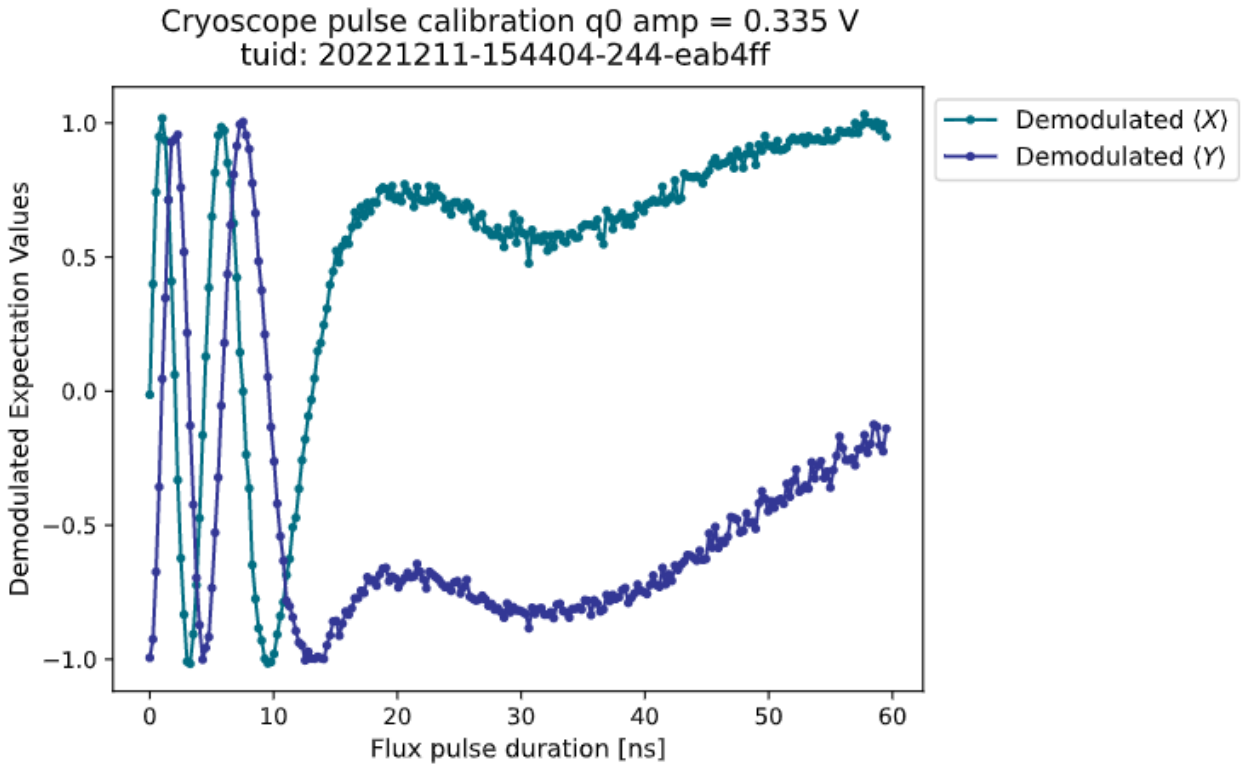

Figure 3.12: Graphical representation of the Demodulated Expectation values obtained from simulated data for a pulse of 0.335 V

lating expectation values increased. And so, after demodulating, the frequency of the oscillations is lower, as shown in Figure 3.12. After determining the expectation values, the next step is to calculate the phase ac-

quired by the qubit for the duration of the applied square pulse.

3.3.2. Calculation of the Phase acquired by the qubit

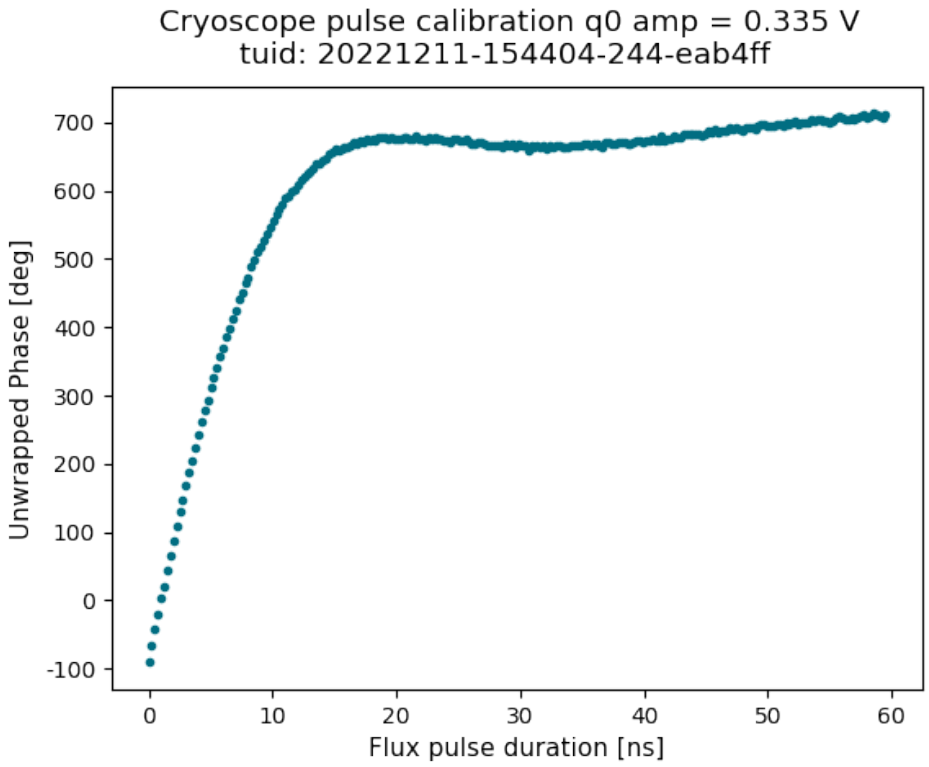

Figure 3.13: Phase acquired by qubit from simulated data

Using the evaluated expectation values, the next step of computing the phase acquired by the qubit was finding the angle between these expectation values $< Y >$ and $< X >$. So, the phase acquired by the qubit is computed as

$$\phi = \tan^{-1}(\frac{< Y >}{< X >})$$

Figure 3.13 shows the phase acquired by the qubit over varying pulse duration (x-axis) with constant pulse amplitude (0.335V). As expected, there is a rise in phase for the flux durations increase. This is because the phase of the qubit state vector is affected by both the pulse amplitude and duration.

3.3.3. Calculation of the detuning frequency

On computing the phase acquired by the qubit (ϕ) over the time duration of the pulse, the detuning frequency is calculated by differentiating the phase with respect to time as explained in Section 3.1. The detuning frequency is

$$\Delta f_{Q,detuning} = \frac{1}{2\pi} * \frac{d\phi}{d\tau} \tag{3.5}$$

Figure 3.14 shows the computed detuning frequency from the phase using the simulated data. As expected, there is a decline in values initially before the detuning frequency settles to a value. This is observed since the detuning frequency is the differentiation of the phase.

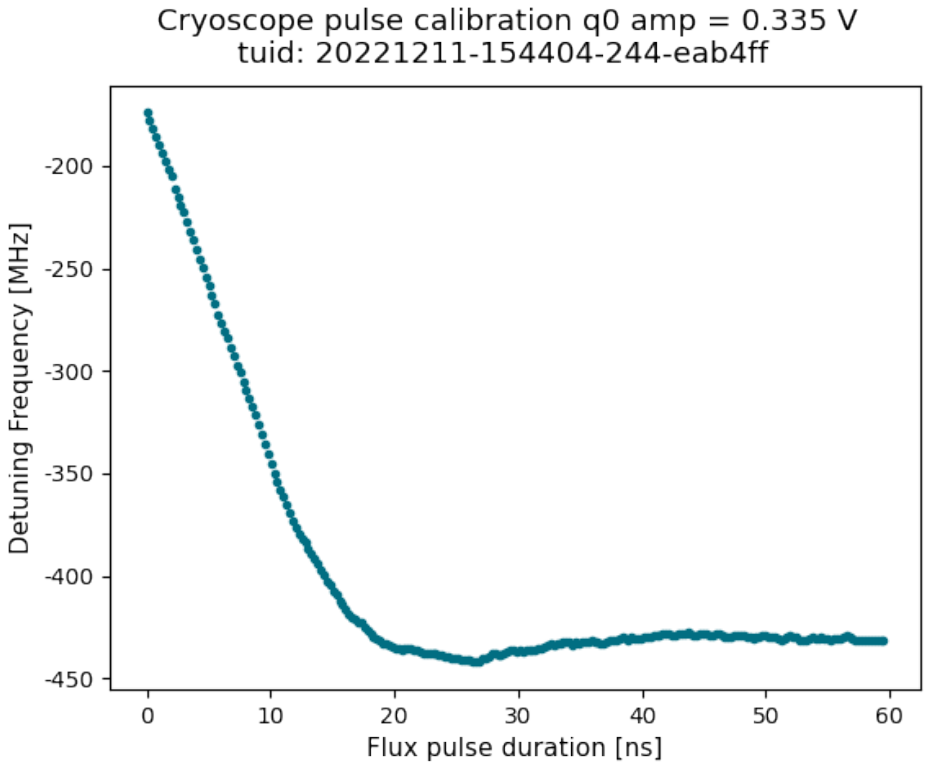

Figure 3.14: Detuning frequency of qubit from simulated data

3.3.4. Reconstruction of the flux amplitude

To calculate the pulse amplitude from the detuning frequency equation 3.4 is used. Therefore, the relation between the detuning frequency and applied flux is

$$\Delta f_{Q,detuning}(\tau) = \frac{(\sqrt{8 * E_J * E_C})}{h} * \left(1 - \sqrt{\left|\cos\left(\pi * (\frac{\Phi_Q(\tau)}{\Phi_0})\right)\right|}\right)$$

Taking into account the system-dependent constants, the above equation can be rewritten as

$$\Delta f'_{Q,detuning} = 1 - \sqrt{\left|\cos\left(\Phi'_Q(\tau)\right)\right|} \tag{3.6}$$

where

$$\Delta f'_{Q,detuning} = (\Delta f_{Q,detuning}) / \frac{(\sqrt{8 * E_J * E_C})}{h}$$
$$\Phi'_Q(\tau) = \pi * (\frac{\Phi_Q(\tau)}{\Phi_0})$$

Equation 3.6 can be further simplified by expanding the $\sqrt{\left|\cos\left(\Phi'_Q(\tau)\right)\right|}$ using the Maclaurin series. On expanding and disregarding higher powers of $\Phi'_Q(\tau)$, we get $\sqrt{\left|\cos\left(\Phi'_Q(\tau)\right)\right|} = 1 - \frac{(\Phi'_Q(\tau))^2}{4}$.

On rewriting equation 3.6 to include the above approximation, the detuning frequency can now be written as

$$\Delta f'_{Q,detuning} = \frac{(\Phi'_Q(\tau))^2}{4} \tag{3.7}$$

$$\Rightarrow \frac{(\Delta f_{Q,detuning})}{\frac{(\sqrt{8 * E_J * E_C})}{h}} = (\frac{\pi}{2} * \frac{\Phi_Q(\tau)}{\Phi_0})^2 \tag{3.8}$$

$$\Delta f_{Q,detuning} = \frac{(\sqrt{8 * E_J * E_C})}{h} * \frac{\pi^2}{2\Phi_0^2} * \Phi_Q^2(\tau) \tag{3.9}$$

For easier implementation, the detuning frequency values were normalized to calculate the flux amplitude. Normalizing the detuning frequency would remove all the constants in the above equation, leaving only a simple quadratic function. Therefore the final relation between detuning frequency and flux is

$$\frac{\Delta f_{Q,detuning}}{\Delta f^{max}_{Q,detuning}} = \frac{\frac{(\sqrt{8 * E_J * E_C})}{h} * \frac{\pi^2}{2\Phi_0^2} * \Phi_Q^2(\tau)}{\frac{(\sqrt{8 * E_J * E_C})}{h} * \frac{\pi^2}{2\Phi_0^2} * (\Phi_Q^{max}(\tau))^2}$$

$$\frac{\Delta f_{Q,detuning}}{\Delta f^{max}_{Q,detuning}} = \frac{\Phi_Q^2(\tau)}{(\Phi_Q^{max}(\tau))^2}$$

Therefore, the reduced relation finally becomes

$$\Delta f'_{Q,detuning} = (\Phi'_Q(\tau))^2 \tag{3.10}$$

where $\Delta f'_{Q,detuning}$ and $\Phi'_Q(\tau)$ represent the normalized values of detuning frequency and flux amplitude, respectively.
Using equation 3.10, the square root of the normalized detuning frequency values obtained from the experiment gives the normalized flux amplitude. This way, the flux amplitude, as seen by the qubit, is reconstructed.

Figure 3.15 shows the reconstruction of the normalized flux amplitude using the simulated data. It can be observed that the shape of the pulse faces distortions before settling to 1.

3.3.5. Calculation of correction coefficients

With the reconstructed normalized flux amplitude, the distortions in the reconstructed pulse can be observed in Figure 3.15. The principle used to correct these distortions is to design a Finite Impulse Response filter function that takes in the distorted reconstruction and gives as output the undistorted pulse. To apply this filter function, the pertinent FIR filter coefficients need to be determined. This is done using the least squares optimization method to minimize the differences between the distorted and ideal pulse (refer to section A.1 in the Appendix for details).
After computing the required (a,b) values of the FIR filter function, the correction is applied to the distorted reconstruction. Figure 3.16 shows the reconstructed flux amplitude after applying the correcting filter. It is observed that the corrected amplitude is close to 1, as expected. The final step is to re-run the Cryoscope implementation on the schedule after pre-distorting the input flux pulse.

Pre-distorted flux pulse

The qubit control system is assumed to be a linear time-invariant system; therefore, the system response, including non-idealities, can be defined using its impulse response $h(t)$ [43]. Hence, the noisy reconstruction of the flux pulse can be written as

$$\Phi_{noisy}(t) = h(\tau) \circledast \Phi_Q(t)$$

Now considering an inverse of the system response $h^{-1}(t)$, with some initial parameters, the residue $\Phi_Q(t) - h^{-1}(t) \circledast \Phi_{noisy}(t)$ is optimized until it becomes zero. At this point, the parameters for $h^{-1}(t)$ are such that $h^{-1}(t) \circledast h(t)$ is the identity.

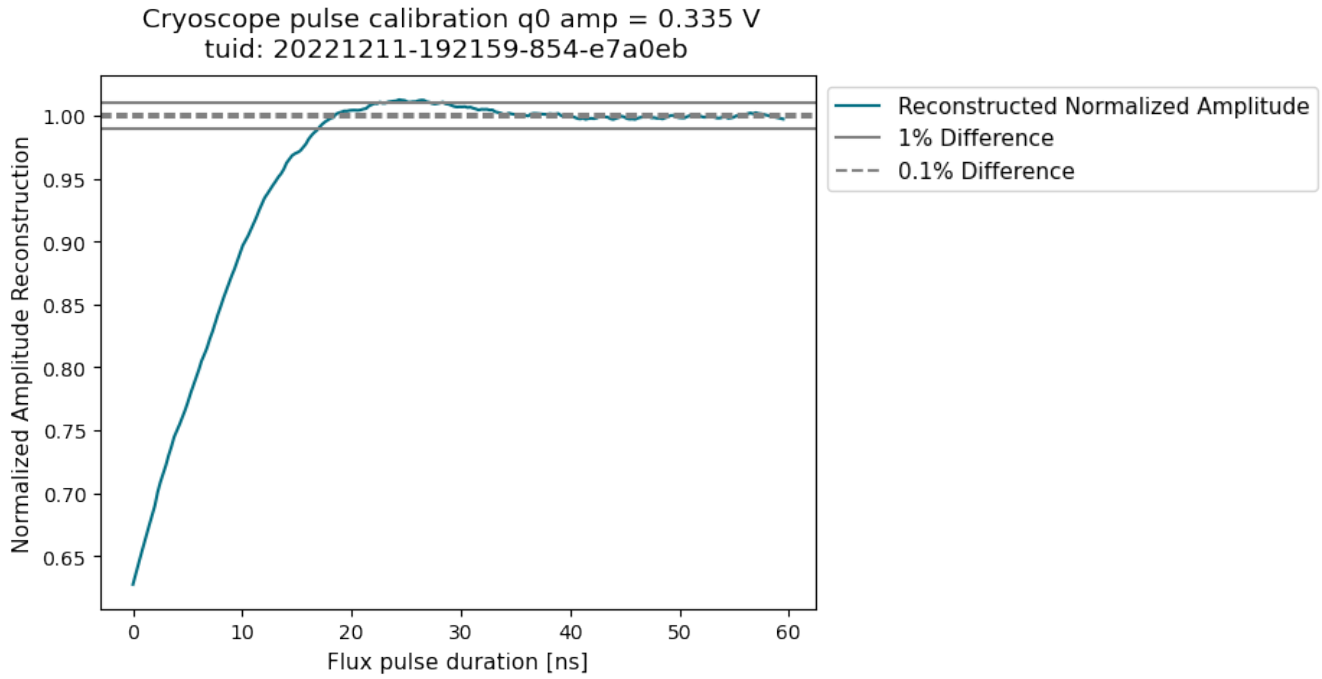

Figure 3.15: Reconstruction of Normalized flux amplitude from simulated data

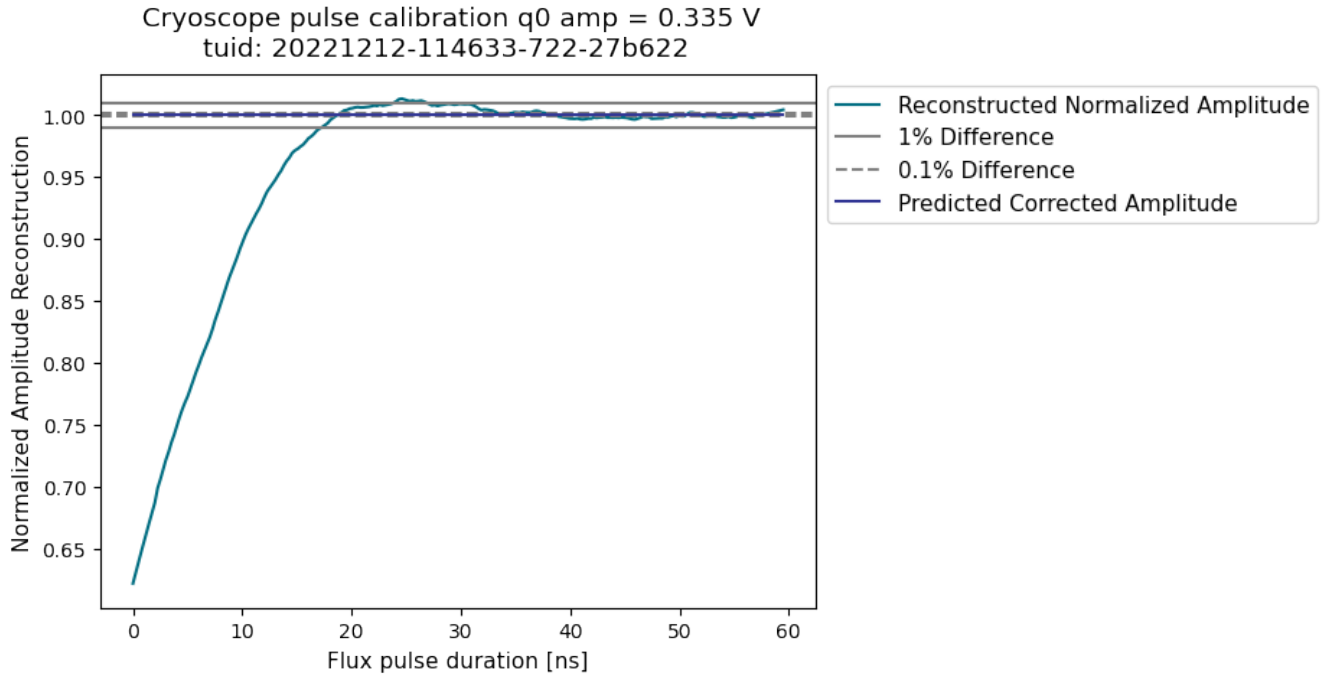

Figure 3.16: Reconstructed flux amplitude and corrected flux amplitude from simulated data

With the inverse identified as explained above, to correct for the distortions, the input signal is **pre-distorted** using $h^{-1}(t)$. The input flux pulse to the experiment now becomes $\Phi_Q'(t) = h^{-1}(t) \circledast \Phi_Q(t)$. As this pre-

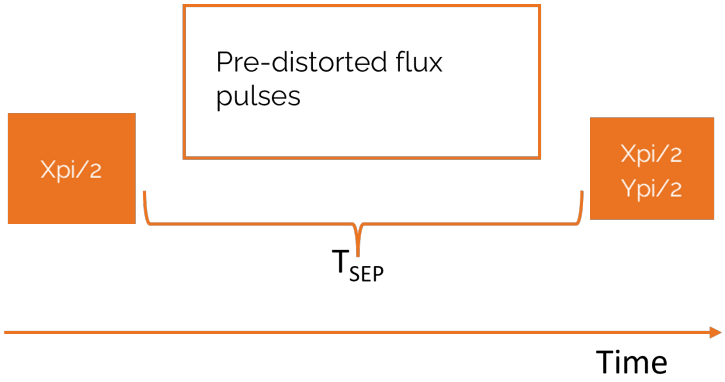

Figure 3.17: Block Diagram representing the Cryoscope implementation with pre-distorted flux pulses

distorted signal traverses the noisy control line $\Phi_{reconstructed}(t)$ now becomes

$$\begin{aligned}\Phi_{reconstructed}(t) &= h(t) \circledast \Phi_Q^{'}(t) \\ &= h(t) \circledast h^{-1}(t) \circledast \Phi_Q(t) \\ &= \Phi_Q(t)\end{aligned}$$

This way, the noise along the control line is compensated for using the pre-distorted input signal. This has been shown in Figure 3.17.

Applying pre-distortions - Calibration

On re-running the experiment with the pre-distorted flux pulse, with the internal noise being compensated by the pre-distorted pulse, the reconstruction should be close to the ideal flux pulse shape. By rerunning the

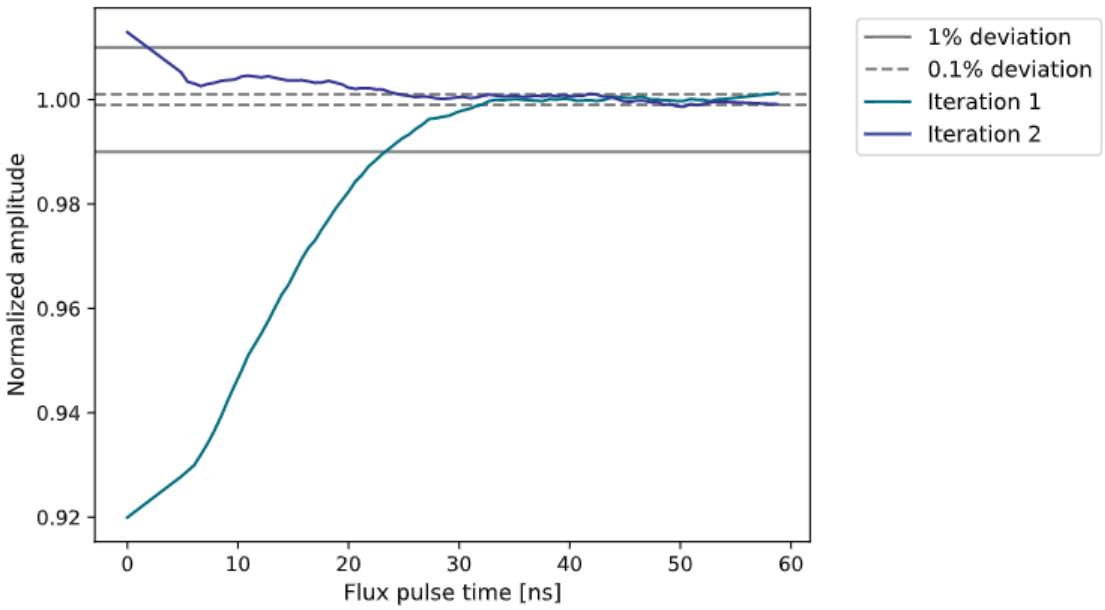

Figure 3.18: Flux amplitude reconstruction after pre-distortion

experiment using the simulation function, it can be seen from Figure 3.18 that the second iteration of the Cryoscope experiment returns almost the ideal square pulse in the reconstruction.
After verifying the working of the Analysis implementation, actual experimental data was put through the same.

3.4. Experimental results

This section shows the results obtained from the actual experimental data with the Analysis code that was verified using the simulated data. The experiment was run with a square pulse amplitude of 0.22V for varying pulse duration between 0 ns and 100 ns.

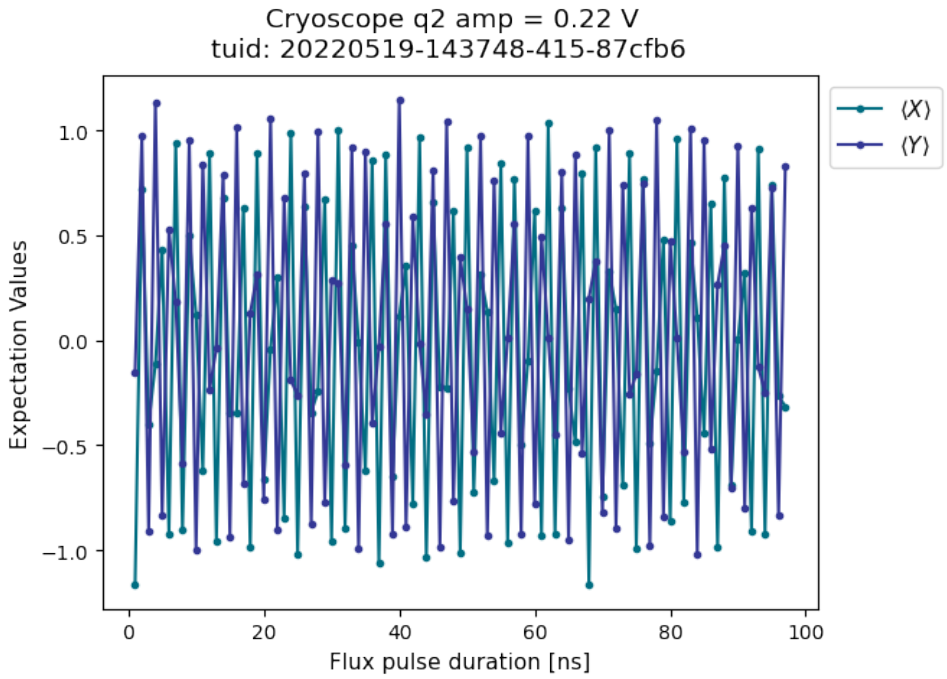

Figure 3.19: Expectation Values

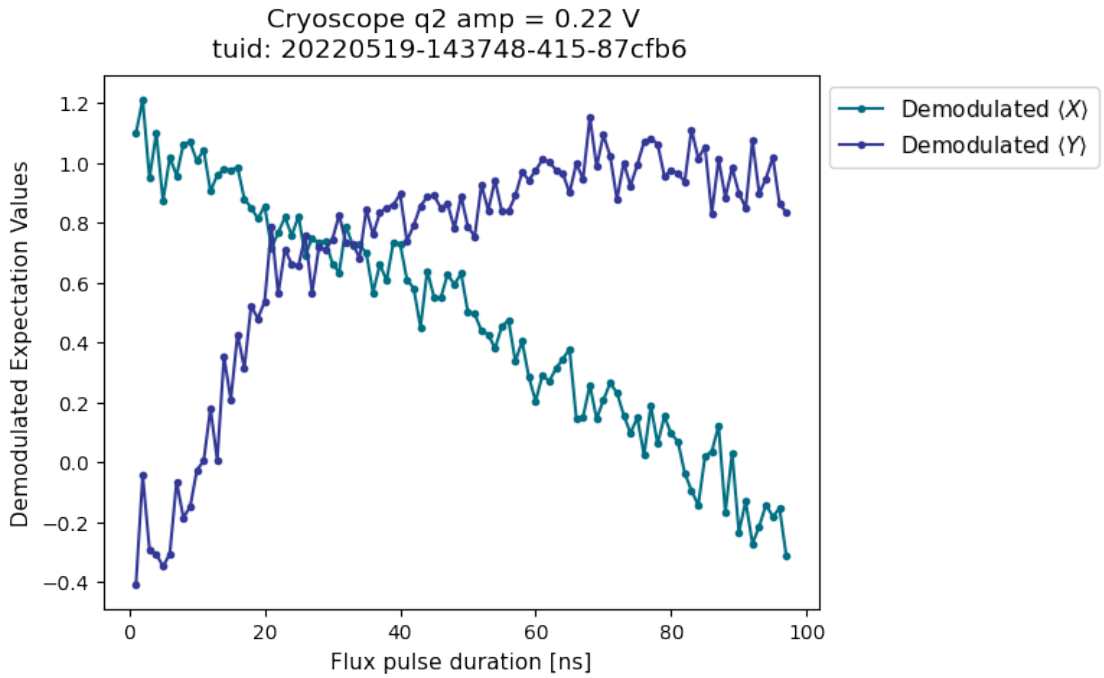

Figure 3.20: Demodulated Expectation Values

Figures 3.19 and 3.20 show the expectation values computed from the experimental raw data.
Figure 3.21 shows the <X> and <Y> values against each other. This graph is used to verify if the calculated

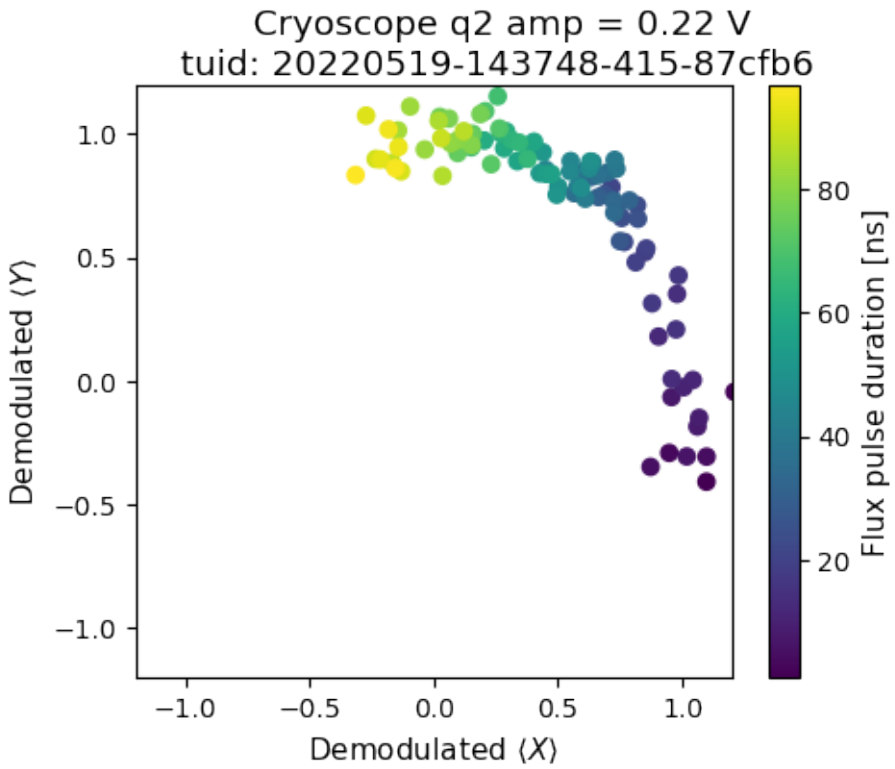

Figure 3.21: Equatorial Projection

expectation values lie on the unit circle. This graph also serves as a pictorial representation of the qubit phase progression.

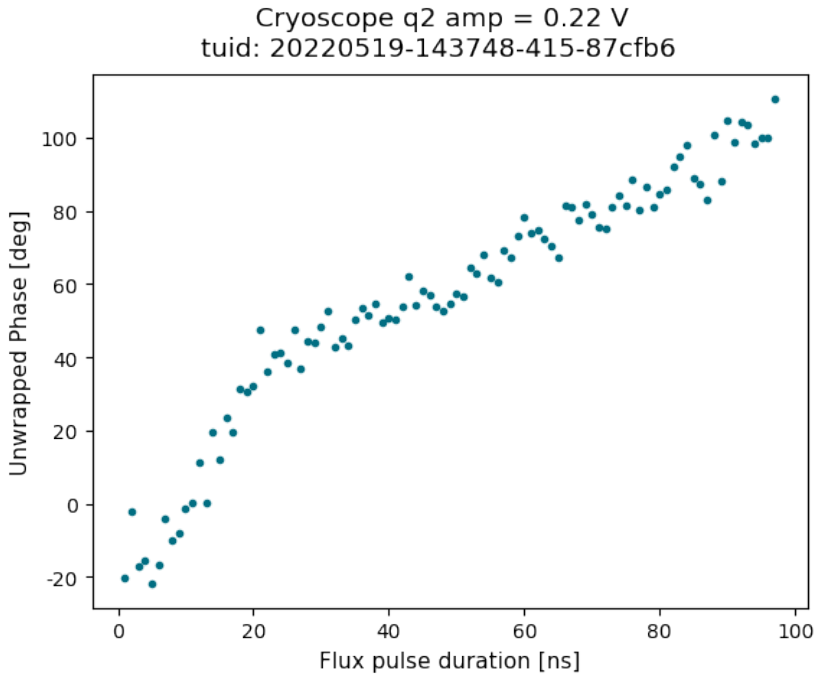

Figure 3.22: Phase acquired by qubit from experimental data

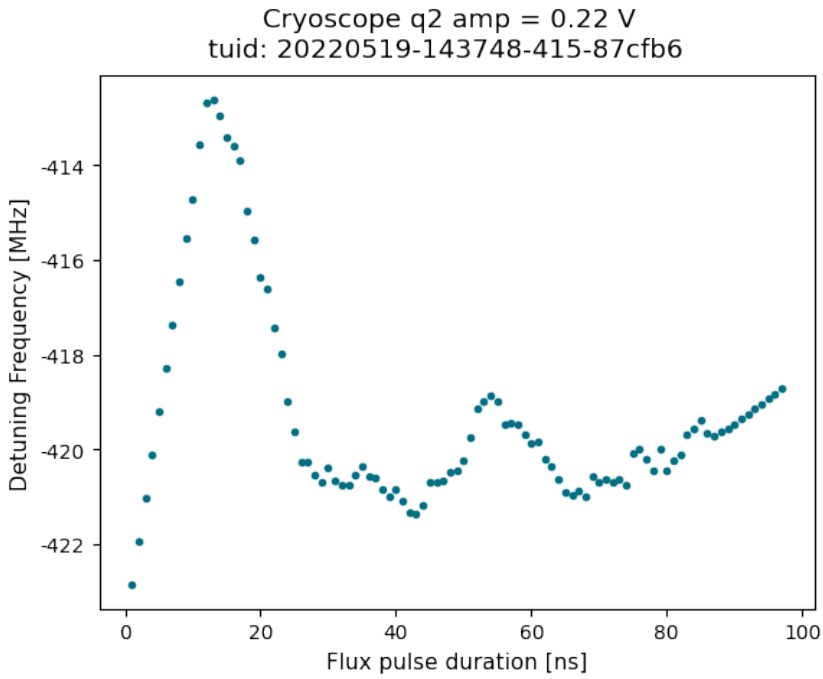

Figure 3.23: Detuning frequency

Figures 3.22 and 3.23 display the phase acquired by the qubit over the varying pulse duration and the related detuning frequency at 0.22V.

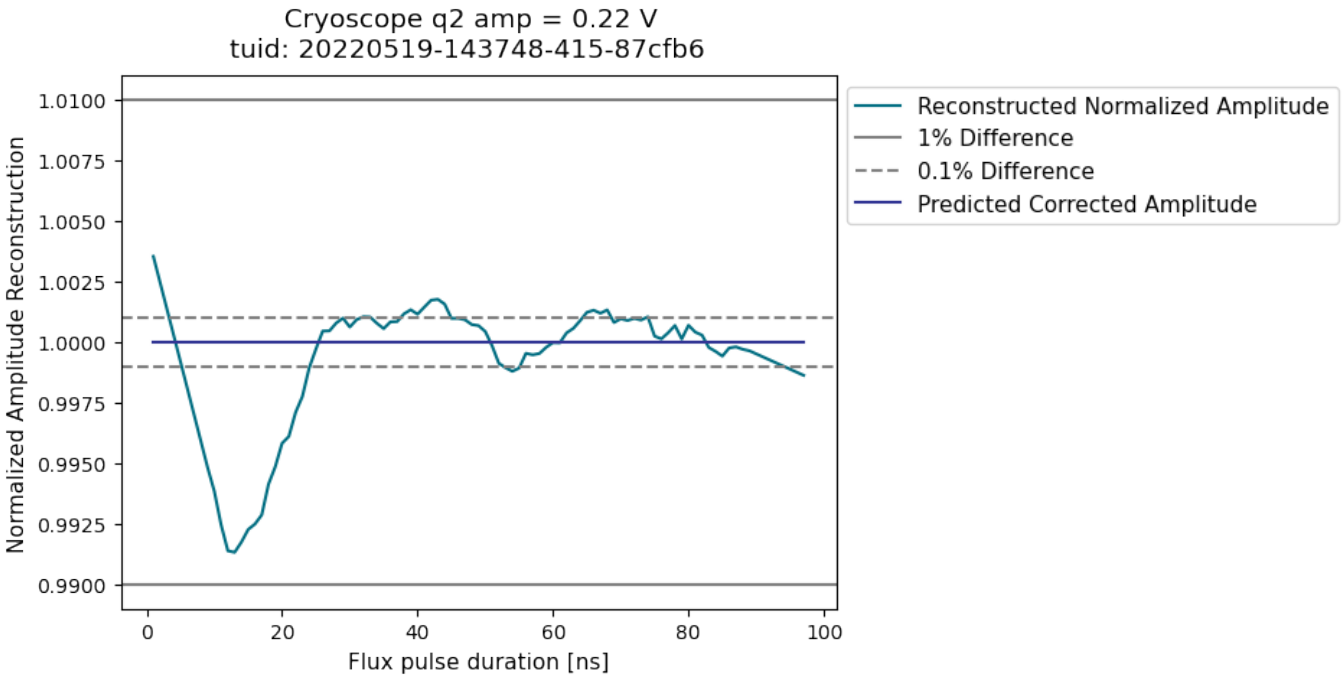

Figure 3.24: Reconstruction of Normalized Flux amplitude as seen by the measured qubit

Using the detuning frequency values, the pulse, as seen by the qubit, is reconstructed. The normalized reconstruction of the pulse has been shown in Figure 3.24. With the use of this reconstruction and the ideal pulse (entered as an array of 1s for [0ns, 100ns]), the correction coefficients (pre-distortion parameters) are

calculated. These parameters are used to pre-distort the flux pulse, which is then used in the next run of the Cryoscope experiment to rectify the distortions. The second run of the experiment has not been shown here.

3.5. Assumptions and Drawbacks of method

The Cryoscope method is applicable in systems where the qubit frequency is related to the control variable (in transmons, the input flux pulse) quadratically or with higher powers. And it is also assumed that the initial qubit frequency is at the 'sweet spot', where the qubit frequency is the least sensitive to first-order flux variations [28]. With this assumption, the implementation ignores noise that causes the qubit frequency to be related to first-order variations of the flux. Therefore, this method is not optimal for the correction of distortions due to system noise in quantum systems where the qubit frequency has a linear dependence on the control variable. The importance of qubit frequency dependence on the control variable to be of second order or higher is explained in detail in the supplement section of [41].
The method also assumes that the dephasing caused by the turn-off transients of the pulse is negligible. Using equation 3.5, detuning frequency can be written as

$$\Delta f_{Q,detuning} = \frac{1}{2\pi} * \frac{d\phi}{d\tau}$$

Therefore, the following can be derived from the above

$$\phi = 2\pi * \int_{\tau=0}^{T_{SEP}} \Delta f_{Q,detuning} d\tau$$
$$\phi = 2\pi * \int_{\tau=0}^{t_{off}} \Delta f_{Q,detuning} d\tau + 2\pi * \int_{\tau=t_{off}}^{T_{SEP}} \Delta f_{Q,detuning} d\tau$$

where T_{SEP} is the total time between the $\pi/2$ rotations. All effects that cause the qubit to detune are taken to occur within this time interval. While t_{off} specifies the time at which the pulse is switched OFF, computed from the user-defined input of pulse widths. After the pulse is turned OFF, ideally, the qubit would return to its original configuration without any flux. In practicality, however, there might still be some effects of the turn-off transients that might lead to the qubit to dephase. This dephasing caused in the OFF part of the pulse, in the equation above as $2\pi * \int_{\tau=t_{off}}^{T_{SEP}} \Delta f_{Q,detuning} d\tau$ is taken to be small enough not to give rise to a large contribution to the dephasing. Thus, it is disregarded in the Cryoscope experiment [28]. With this assumption, only the distortions on the rising edge of the pulse are accounted for by reconstructing only this part of the pulse.
Linear systems characteristics are completely specified by the system's impulse response [43]. By taking the qubit control system as a linear time-invariant system, system noise has been easily characterized using the impulse response $h(t)$. Therefore, the entire experiment hinges on the assumption that the qubit control system is linear and time-invariant.
In conclusion, the Cryoscope is a novel approach to correcting for the distortions on the control line of a qubit system by using the qubit itself for the noise characterization. It has been shown that the method is workable for single qubit distortion characterization in two-level transmon systems.

4

Ramsey using Kelly's method

Superconducting qubits are limited in their usage because of their short dephasing times. Dephasing, as mentioned in Section 2.3, can be caused by fluctuations in the qubit when transiting from state $|0\rangle$ to $|1\rangle$. In order to negate the low dephasing times caused due to flux noise, individual transmons are pulsed at the 'sweet spot' frequency, i.e., the frequency at which the state occurs without being sensitive to frequency fluctuation of the first order [36].
Flux effects on the transmon can also cause dephasing. This dephasing results from the qubit frequency detuning from the drive frequency. From Equation 3.10, it is seen that the change in qubit frequency is quadratically related to the input flux. To curb this dephasing, the method taken from the thesis work of Dr. Kelly suggests using the qubit state measurements to extract the affected parameter. This method is a predecessor to the Cryoscope distortion-characterization method, with the methodology being similar to that of the Cryoscope. In the following sections, the implementation of the idea on page 93 of the thesis work [44] is explained.

4.1. Principle

The transition frequency of the qubit is varied by the application of magnetic fluxes of specific amplitude. The flux is applied as a square pulse to the qubit. The noise along the flux line appears as distortions on the square pulse. In the absence of noise, the square pulse at the qubit would resemble Figure 4.1a. Without any

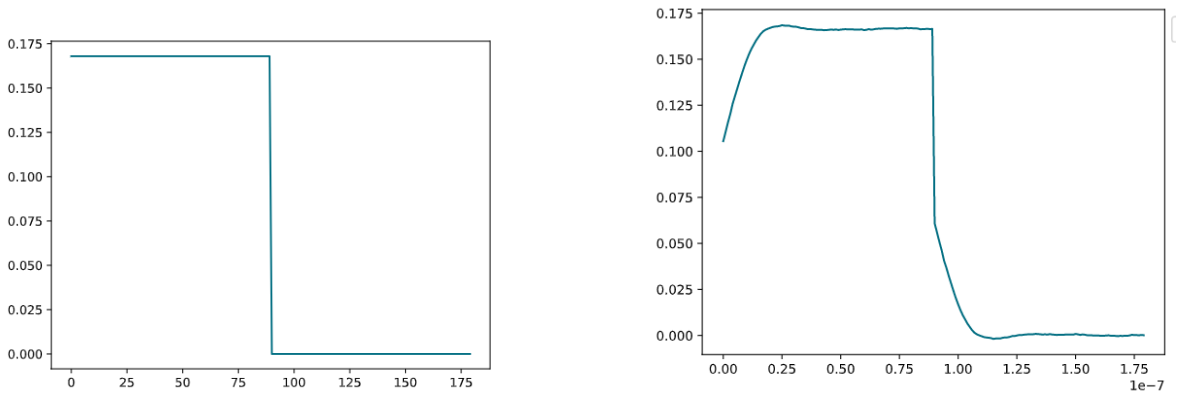

(a) Ideal square pulse that is expected at the qubit

(b) Distorted square pulse caused by noise

Figure 4.1: Square pulse renditions

distortions on the pulse, the transition frequency is dependent on the applied flux as shown in the equation 3.10. However, when the flux bias line is affected by noise, the square pulse becomes distorted, as shown in Figure 4.1b. This distorted square pulse, when applied to the qubit, would cause the qubit to dephase. Therefore the idea implemented in [44] is to apply a square pulse affected by noise to the transmon qubit and identify the distortions by analysing the qubit state measurements.

We assume that the flux line is a linear time-invariant system (similar to Section **??**). With this assumption, the noise on magnetic flux applied is quantified as an impulse response convolved with the square pulse.

$$\Phi_{ideal}(t) \circledast h(t) = \Phi_{distorted}(t)$$

where $\Phi_{ideal}(t)$ is the ideal square pulse (Figure 4.1a) and $\Phi_{distorted}(t)$ is the distorted square pulse (Figure 4.1b). Assuming that the pulse is turned off is at time $t = t_{off}$, $\Phi_{ideal}(t)$ can be split into the on-pulse and off-pulse.

$$[\Phi_{ideal}(t)]_{t=0}^{t=t_{off}} \circledast h(t) + [\Phi_{ideal}(t)]_{t=t_{off}}^{t=\tau} \circledast h(t) = \Phi_{distorted}(t)$$

The implementation extracts the distortion parameters ($h(t)$) by considering only the off-pulse part of the pulse.

4.2. Implementation

The above method is implemented by first applying a square pulse. After the square pulse is switched off, a Ramsey experiment is done.

Figure 4.2 shows the implementation of this method. With the initial application of the square pulse, the

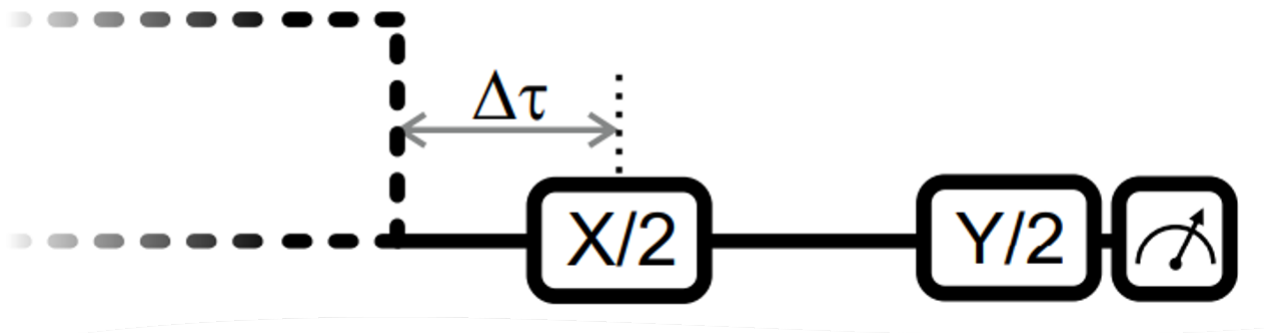

Figure 4.2: Block diagram depicting the method [44]

qubit is detuned from its original transition frequency. Once the pulse is removed, ideally, the qubit frequency should return to its initial value. In the presence of noise, however, the remnants of the falling edge of the pulse induce qubit dephasing. Therefore, this dephasing is captured by rotating the qubit to the equatorial plane by the initial $X_{pi/2}$ rotation and then a final $\pi/2$ rotation around the x-axis or the y-axis. By varying the wait times Δt, between the time at which the pulse was switched OFF (found using the fixed value of $pulse\_width$) and the first $\frac{\pi}{2}$ rotation, the dephasing caused by the distorted flux is effectively calculated. The Schedule to implement this method on the setup is very similar to the Cryoscope experiment explained in section 3.2.

Listing 4.1: Code snippet showing Kelly's method in the Schedule

```
sched = Schedule("Ramsey using Kelly")

sched.add(Reset(q0))  # initialize the qubits
square_pulse = sched.add(
    SquarePulse(amp=0.2, duration=1e-6, port="q0:res", clock="q0.ro")
) # adding square pulse

initial_X90 = sched.add(
            X90(qubit),
            rel_time=tau,
            ref_op=square_pulse,
        ) # to rotate the qubit to the equatorial plane after time 'tau' from the
            square\_pulse
```

```
13
14 sched.add_resource(readout_clock)
15 sched.add(Y90(qubit=q0), rel_time = 1e-9, ref_op=initial_X90) # final Y rotation
16                         # also implemented with the final X90 rotation
17 sched.add(Measure(q0, acq_index=0)) # measurement
18 sched
```

The code snippet 4.1 shows the code implementation of the experiment. The relative time tau between the application of the square pulse and the initial $X_{pi/2}$ rotation is varied to accommodate for the wait times (Δt). The pulse duration is kept constant throughout the experiment. The time between the two rotation pulses is also kept constant as shown in the code 4.1. This is implemented by specifying the rel_time from the reference point $ref\_op = initial\_X90$ with a constant. Similar to the Cryoscope experiment, the only difference here is the placement of the square pulse, which is implemented before rotating the qubit to the equatorial plane. The data from the qubit state measurements is then analysed to reconstruct the distorted fall edge of the pulse.

4.2.1. Simulation Implementation

To check the working of the analysis code, a function that gives the experiment's simulated data was coded. The simulated data is calculated by first computing the phase caused by the flux's presence.
From the 'Schedule', the user input of wait times, flux pulse amplitude, the values of the constant pulse duration ($pulse\_width$) and the time between the rotation pulses are taken (t_{sep}). With the input amplitude being in Volts, a mock value of qubit flux sensitivity is used to convert the input amplitude into the flux amplitude (amp) at the qubit. Using an inbuilt Heaviside function and the converted amplitude, a square pulse that is ON for the input $pulse\_width$ and OFF after the input t_{off} for an interval of t_{sep}, is computed. Figure 4.1a shows an example of the ideal square pulse for a $pulse\_width$ of $90ns$ and the t_{sep} at $90ns$.
The next step is to add known distortion parameters to this ideal square pulse to emulate the noise that will arise in the actual system. The ideal square pulse is distorted using an FIR filter function with known filter coefficients b. In the current simulated data for this method, the distortion filter parameters used are the ones obtained from the experimental data of a Cryoscope experiment. Using these distortion parameters with the FIR filter on the ideal square pulse, the distorted square pulse is acquired, shown in Figure 4.1b.
The next step was to compute the simulated detuning frequency values that were caused by the distorted square pulse using the relation 3.4. Mock values of E_J and E_C together with the known value of the flux quantum Φ_0 were used to compute the detuning frequencies for every value of the flux amplitude ($\Phi_Q(t)$ in the relation).
The detuning frequency values computed during the OFF period of the pulse are spliced out since the method requires dephasing after the pulse has been switched off. That is, in the given example of $pulse\_width = 90ns$ and $t\_sep = 90ns$, with the resolution of $1ns$, the square pulse would have 180 values. Therefore, the detuning frequencies computed also have 180 values. When splicing using t_sep, the detuning frequencies would be whittled down to 90 values since the method requires dephasing to be calculated in the absence of the flux pulse.
After the necessary detuning values are obtained, the respective phase values are calculated by integrating over the detuning frequencies. From equation 3.5, it is known that

$$\Delta f_{Q,detuning} = \frac{1}{2\pi} * \frac{d\phi}{dt}$$

Therefore, the phase is

$$2\pi * \int \Delta f_{Q,detuning} dt = \phi$$

In the absence of any distortions, there is no flux pulse applied on the qubit and so, there is no phase acquired by the qubit. When conducting the Ramsey experiment under this condition, the expectation values are simply -1 for the final X90 rotation ($< Y >$) and 0 for the final Y90 rotation ($< X >$). This is because, in an ideal situation, the qubit state vector after being rotated by 90° around the X-axis from the initial $|0\rangle$ state, remains in the $|-i\rangle$ state until the final rotation. When the final rotation is a 90° around the X-axis, the state becomes $|1\rangle$ whose expectation value is -1. When the final rotation is a 90° around the Y-axis, the state remains at $|-i\rangle$ whose expectation value is 0. Therefore, in an ideal situation, the expectation values at the output would be simply just -1 and 0 as shown in Figure 4.3.
In this case, there is no phase acquired by the qubit which is shown by the rendition of the equatorial projec-

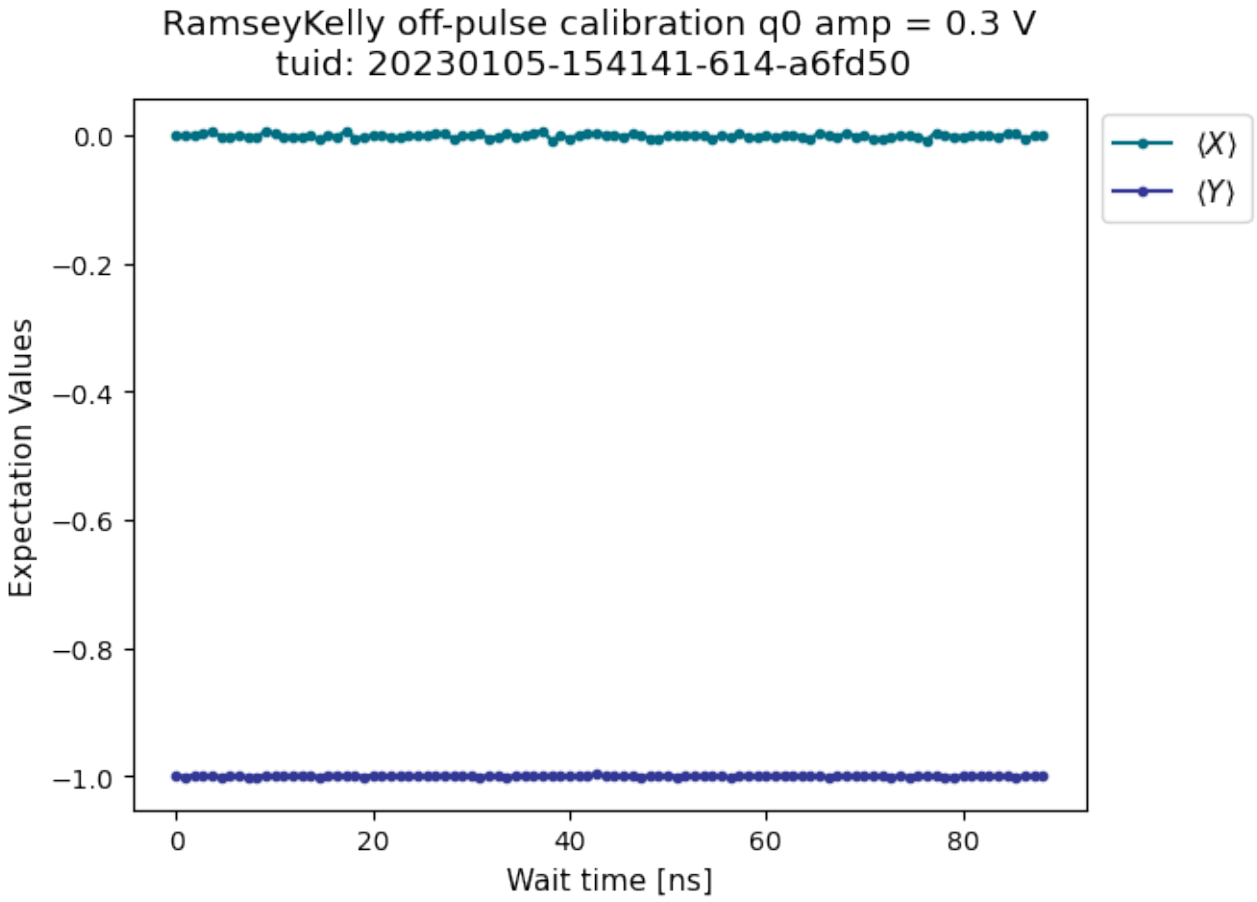

Figure 4.3: Ideal Expectation Values of Kelly's Ramsey experiment

tion in Figure 4.4.
To add the effect of the distortions, the calculated dephasing values are added to the expectation values using cosine functions as explained in Section 3.3.2. After the expectation values are calculated, the corresponding state probability values are computed as

$$\text{prob}(|\Psi\rangle) = \frac{1 - \text{expectation values}}{2}$$

Thus calculated state probability values are then used to gauge approximate resonator output values which is done using an inbuilt resonator function. The simulated data was used in running the analysis section of the code since this experiment was not implemented on the setup as yet. The following analysis section receives the data from the setup, or in this case, the simulation function and computes the distortion parameters.

4.3. Analysis

The analysis of this method follows the same flow described in Figure 3.9. From the I-Q values received, expectation values are calculated by rotating the data using the calibration points as explained in section **??**. From the expectation values, the phase acquired by the qubit is obtained by evaluating the phase between the expectation values $< Y >$ and $< X >$. Then the detuning frequency values are calculated in a similar fashion to the Cryoscope analysis by differentiating the phase. Using the same logic explained in the Cryoscope analysis, the normalized amplitude reconstruction is done using equation 3.10. From the reconstruction, the correction coefficients are determined using the least squares method. The ideal square pulse to be optimized against is set as the ideal pulse from Figure 4.1a from the time the pulse is switched off. In the given example, this would be the ideal pulse values $\forall$ wait times $\in [90e^{-9}, 180e^{-9}]$. The FIR filter coefficients are found by optimizing the residue between the above ideal square pulse values and the reconstructed amplitude values. Using the calculated correction FIR parameters, a pre-distortion filter is added to the pulse at

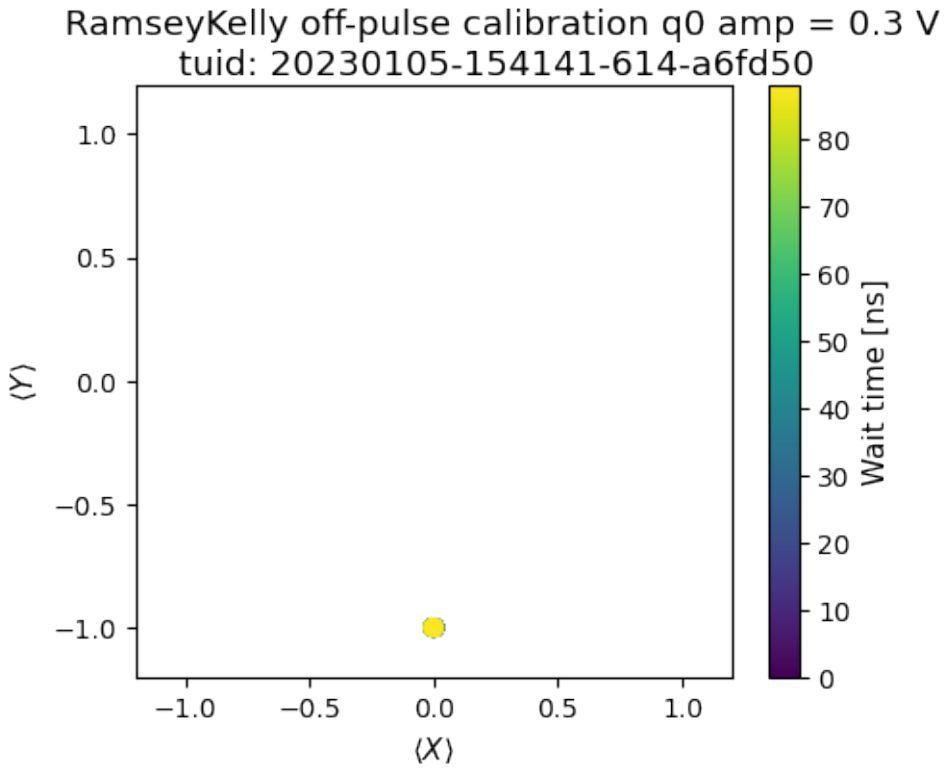

Figure 4.4: Ideal Equatorial Projection graph of Kelly's Ramsey experiment

the start of the experiment and the experiment is run again. Earlier, we saw that the distorted pulse can be written as

$$h(t) \circledast \Phi_{ideal}(t) = \Phi_{distorted}(t)$$

This relation holds the same when converted to the voltage domain since $\Phi(t) = V(t) *$ qubit flux sensitivity which is constant for a given system.
Therefore, when using a correction FIR filter, the distorted pulse reconstruction is brought back to the ideal shape. This correction filter effectively applies $h^{-1}(t)$ to the distorted pulse reconstruction cancelling out the noise quantified as $h(t)$. The application of the FIR correction filter is then

$$\begin{aligned} V_{corrected}(t) &= h^{-1}(t) \circledast V_{distorted}(t) \\ &= h^{-1}(t) \circledast h(t) \circledast V_{ideal}(t) \\ &= V_{ideal}(t) \end{aligned}$$

When the correction filter is applied to the ideal input voltage pulse at the start of the experiment, the input voltage becomes $h^{-1}(t) \circledast V_{ideal}(t)$. When this pre-distorted input voltage encounters the noisy elements ($h(t)$), the pre-distortion cancels out leaving behind the ideal pulse to be seen by the qubit. That is, on applying the pre-distortion (FIR filter with the correction coefficients),

$$V_{input} = h^{-1}(t) \circledast V_{ideal}(t)$$

On running the experiment again, the pulse actually implemented at the qubit is reconstructed again by the analysis. This reconstructed pulse then is

$$\begin{aligned} V_{reconstructed}(t) &= h(t) \circledast V_{input}(t) \\ &= h(t) \circledast h^{-1}(t) \circledast V_{ideal}(t) \\ &= V_{ideal}(t) \end{aligned}$$

In an ideal scenario, the second run of the experiment should return a perfect reconstruction of the distortion-less square pulse. In the case of using simulated data, a check here would be to compare the input distortion parameters and the correction parameters from the reconstruction to see if they're the exact inverses of each other. The following section shows the results of applying the analysis code to the simulated data of the experiment.

4.4. Results

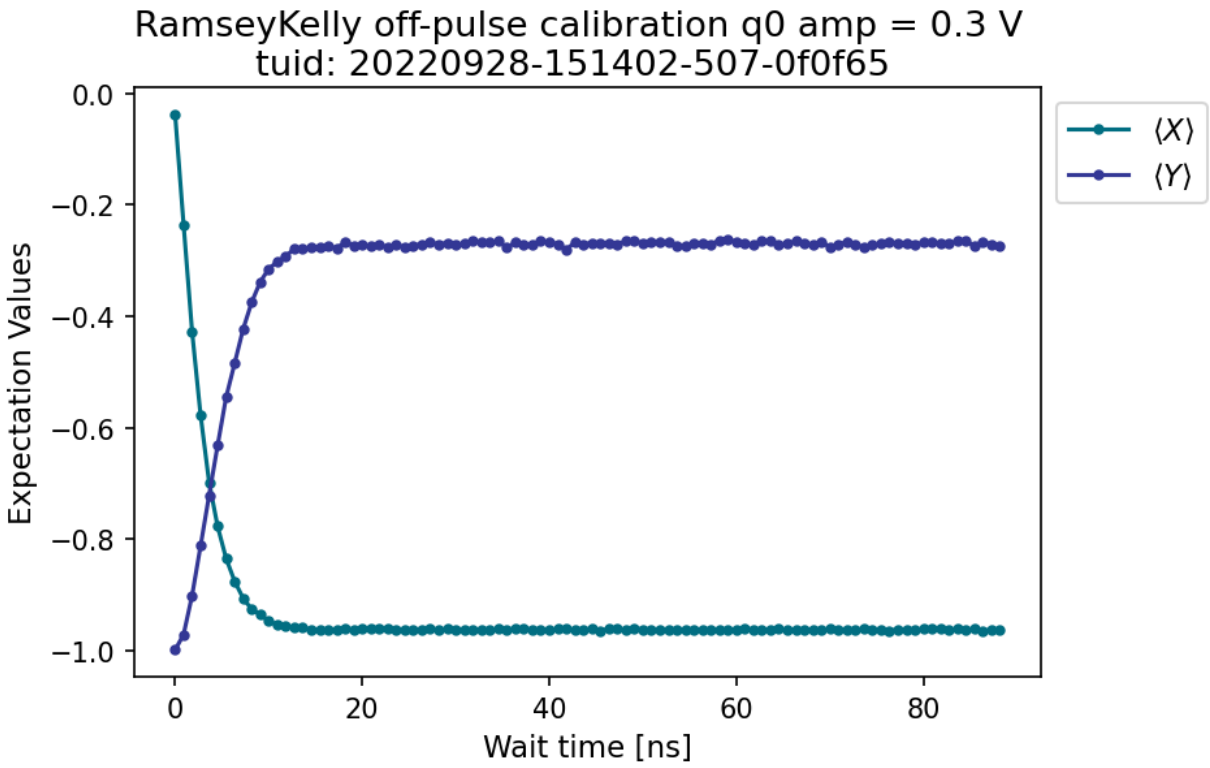

Figure 4.5: Expectation Values

Using the simulated data that contains distortions on the input pulse, the analysis code gives the output of the following graphs. In the presence of distortions, the output expectation values show initial oscillations before settling to a value as shown in Figure 4.5.

Figure 4.6 shows the phase acquired by the qubit state vector on the equatorial plane. The acquired phase stabilizes at a final value showing that the flux pulse value also drops to zero as the wait time increases. Figure 4.7 shows the phase acquired by the qubit. This is the phase that is evaluated as the phase between the expectation values $< Y >$ and $< X >$. During the OFF part of the pulse, as the distortions cease and the pulse value drops to zero, the effect of the pulse on the frequency also lessens thereby allowing the qubit to regain its transition frequency. Therefore, the detuning frequency is initially high due to the presence of flux and as the flux value slowly disappears, the detuning frequency recedes to zero which is shown in Figure 4.8.
From the detuning frequency, the amplitude is reconstructed as mentioned in section 4.3. In the Cryoscope

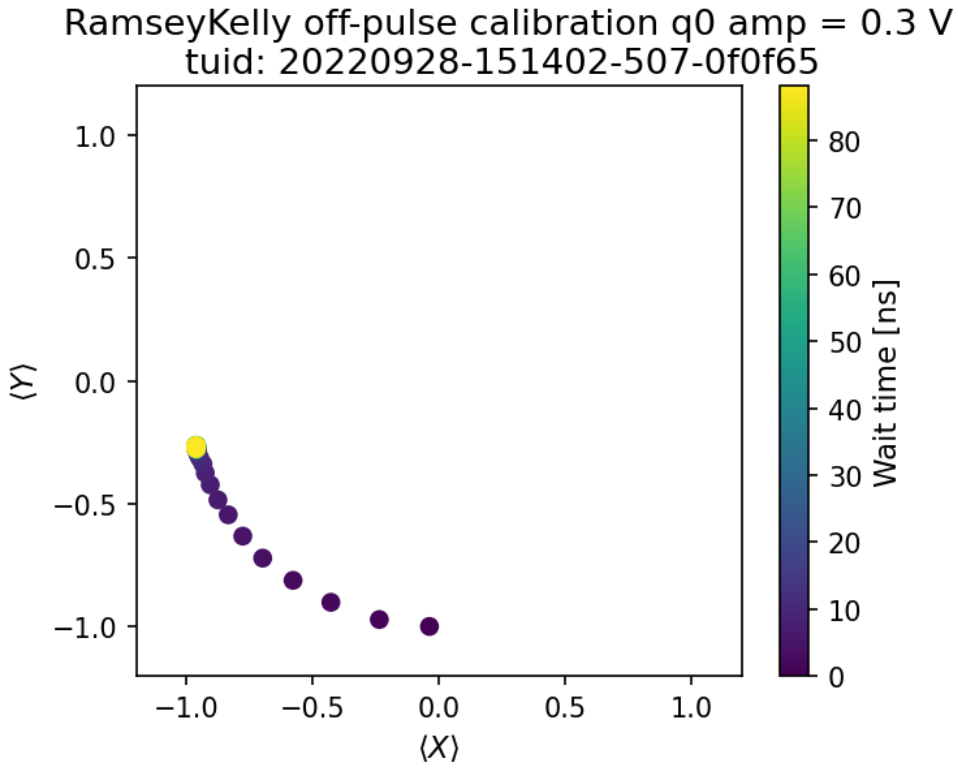

Figure 4.6: Equatorial representation of the qubit state vector rotation

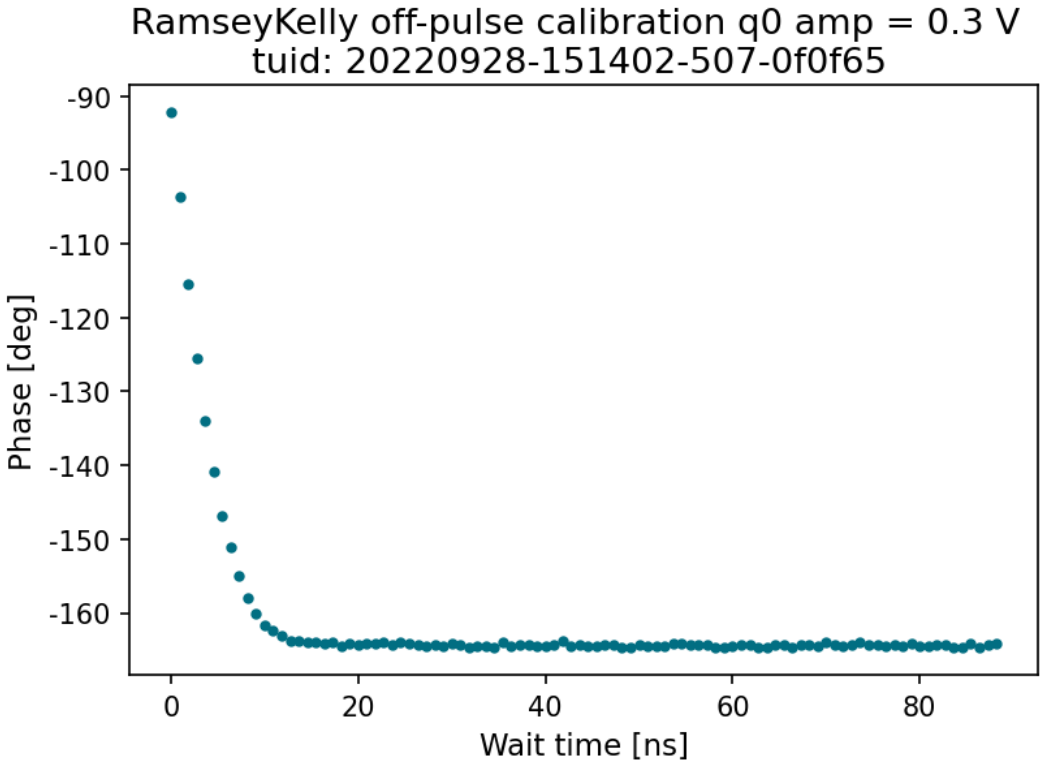

Figure 4.7: Phase acquired by the qubit against wait time

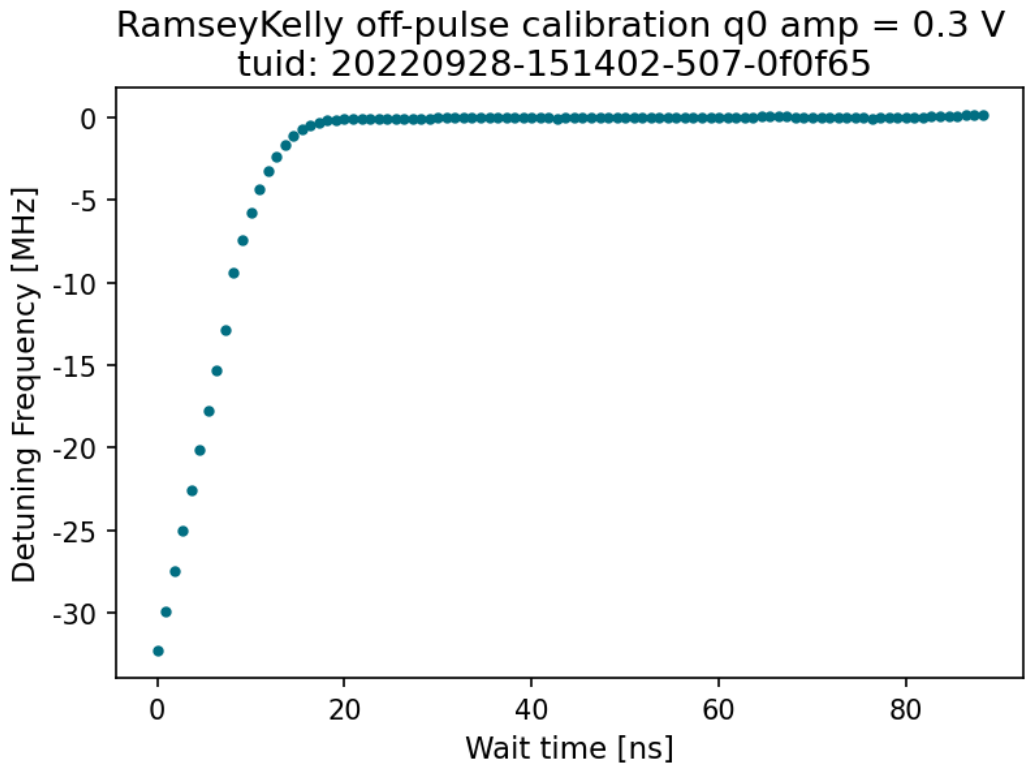

Figure 4.8: Detuning frequency against wait time

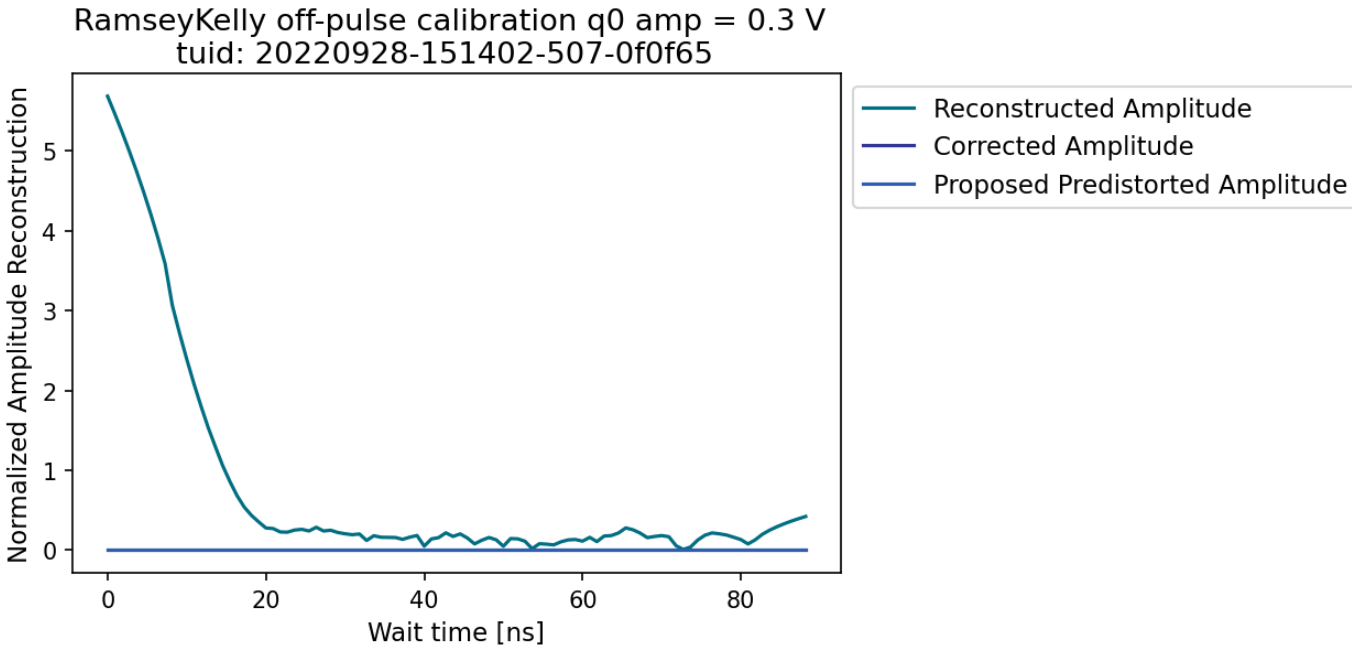

Figure 4.9: Reconstructed amplitude against wait time

experiment (refer section 3.2, the flux amplitude is related to the detuning frequency using equation 3.9 -

$$\Delta f_{Q,detuning} = \frac{(\sqrt{8 * E_J * E_C})}{h} * \frac{\pi^2}{\Phi_0^2} * \Phi_Q^2(\tau)$$

$$\frac{\Delta f_{Q,detuning}}{\frac{(\sqrt{8 * E_J * E_C})}{h} * \frac{\pi^2}{\Phi_0^2}} = \Phi_Q^2(\tau)$$

$$\Delta f'_{Q,detuning} = \Phi_Q^2(\tau)$$

$$\text{where} \quad \Delta f'_{Q,detuning} = \frac{\Delta f_{Q,detuning}}{\frac{(\sqrt{8 * E_J * E_C})}{h} * \frac{\pi^2}{\Phi_0^2}}$$

In the convolution of signals, the presence of constants only amplifies or attenuates the resulting signal without affecting the convolution itself [45]. Therefore, the effect of noise (quantified as system impulse response $h(t)$) is unaffected by the constants in the above relation. By taking the square root of this equation, the flux pulse amplitude is reconstructed as shown in Figure 4.9.
With the reconstruction completed, the correction coefficients are calculated by optimizing the reconstruction against the ideal square pulse. After obtaining the correction coefficients via this method, a pre-distortion filter is applied to the pulse at the start of the experiment and the method is implemented again. The second run of the experiment, ideally, corrects the noise in the system and reconstructs the ideal pulse. Multiple runs of the experiment are conducted in order to achieve a final reconstruction that is within a tolerable error threshold. The error here is calculated as

$$\text{Error} = \text{Ideal Square Pulse} - \text{Reconstructed Square Pulse}$$

The multiple runs of the experiment are shown in Figure 4.10. It can be seen that the amplitude reconstruc-

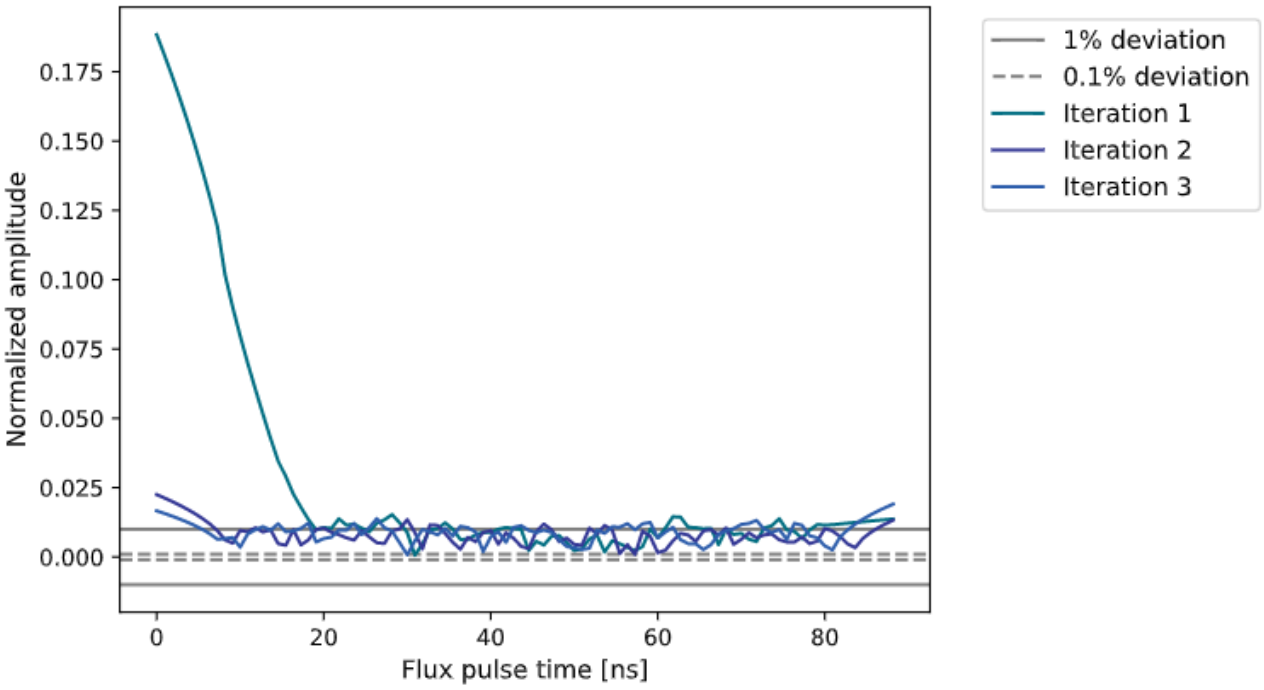

Figure 4.10: Amplitude reconstruction of multiple runs

tion becomes closer to the ideal square pulse with the introduction of pertinent pre-distortion filters, i.e., as the number of runs increases, reconstruction tends more towards the ideal pulse as expected.

4.5. Assumptions and Drawbacks of method

Similar to the Cryoscope experiment discussed in Section **??**, this method also assumes that the qubit control system is a linear time-invariant system. With this assumption, the method faces the same disadvantage as the Cryoscope protocol - non-linear distortions are glossed over. In situations where non-linear distortions dominate, the above method would not be a perfect fit for noise characterization.
In attempting to identify the system impulse response $h(t)$ using the falling edge of the pulse, there is the problem of resonator noise. The effect of resonator noise is much more observable in the above method than in the Cryoscope. One explanation of this effect could be that in the absence of detuning, the qubit state measurements fluctuation is a lot more observable in the graphs.
A third drawback of the experiment is that, ideally, for the same input parameters such as the flux amplitude and duration, the $h(t)$ obtained from the Cryoscope experiment and Kelly's version of Ramsey must be the

same. That is, $h(t)_{cryoscope} = h(t)_{ramsey\_kelly}$. This is because the system impulse response must be the same for both experiments. However, using the simulation, when comparing the above relation, the individual system impulse responses do not match. A more detailed analysis of the working of Kelly's version of the Ramsey experiment is required to check its efficacy.

5

Chevron

The third method investigated for the characterization of distortions in the qubit control line is the Chevron method [46]. This method differs from the previously discussed methods by employing two-qubit interactions to identify the existence of noise in the qubit control line. The working of the Chevron experiment is based on the same principle of implementing the two-qubit CPHASE gate discussed in Section 2.5.

5.1. Principle

The Chevron experiment uses the principle of Avoided Crossing to check for the coupling between two qubits (or two systems that can resonate with each other). In the current implementation, the experiment is done with two transmon qubits, each with its individual qubit transition frequency. To explain with an example, in figure 5.1, assume that the f_{01} transition frequency for the first qubit q_a is at 5.5 GHz and the f_{01} transition frequency for the second qubit q_b is at 4.982 GHz. Then the higher frequency qubit q_a is detuned such that it's f_{01} transition frequency resonates with the transition frequency of a lower frequency qubit (q_b). This detuning is done by applying a square pulse of a particular amplitude. Under the condition that this square pulse is ideal, the detuned frequency will be as expected. But when distortions are present, the detuned frequency will differ from the required value and q_a will not be in resonance with q_b (which is the basis for two-qubit gates [47]).

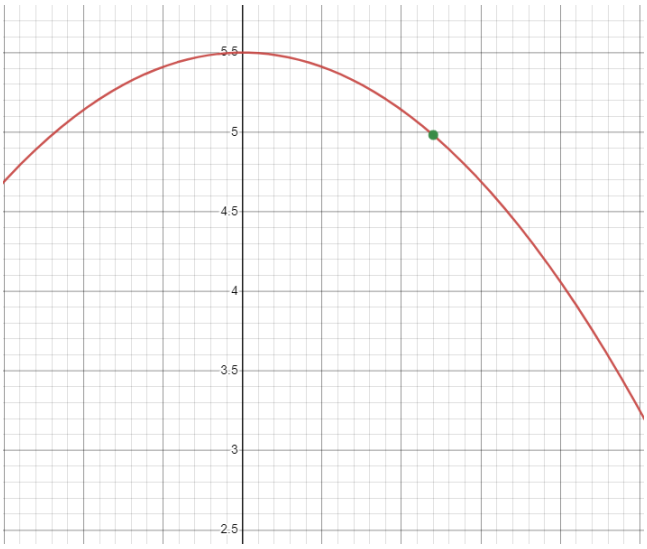

Figure 5.1: Flux Arc of a Cryoscope experiment

On detuning q_a to 4.982GHz, due to the phenomenon of **Avoided Crossing** wherein due to the interaction between the two qubits, there is an exchange in population density. This means, at perfect resonance, the

population densities (the probability of $|1\rangle$ state) of both qubits oscillate in perfectly out-of-phase sinusoids (of peak 1 to 0) with the summation of population densities always 1 (total probability of finding a qubit is 1). When there is no interaction between the qubits, the probabilities are entirely skewed (two horizontal lines). With these boundary conditions, when there is a slight energy interaction between the two qubits, the probability states oscillate with a higher frequency and low amplitudes (with the summation of amplitudes always being one).

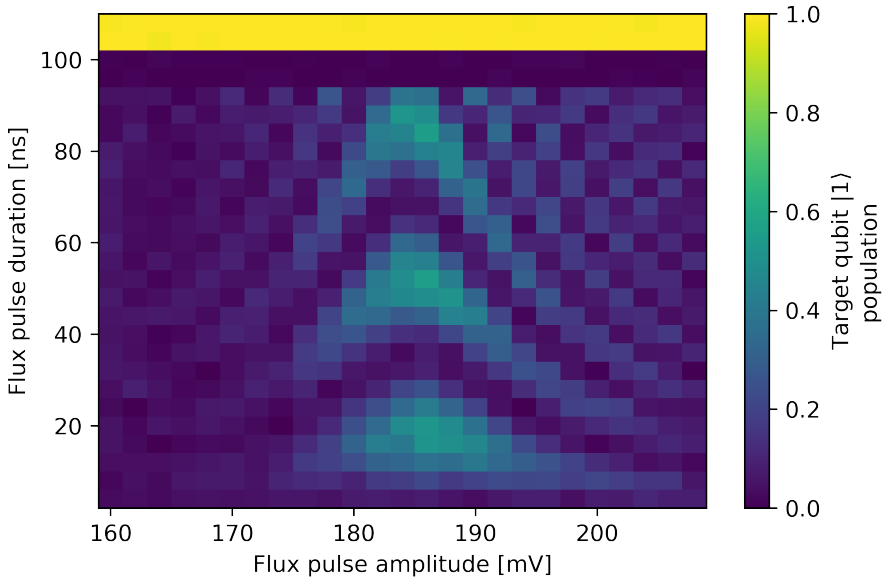

Figure 5.2: Chevron graph taken from reference [48]

With the on-resonance amplitude (around 186mV in figure 5.2) as the centre of symmetry, the off-resonance populations are plotted as the side lobes. When the detuning is not perfect, i.e., when there are distortions on the square pulse, the on-resonance amplitude becomes skewed.

5.1.1. Avoided Crossing

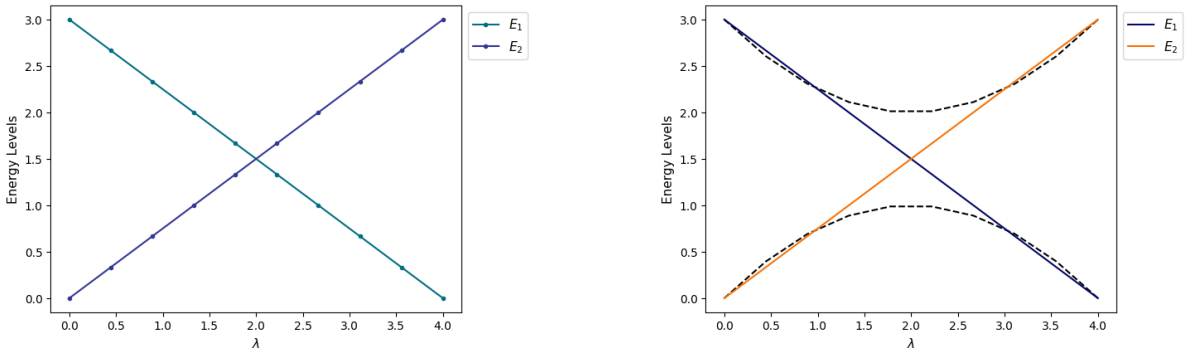

(a) Expected Energy levels

(b) Actual Energy levels

Figure 5.3: Avoided Crossing in quantum systems

For a quantum mechanical system, the system's energy can be defined using a Hamiltonian $\hat{H}$. If the system has discrete energy levels, then those energy levels (the eigenvalues of $\hat{H}$) affected by a varying parameter (say λ), when plotted, would be expected to look like Figure 5.3a. In this example of a quantum system with two energy levels placed close to each other, in actuality do not cross each other [49] and the energy levels instead are more similar to Figure 5.3b. Rather than intersecting, the two energy levels approach close and then diverge, showing that the low energy state prefers staying close to other low energy values, and the higher

energy state remains close to higher energy values. This phenomenon is termed the Avoided Crossing or Level repulsion.
At the crossing point, however, there is an interaction between the two energy states leading to a continuous exchange of energy. For example, consider a quantum mechanical system of two qubits q_a and q_b of varying energies. It is observed that on fluxing one Qubit, the energy of the net quantum state is affected [47]. When the singular Qubit q_a is detuned, the qubit transition frequency decreases, lowering its energy close enough to the lower frequency qubit q_b taking the system to a region of avoided Crossing.
In the scenario where their respective energies are far away from the region of Avoided Crossing, their state

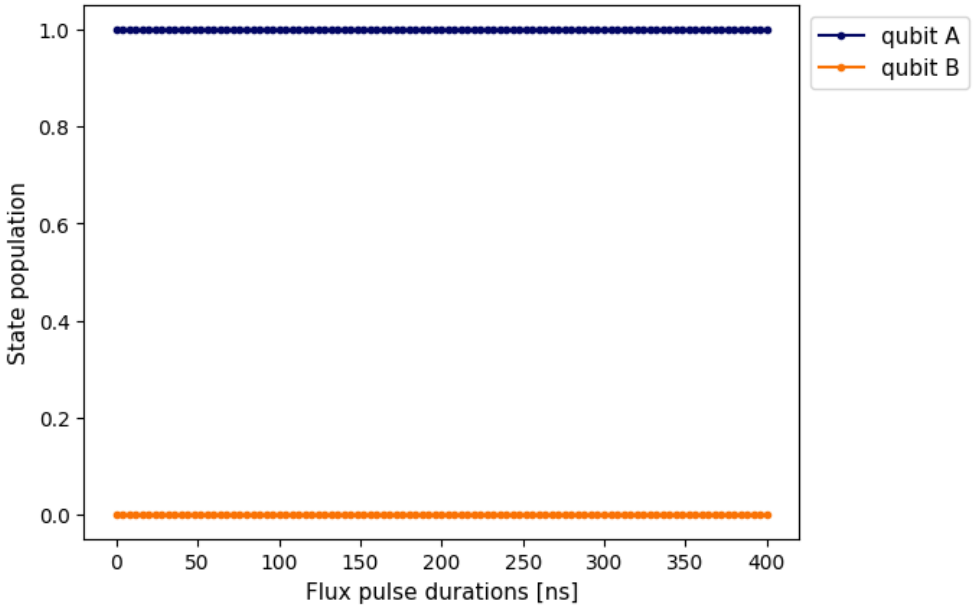

Figure 5.4: Qubit states far away from the avoided Crossing

populations would look like Figure 5.4.
As the Qubit q_a is detuned with higher flux amplitudes, the energy level inches closer to the avoided crossing

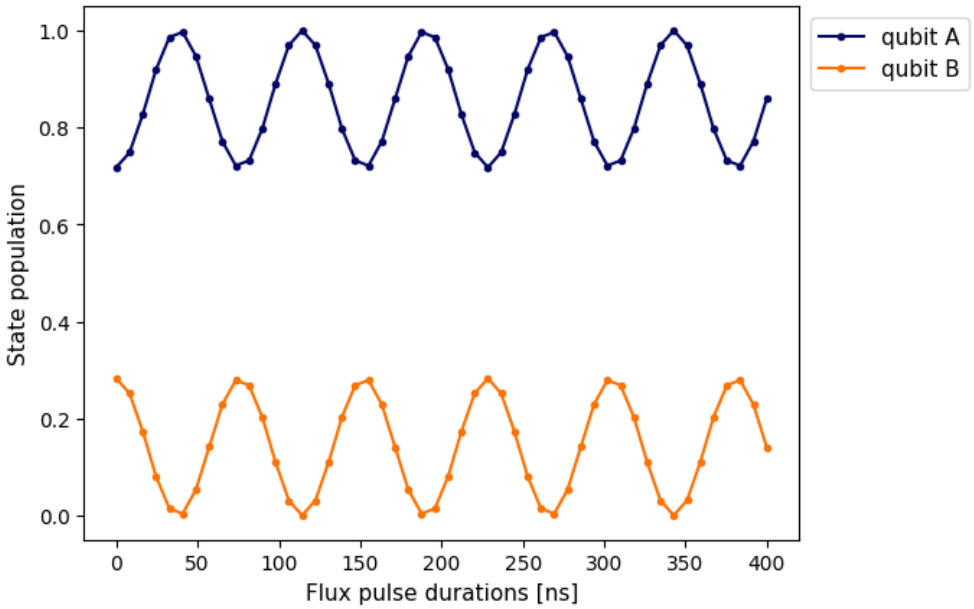

Figure 5.5: Qubit states close to the avoided Crossing

region. Interactions between the two qubits can be observed in state exchanges as shown in Figure 5.5.
As the Qubit q_a is further detuned, when its energy reaches the minimum energy it can have right at the

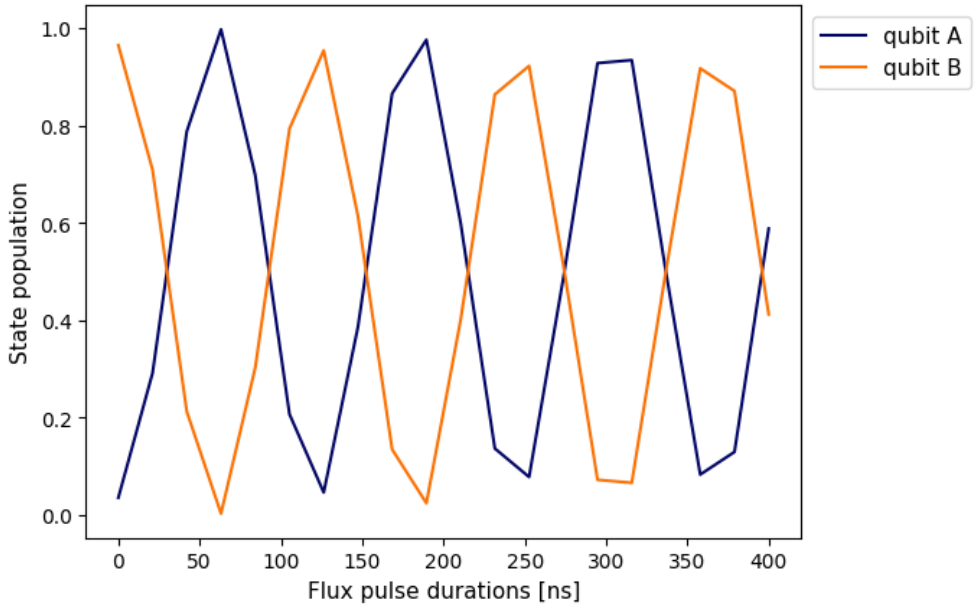

Figure 5.6: Qubit states at the avoided Crossing

region of avoided Crossing, there will be maximum state exchange between the two qubits as shown by Figure 5.6. Since this state interaction is caused by the application of flux (for qubit detuning), plotting a heat map shows the place of the occurrence of the maximum oscillations. Figure 5.2 shows the oscillations of the target qubit (q_b) against the flux amplitude, and it can be seen that the maximum oscillations occur at the midpoint (here around 0.186V), the region of avoided Crossing. These qubit-qubit interactions are a way to realize the two-qubit CPHASE gate [47].
In an ideal situation where the qubit control line is noiseless, the detuning of the higher frequency qubit occurs without any errors. This is seen as the perfect exchange of state population as shown in Figure 5.6. In the presence of distortions, the flux amplitude given as input is noisy, affecting the qubit detuning. Observing the Chevron plot in such conditions can identify the presence of distortions.

5.2. Implementation

The Chevron experiment is a two-qubit method that should give outputs of the respective heatmaps of the Qubit that is detuned using the flux pulse (the pulsed Qubit) and the other lower frequency qubit (the spectator qubit). The region of avoided Crossing where the state population exchange occurs is taken as either $|01\rangle - |10\rangle$ transition or $|11\rangle - |02\rangle$ transition. Initially, the two qubits are reset to the $|0\rangle$ state and then taken to either the $|11\rangle$ state or the $|01\rangle$ state through X rotations specified using the R_{xy} function.

$$R_{xy}(\theta,\varphi) = \begin{bmatrix} \cos(\theta/2) & -ie^{-i\varphi}\sin(\theta/2) \\ -ie^{i\varphi}\sin(\theta/2) & \cos(\theta/2) \end{bmatrix}$$

Therefore, by specifying $\theta = 180°$ and $\varphi = 0°$, the required X gates are implemented. After the initial X rotations to prepare the required states, the higher frequency qubit is detuned using a flux pulse with a specified pulse duration and a particular flux amplitude. A final rotation gate with similar values to the initial X rotations is implemented, and the qubit states are measured. This is the basis for the execution of a CPHASE gate, as discussed in Section 2.5. This block is repeated multiple times by varying the pulse duration, and the pulse amplitude and the output measurements of every run are used in plotting the final heat maps of both qubits.

5.3. Expected Results

In the absence of noise on the qubit control line, the peaks along the flux amplitude for maximum state interaction are aligned. However, when the flux pulse undergoes distortions, these peaks are unaligned and away from the region where the maximum state interaction can be expected. This serves as an indicator of the presence of distortions on the flux pulse. With the knowledge of whether the noise affects the square pulse, the next step would be to inverse the distorted version of the Chevron plot to correct the distortions. This direct inversion is challenging and computationally intensive as large datasets would need to be analysed. Therefore, instead of employing this method to correct for noise, the chevron experiment is better used as a quality check on how ideal the square pulse is at the pulsed qubit. Using another distortion-correction protocol, the Chevron experiment can now be run on the corrected qubit to check how well the distortion-correction protocol works. Figure 5.7 shows the results of the Chevron experiment conducted for state exchanges $|11\rangle - |02\rangle$

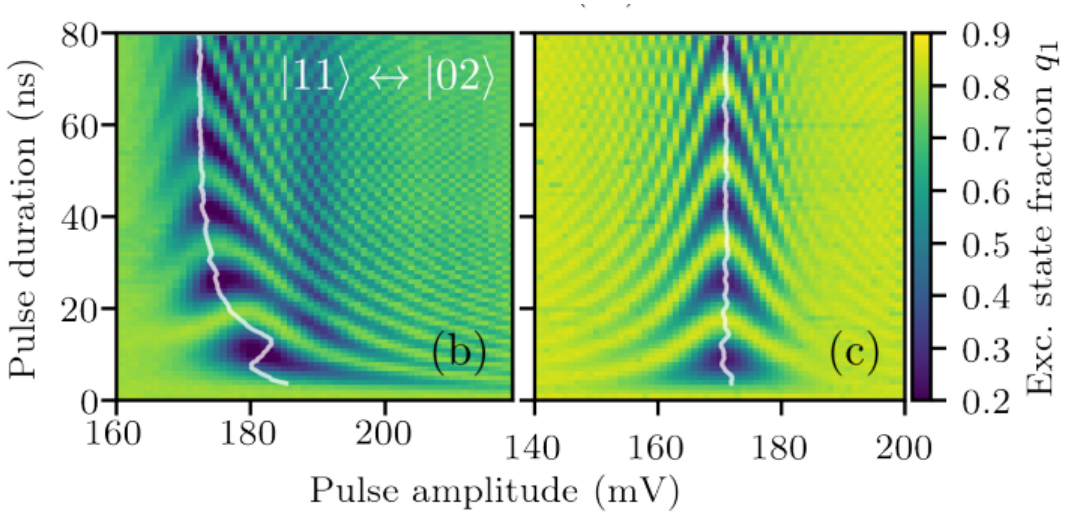

Figure 5.7: Chevron plots in (a) presence of distortions (b) absence of distortions taken from [28]

when the flux amplitude is affected by distortions and after the application of the Cryoscope distortion-correction protocol. It can be seen that after the implementation of the distortion-correction protocol, the Chevron plot peaks are aligned almost symmetrically, indicating that the protocol works as expected.

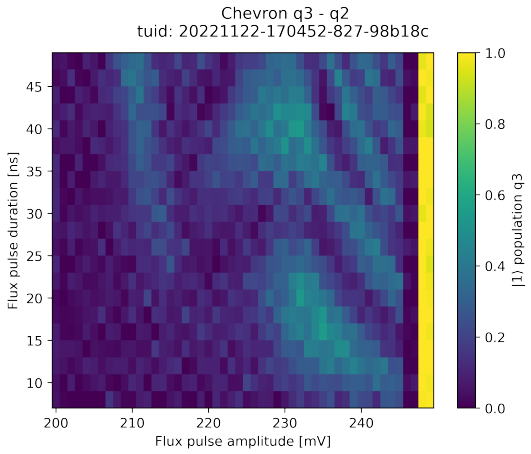

(a) Chevron heatmap before implementing the Cryoscope distortion-correction protocol

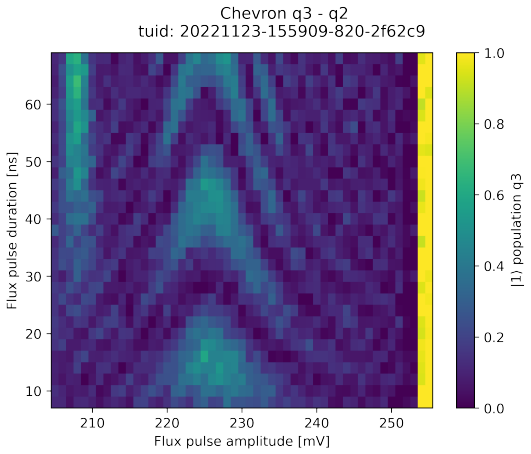

(b) Chevron heatmap after implementing the Cryoscope distortion-correction protocol

Figure 5.8: Chevron plots from recent experimental run [48]

With the above figure being taken from the reference work [28], Figure 5.8 shows the plots from a recent

experimental run for checking the efficacy of the Cryoscope experiment. Figure 5.8a shows the distribution of the state population of qubit q_3 in a two-qubit system comprised of qubits q_3 and q_2. In this figure, the distribution can be seen to be uneven without the expected shape of the peaks suggesting the presence of noise along the qubit control line. Rerunning the Chevron after the application of the Cryoscope gives Figure 5.8b, showing symmetrically aligned peaks indicating a reduction in the noise affecting the control line.

5.4. Assumptions and Drawbacks of method

The major drawback of this method is that extracting the exact distortion parameters by trying to invert the graph is computationally infeasible. Therefore, it is more useful as a check to discern if another applied distortion-correction protocol works or not. Rather than using it as a standalone method for noise correction, the Chevron method is a more straightforward noise identification method as employed in Chapter 6 of [28].

6

Comparison of Protocols

With three protocols studied and implemented, to get a better understanding of how they fare against each other, a comparison of the protocols was made. From the study of the three methods alone, the differences observed are outlined below.

- The first two methods - the Cryoscope and Ramsey using Kelly's method - are single qubit distortions characterization methods. They required only a single qubit for their functioning. Instead, the Chevron method needed two qubits for identifying the presence of distortions on the flux pulse.
- Only the Cryoscope method suggested a technique for reconstructing the flux pulse. Cryoscope was also shown to possess the capability to reconstruct arbitrary waveforms [41].
- As mentioned earlier, Chevron was shown only to check for the presence of distortions, unlike the other two methods, which were also shown to correct the distortions.

These essential dissimilarities observed do not deliver a detailed portrayal of the advantages and disadvantages of the methods when compared against each other. A user aiming to calibrate their transmon quantum computing setup might wish to know which distortions characterization method would be the most suitable as per their requirements. For example, if the user wishes to implement a distortions characterization protocol within a specified duration, then a functionality that performs a comparison of the available protocols and returns the most suitable protocols would be of massive help here. With this as the motivation, a code that runs the available protocols and calculates a given set of performance metrics was implemented. For now, the code merely takes in the first two methods because of time constraints in the project execution.

6.1. Implementation

As the first step, the metrics to be used to compare the protocols were decided upon. The parameters chosen were experiment runtime, memory used, deviation from the ideal values and quality of correction. Experiment runtime is the metric that accounts for the time taken to execute the experiment. This was measured by starting a timer before the protocol started and then stopping the timer after the results for that particular protocol were calculated.
Computer memory used by every protocol implementation was calculated using specialized functions in python (psutil and os libraries). The next performance metric computed was the 'deviation from ideal'. This metric computes the final difference between the reconstructed and ideal flux pulses. The motivation behind determining this metric is to give a view of how accurately each protocol does the correction. The smaller the deviation value, the more precise the correction.
The last metric considered is the 'quality of correction'. This metric checks if the correction parameters perfectly compensate for the distortions. That is, $1-(h^{-1}_{correction}(t) \circledast h(t)) = 0$ where $h^{-1}_{correction}(t)$ is the function described using the correction parameters and $h(t)$ is the impulse response of the system. This metric was determined to quantify how well a particular protocol corrects for every iteration. As this value inches closer to 0, the correction of the distorted flux pulse becomes better.

x0	runtime[s]	memory_usage[Bytes]	iterations	deviation_from_ideal	quality_of_correction_iteration_0	quality_of_correction_iteration_1
Cryoscope	22.584641	595537920	2	0.0043+/-0.0007	0.16782	0.156185
RamseyKelly	17.387666	421933056	2	0.0192+/-0.0011	0.10600	0.106000

Figure 6.1: Performance metrics of two distortion characterization protocols

6.2. Results

The code programmed, as explained above, was run for its efficacy by setting certain input variables. This code was executed with the protocols on the simulation environment and not on the quantum computing backend.

Table 6.1 shows the performance metrics calculated for the Cryoscope and Ramsey using Kelly's method. In this illustrative table, the number of iterations was set as two. It can be seen from this table that Cryoscope gives better reconstructions, with the quality of correction increasing as the number of iterations increase. In contrast, the second protocol initially corrects well and does not seem to improve the corrections as the number of iterations increases. Another factor that can be noticed is that the runtime and memory usage for the Cryoscope is higher when compared with the other method.

A point to be noted here, this implementation is just employed to illustrate the potential of the comparison. However, it can be said that this program can be further refined to generate detailed comparison results.

This comparison code was executed on the protocols using only the simulated data. With the performance metrics solely chosen based on Computer Engineering concepts, they were not checked for relevance by running this code on a quantum computing backend. For example, in present-day computing systems, memory consumption plays a vital role in computing performance [50]. But calculating the memory required to run a distortions characterization protocol might not play a significant role in helping the user choose a protocol for implementation. This might be so since every experiment on the qubit generates colossal amounts of data. Therefore, the calculation of memory required might be irrelevant when comparing the different protocols. However, evaluating the memory utilized by each distortions characterization protocol seemed to be a good starting point and hence, was implemented.

7

Conclusion

The thesis presents three methods that were effectively implemented to identify distortions in the transmon setup's flux control line. Out of these three, two protocols - the Cryoscope and Ramsey using Kelly's method, were shown to identify and correct for the distortions.

7.1. Summary of Chapter 3

The Cryoscope customized the Ramsey experiment originally used for calculating the transverse relaxation rates of the qubit. By introducing flux pulses after rotating the qubit to the equatorial plane, the qubit is intentionally detuned from the drive field. In doing so, it was shown that by extracting the detuning frequency, the input distorted flux pulse could be reconstructed. On reconstructing the pulse, the parameters to correct the pulse were calculated by using least squares optimization on a cost function (the cost function being the difference between the ideal pulse and the filtered version of the reconstructed pulse with distortions).

7.2. Summary of Chapter 4

Ramsey using Kelly's method was the second distortions-identifying method implemented. Similar to the Cryoscope, the major difference was instead of applying the flux pulse in between the $\pi/2$ rotations of the Ramsey, the flux pulse was applied to the qubit before executing the $\pi/2$ rotations. The purpose was to correct the distortion parameters using the falling edge of the pulse, whilst the Cryoscope attempts to do the same using the rising edge of the pulse. Again, the flow of analysis followed the same steps as the Cryoscope. The qubit detuning caused by distortions on the tail end of the flux pulse is extracted from the expectation values and then used to reconstruct the distorted fall edge of the pulse. The reconstruction is then used to calculate the correction parameters using the same method employed in the Cryoscope protocol.

While the Cryoscope implementation followed the same flow as wrought in the reference, the analysis of the above method was devised purely for this project based on guidance from the supervisor. This method still contains kinks that need to be straightened out before it can be effectively employed on the same scale as the Cryoscope. However, the implementation process helped in the understanding of the major steps involved in the execution of a novel idea.

7.3. Summary of Chapters 5 and 6

Chevron was the third method studied for identifying distortions. This protocol employed two qubits to verify a distortion-less pulse as opposed to the other two protocols, which used a single qubit. In a two-qubit system, a flux pulse is applied to one qubit to detune it to the frequency of the other qubit. In doing so, the system is taken to the region of avoided crossing, where a state exchange between the qubits can be observed. The next step is to plot a heatmap with flux amplitude, duration of flux and the state population of the qubits for the experiment. The presence of distortions can be gleaned from this plot by verifying the alignment of

maximum state interaction peaks. In the presence of distortions, the peak point of maximum state interaction will be misaligned. This misalignment shows that distortions exist in the pulse. The distorted pulse causes variations in detuning, which in turn causes the region of avoided crossing to occur at different amplitudes.
The Chevron method was studied, and the graphs were taken from previous experiments on the hardware. A significant challenge in using the Chevron to correct the distortions is that, while it can be easily used to detect distortions, using this experiment to go in reverse to correct the distorted flux is difficult. Therefore, in the scope of this thesis project, this experiment was only studied for using it to verify the presence of distortions.
The Comparison of protocols chapter elaborates on the procedure used for comparing the distortion-characterization methods. The performance metrics chosen were explained, and an example run of the program comparing the Cryoscope and Ramsey using Kelly's method was given. This example also gave conclusions based on the runtime and other performance metrics.

7.4. Future work

The thesis report explained the study and implementation of three methods to identify and correct distortions in flux pulses used in transmon systems. With many avenues for improvement and innovation, the potential future implementations that can follow this thesis project are summarized below.

- Out of the three methods, only the Cryoscope and Chevron have been verified for their functioning on an experimental setup. One potential future implementation can be the experimental run of the Ramsey using Kelly's method. For now, this implementation has only been verified for its working using simulation data. Experimentally executing this protocol might lead to more insights into this method.
- The scope of this thesis project was limited to three distortions identifying protocols. A possible next step would be implementing other available distortions correcting protocols, such as the cryo-VNA method [51].
- In the Chevron experiment, the current implementation is employed only to verify if distortions are present. A possible next step might be to prepare a method to extract the distorting parameters and use them to concoct a correction protocol.
- Another area for future innovation lies in the area of comparison of protocols. In the current implementation, the comparison was made only for a few parameters, namely the runtime, memory usage, the number of iterations and the final deviation of the reconstruction from the ideal pulse. The next step might be to consider more performance metrics to gauge the efficacy of the methods against each other. Theoretically, by executing a distortion-characterizing method, the distortions on the control line are perfectly corrected. However, in practical conditions, this might not be true, and a qubit system may necessitate multiple runs of the same protocols to tamp down the distortions to a permissible level. Therefore, an example performance metric could be the number of times a particular protocol needs to be repeated until the distortions reach a tolerable limit.
- For now, the comparison was made using only simulations for just the Cryoscope and Ramsey using Kelly's method. A possible next step could be to extend the comparison of the protocols to include Chevron. An exciting implementation would be running the comparison when the protocols are being executed on the quantum computing backend. This might show exciting results in total experiment runtime, the number of iterations it takes for the reconstruction to reach tolerable levels etc.
- The methods discussed above are restricted to correcting linearly affecting errors by assuming that the qubit control system is a Linear Time Invariant system. To extend beyond this linear regime, other noise characterizations, such as the Quantum Noise Spectroscopy protocols, can be employed [52].

To perform exciting operations such as quantum gates, the qubit system must be well-calibrated. Flux characterization, therefore, is also an important section of qubit characterization. With this work, linear distortions in the flux control line of transmon were studied, and three methods to identify and correct them were implemented.

A

Mathematical Methods

A.1. Least Squares Optimization method:

The Least Squares regression method is used to optimize parameters based on the error function. Assume measured parameters y_n that are a function of known variables x_n $\forall$ n $\in [1, N]$. Therefore, it can be written that

$$y_n = f(x_n)$$

In the presence of some error variables, denoted by ϵ, the measured parameter is affected and the relation becomes

$$y_n^{'} = f(x_n) + \epsilon$$

The principle behind this method is to find the minimum values of 'p', such that $\sum_{n=1}^{N}(p * y_n^{'})^2 - (y_n)^2$ is minimum [53].
In the software, the optimization is implemented by deciding upon an FIR filter function that is set with some initial filter coefficients (a,b). Therefore the residue to be minimized is now defined as

$$residue = \sum_{n=1}^{N}(f_{a,b}^{FIR} * y_n^{measured})^2 - (y_n^{ideal})^2 \tag{A.1}$$

This equation A.1 is swept over a range of varying (a,b) values until the residue is minimum. The particular (a,b) values for the minimum residue is returned as output.

Listing A.1: Code snippet showing cost function using Lfilter

```
    # Define a cost function which returns the residuals between the target
    # and the filtered signal
    def cost_function(fir_coefficients, pulse, target_pulse):
        filtered_signal = lfilter(b=fir_coefficients, a=1, x=pulse)
        return target_pulse - filtered_signal

    ideal_b = np.zeros(len(pulse))
    ideal_b[0] = 1

    # Minimise the cost function
    minimisation_result = least_squares(
        cost_function, x0=ideal_b, args=(pulse, target_pulse)
    )

    # Return the result array
    return minimisation_result.x
```

In the code snippet A.1, function *cost_function* computes the residue on calling it. By using the $least\_squares$ method available in the Python - SciPy module, the required filter coefficients for which the *pulse* (distorted measurements) is corrected to resemble the *target_pulse* (ideal square pulse) are returned as *minimization_result.x*.

Bibliography

[1] G. E. Moore, "Cramming more components onto integrated circuits," *IEEE Solid-State Circuits Society Newsletter*, vol. 11, no. 3, pp. 33–35, 2006.

[2] D. Geer, "Chip makers turn to multicore processors," *Computer*, vol. 38, no. 5, pp. 11–13, 2005.

[3] D. H. Woo and H.-H. S. Lee, "Extending amdahl's law for energy-efficient computing in the many-core era," *Computer*, vol. 41, no. 12, pp. 24–31, 2008.

[4] T. Becker, O. Mencer, and G. Gaydadjiev, *Spatial Programming with OpenSPL*. Springer Science+Business Media, 2016, pp. 83–98.

[5] M. A. Nielsen and I. L. Chuang, "Quantum Computation and Quantum Information," 2000.

[6] P. Krantz, M. Kjaergaard, F. Yan, T. P. Orlando, S. Gustavsson, and W. D. Oliver, "A Quantum Engineer's Guide to Superconducting Qubits," *Applied Physics Reviews*, vol. 6, no. 2, p. 021318, Jun. 2019, arXiv: 1904.06560. [Online]. Available: http://arxiv.org/abs/1904.06560

[7] R. Hanson, O. Gywat, and D. D. Awschalom, "Room-temperature manipulation and decoherence of a single spin in diamond," *Phys. Rev. B*, vol. 74, p. 161203, Oct 2006. [Online]. Available: https://link.aps.org/doi/10.1103/PhysRevB.74.161203

[8] M. V. G. Dutt, L. Childress, L. Jiang, E. Togan, J. Maze, F. Jelezko, A. S. Zibrov, P. R. Hemmer, and M. D. Lukin, "Quantum register based on individual electronic and nuclear spin qubits in diamond," *Science*, vol. 316, no. 5829, pp. 1312–1316, 2007. [Online]. Available: https://www.science.org/doi/abs/10.1126/science.1139831

[9] B. E. Kane, "A silicon-based nuclear spin quantum computer," *Nature*, vol. 393, no. 6681, pp. 133–137, may 1998.

[10] D. Loss and D. P. DiVincenzo, "Quantum computation with quantum dots," *Phys. Rev. A*, vol. 57, pp. 120–126, Jan 1998. [Online]. Available: https://link.aps.org/doi/10.1103/PhysRevA.57.120

[11] D. Leibfried, R. Blatt, C. Monroe, and D. Wineland, "Quantum dynamics of single trapped ions," *Rev. Mod. Phys.*, vol. 75, pp. 281–324, Mar 2003. [Online]. Available: https://link.aps.org/doi/10.1103/RevModPhys.75.281

[12] R. Blatt and D. Wineland, "Entangled states of trapped atomic ions," *Nature*, vol. 453, no. 7198, pp. 1008–1015, jun 2008.

[13] D. Jaksch and P. Zoller, "The cold atom hubbard toolbox," *Annals of Physics*, vol. 315, no. 1, pp. 52–79, 2005, special Issue. [Online]. Available: https://www.sciencedirect.com/science/article/pii/S0003491604001782

[14] E. Knill, R. Laflamme, and G. J. Milburn, "A scheme for efficient quantum computation with linear optics," *Nature*, vol. 409, no. 6816, pp. 46–52, jan 2001.

[15] J. van Dijk, E. Charbon, and F. Sebastiano, "The electronic interface for quantum processors," *Microprocessors and Microsystems*, vol. 66, pp. 90–101, 2019. [Online]. Available: https://www.sciencedirect.com/science/article/pii/S0141933118303417

[16] M. Kjaergaard, M. E. Schwartz, J. Braumüller, P. Krantz, J. I.-J. Wang, S. Gustavsson, and W. D. Oliver, "Superconducting qubits: Current state of play," *Annual Review of Condensed Matter Physics*, vol. 11, no. 1, pp. 369–395, 2020. [Online]. Available: https://doi.org/10.1146/annurev-conmatphys-031119-050605

[17] MIT, "Lecture notes, Basic Josephson Junctions," https://web.mit.edu/6.763/www/FT03/Lectures/Lecture11.pdf.

[18] T. Roth, R. Ma, and W. C. Chew, "An introduction to the transmon qubit for electromagnetic engineers," 06 2021.

[19] U. Vool and M. Devoret, "Introduction to quantum electromagnetic circuits," *International Journal of Circuit Theory and Applications*, vol. 45, no. 7, pp. 897–934, jun 2017. [Online]. Available: https://doi.org/10.1002%2Fcta.2359

[20] S. M. Girvin, "Page 40, Lecture Notes, Circuit QED: Superconducting Qubits Coupled to Microwave Photons," 2016, http://www.capri-school.eu/lectureres/master_cqed_les_houches.pdf.

[21] A. Cottet, "Implementation of a quantum bit in a superconducting circuit," PhD Dissertation, Université Paris VI, 2002. [Online]. Available: http://www.phys.ens.fr/~cottet/ACottetThesis.pdf

[22] X. Gu, A. F. Kockum, A. Miranowicz, Y. xi Liu, and F. Nori, "Microwave photonics with superconducting quantum circuits," *Physics Reports*, vol. 718-719, pp. 1–102, 2017, microwave photonics with superconducting quantum circuits. [Online]. Available: https://www.sciencedirect.com/science/article/pii/S0370157317303290

[23] W. C. Chew, D.-Y. Na, P. Bermel, T. E. Roth, C. J. Ryu, and E. Kudeki, "Quantum maxwell's equations made simple: Employing scalar and vector potential formulation," *IEEE Antennas and Propagation Magazine*, vol. 63, no. 1, pp. 14–26, 2021.

[24] V. Bouchiat, D. Vion, P. Joyez, D. Esteve, and M. H. Devoret, "Quantum coherence with a single cooper pair," *Physica Scripta*, vol. 1998, no. T76, p. 165, jan 1998. [Online]. Available: https://dx.doi.org/10.1238/Physica.Topical.076a00165

[25] A. F. Kockum and F. Nori, "Quantum bits with josephson junctions," in *Fundamentals and Frontiers of the Josephson Effect*. Springer International Publishing, 2019, pp. 703–741. [Online]. Available: https://doi.org/10.1007%2F978-3-030-20726-7_17

[26] J. Koch, T. M. Yu, J. Gambetta, A. A. Houck, D. I. Schuster, J. Majer, A. Blais, M. H. Devoret, S. M. Girvin, and R. J. Schoelkopf, "Charge-insensitive qubit design derived from the cooper pair box," *Phys. Rev. A*, vol. 76, p. 042319, Oct 2007. [Online]. Available: https://link.aps.org/doi/10.1103/PhysRevA.76.042319

[27] X. Y. Jin, A. Kamal, A. P. Sears, T. Gudmundsen, D. Hover, J. Miloshi, R. Slattery, F. Yan, J. Yoder, T. P. Orlando, S. Gustavsson, and W. D. Oliver, "Thermal and residual excited-state population in a 3d transmon qubit," *Phys. Rev. Lett.*, vol. 114, p. 240501, Jun 2015. [Online]. Available: https://link.aps.org/doi/10.1103/PhysRevLett.114.240501

[28] M. A. Rol, "Control for programmable superconducting quantum systems," PhD Dissertation, Delft University of Technology, 2020. [Online]. Available: https://doi.org/10.4233/uuid:0a2ba212-f6bf-4c64-8f3d-b707f1e44953

[29] X. Fu, L. Riesebos, L. Lao, C. G. Almudever, F. Sebastiano, R. Versluis, E. Charbon, and K. Bertels, "A heterogeneous quantum computer architecture," in *Proceedings of the ACM International Conference on Computing Frontiers*, ser. CF '16. New York, NY, USA: Association for Computing Machinery, 2016, p. 323–330. [Online]. Available: https://doi.org/10.1145/2903150.2906827

[30] R. LaRose, "Expectation values," https://www.ryanlarose.com/uploads/1/1/5/8/115879647/quic04s02s.pdf.

[31] F. Bloch, "Generalized theory of relaxation," *Phys. Rev.*, vol. 105, pp. 1206–1222, Feb 1957. [Online]. Available: https://link.aps.org/doi/10.1103/PhysRev.105.1206

[32] J. Bylander, S. Gustavsson, F. Yan, F. Yoshihara, K. Harrabi, G. Fitch, D. Cory, Y. Nakamura, J. Tsai, and W. Oliver, "Noise spectroscopy through dynamical decoupling with a superconducting flux qubit," *Nature Physics*, vol. 7, no. 7, pp. 565–570, jul 2011. [Online]. Available: https://doi.org/10.1038/nphys1994

[33] R. H. Koch, D. P. DiVincenzo, and J. Clarke, "Model for $1/f$ flux noise in squids and qubits," *Phys. Rev. Lett.*, vol. 98, p. 267003, Jun 2007. [Online]. Available: https://link.aps.org/doi/10.1103/PhysRevLett.98.267003

[34] A. O. Niskanen, K. Harrabi, F. Yoshihara, Y. Nakamura, S. Lloyd, and J. S. Tsai, "Quantum coherent tunable coupling of superconducting qubits," *Science*, vol. 316, no. 5825, pp. 723–726, 2007. [Online]. Available: https://www.science.org/doi/abs/10.1126/science.1141324

[35] R. C. Bialczak, M. Ansmann, M. Hofheinz, E. Lucero, M. Neeley, A. D. O'Connell, D. Sank, H. Wang, J. Wenner, M. Steffen, A. N. Cleland, and J. M. Martinis, "Quantum process tomography of a universal entangling gate implemented with josephson phase qubits," *Nature Physics*, vol. 6, pp. 409–413, jun 2010. [Online]. Available: https://doi.org/10.1038/nphys1639

[36] D. Sank, R. Barends, R. C. Bialczak, Y. Chen, J. Kelly, M. Lenander, E. Lucero, M. Mariantoni, A. Megrant, M. Neeley, P. J. J. O'Malley, A. Vainsencher, H. Wang, J. Wenner, T. C. White, T. Yamamoto, Y. Yin, A. N. Cleland, and J. M. Martinis, "Flux noise probed with real time qubit tomography in a josephson phase qubit," *Phys. Rev. Lett.*, vol. 109, p. 067001, Aug 2012. [Online]. Available: https://link.aps.org/doi/10.1103/PhysRevLett.109.067001

[37] M. Reagor, C. B. Osborn, N. Tezak, A. Staley, G. Prawiroatmodjo, M. Scheer, N. Alidoust, E. A. Sete, N. Didier, M. P. da Silva, E. Acala, J. Angeles, A. Bestwick, M. Block, B. Bloom, A. Bradley, C. Bui, S. Caldwell, L. Capelluto, R. Chilcott, J. Cordova, G. Crossman, M. Curtis, S. Deshpande, T. E. Bouayadi, D. Girshovich, S. Hong, A. Hudson, P. Karalekas, K. Kuang, M. Lenihan, R. Manenti, T. Manning, J. Marshall, Y. Mohan, W. O'Brien, J. Otterbach, A. Papageorge, J.-P. Paquette, M. Pelstring, A. Polloreno, V. Rawat, C. A. Ryan, R. Renzas, N. Rubin, D. Russel, M. Rust, D. Scarabelli, M. Selvanayagam, R. Sinclair, R. Smith, M. Suska, T.-W. To, M. Vahidpour, N. Vodrahalli, T. Whyland, K. Yadav, W. Zeng, and C. T. Rigetti, "Demonstration of universal parametric entangling gates on a multi-qubit lattice," *Science Advances*, vol. 4, no. 2, p. eaao3603, 2018. [Online]. Available: https://www.science.org/doi/abs/10.1126/sciadv.aao3603

[38] Y. Chen, C. Neill, P. Roushan, N. Leung, M. Fang, R. Barends, J. Kelly, B. Campbell, Z. Chen, B. Chiaro, A. Dunsworth, E. Jeffrey, A. Megrant, J. Mutus, P. O'Malley, C. Quintana, D. Sank, A. Vainsencher, J. Wenner, T. White, M. R. Geller, A. Cleland, and J. M. Martinis, "Qubit architecture with high coherence and fast tunable coupling," *Physical Review Letters*, vol. 113, no. 22, nov 2014. [Online]. Available: https://doi.org/10.1103%2Fphysrevlett.113.220502

[39] N. Didier, E. A. Sete, M. P. da Silva, and C. Rigetti, "Analytical modeling of parametrically modulated transmon qubits," *Physical Review A*, vol. 97, no. 2, feb 2018. [Online]. Available: https://doi.org/10.1103%2Fphysreva.97.022330

[40] L. DiCarlo, J. M. Chow, J. M. Gambetta, L. S. Bishop, B. R. Johnson, D. I. Schuster, J. Majer, A. Blais, L. Frunzio, S. M. Girvin, and R. J. Schoelkopf, "Demonstration of two-qubit algorithms with a superconducting quantum processor," *Nature*, vol. 460, jul 2009. [Online]. Available: https://doi.org/10.1038/nature08121

[41] M. A. Rol, L. Ciorciaro, F. K. Malinowski, B. M. Tarasinski, R. E. Sagastizabal, C. C. Bultink, Y. Salathe, N. Haandbaek, J. Sedivy, and L. DiCarlo, "Time-domain characterization and correction of on-chip distortion of control pulses in a quantum processor," *Applied Physics Letters*, vol. 116, no. 5, p. 054001, 2020. [Online]. Available: https://doi.org/10.1063/1.5133894

[42] Orange Quantum Systems and Qblox, "Quantify-scheduler," https://quantify-quantify-scheduler.readthedocs-hosted.com/en/v0.11.1/.

[43] A. Oppenheim, A. Willsky, and S. Nawab, *Signals & Systems*, ser. Prentice-Hall signal processing series. Prentice Hall, 1997. [Online]. Available: https://books.google.nl/books?id=LwQqAQAAMAAJ

[44] J. S.Kelly, "Fault-tolerant superconducting qubits," PhD Dissertation, University of California Santa Barbara, 2015. [Online]. Available: https://web.physics.ucsb.edu/~martinisgroup/theses/Kelly2015.pdf

[45] S. W. Smith, “Chapter 7, the scientist and engineer’s guide to digital signal processing,” 1999. [Online]. Available: https://www.analog.com/media/en/technical-documentation/dsp-book/dsp_book_Ch7.pdf

[46] N. K. Langford, R. Sagastizabal, M. Kounalakis, C. Dickel, A. Bruno, F. Luthi, D. J. Thoen, A. Endo, and L. DiCarlo, “Experimentally simulating the dynamics of quantum light and matter at deep-strong coupling,” *Nature Communications*, vol. 8, no. 1, nov 2017. [Online]. Available: https://doi.org/10.1038%2Fs41467-017-01061-x

[47] L. DiCarlo, J. M. Chow, J. M. Gambetta, L. S. Bishop, B. R. Johnson, D. I. Schuster, J. Majer, A. Blais, L. Frunzio, S. M. Girvin, and R. J. Schoelkopf, “Demonstration of two-qubit algorithms with a superconducting quantum processor,” *Nature*, vol. 460, no. 7252, pp. 240–244, jun 2009. [Online]. Available: https://doi.org/10.1038%2Fnature08121

[48] O. Q. Systems, “Tutorials of qubit characterization methods, **part of** the **Quantum Diagnostics Libraries** provided by **Orange Quantum Systems**.” [Online]. Available: https://orangeqs.com/

[49] M. Wilkinson, “Narrowly avoided crossings,” *Journal of Physics A: Mathematical and General*, vol. 20, no. 3, p. 635, feb 1987. [Online]. Available: https://dx.doi.org/10.1088/0305-4470/20/3/026

[50] O. Mutlu, “Memory scaling: A systems architecture perspective,” pp. 21–25, 2013.

[51] M. Jerger, A. Kulikov, Z. Vasselin, and A. Fedorov, “In situ characterization of qubit control lines: A qubit as a vector network analyzer,” *Phys. Rev. Lett.*, vol. 123, p. 150501, Oct 2019. [Online]. Available: https://link.aps.org/doi/10.1103/PhysRevLett.123.150501

[52] Y. Sung, F. Beaudoin, L. M. Norris, F. Yan, D. K. Kim, J. Y. Qiu, U. von Lüpke, J. L. Yoder, T. P. Orlando, S. Gustavsson, L. Viola, and W. D. Oliver, “Non-gaussian noise spectroscopy with a superconducting qubit sensor,” *Nature Communications*, vol. 10, sep 2019. [Online]. Available: https://doi.org/10.1038/s41467-019-11699-4

[53] E. P. Simoncelli, “Least squares optimization,” http://www.cns.nyu.edu/~eero/math-tools/Handouts/leastSquares.pdf.